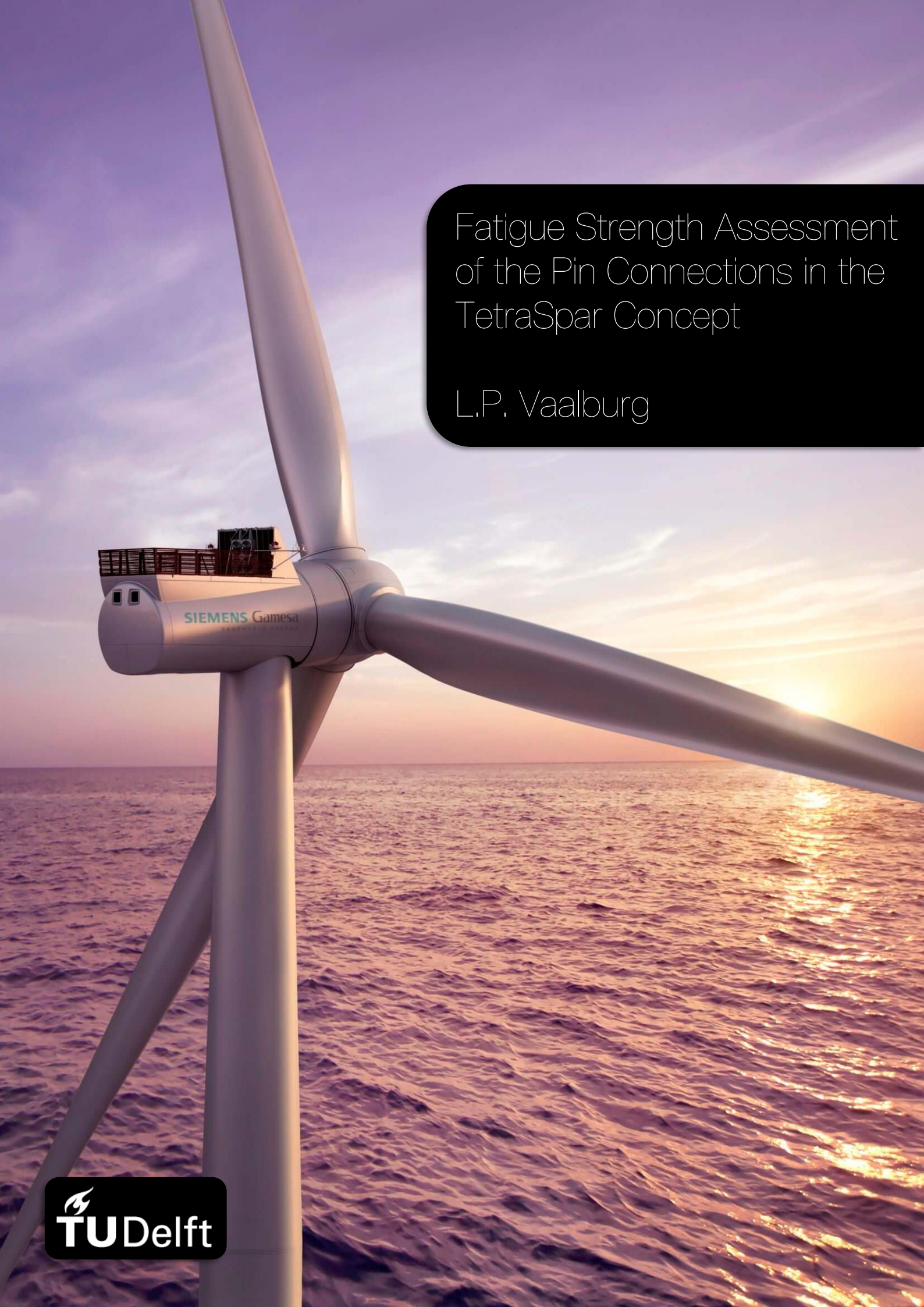

Fatigue Strength Assessment of the Pin Connections in the TetraSpar Concept

L.P. Vaalburg

TU Delft

Fatigue Strength Assessment of the Pin Connections in the TetraSpar Concept

by

L.P. Vaalburg

to obtain the degree of Master of Science
at the Delft University of Technology,
to be defended publicly on Friday November 8, 2019 at 14:00.

Student number:	4211359	
Project duration:	February 1, 2019 – November 8, 2019	
Thesis committee:	Ir. A.C.M. van der Stap,	TU Delft, chairman
	Ir. C. Keijdener,	TU Delft, supervisor
	Ir. P.A. de Vries,	TU Delft
	Ir. J.W. van de Graaf,	Shell

This thesis is confidential and cannot be made public until November 8, 2024.

An electronic version of this thesis is available at `http://repository.tudelft.nl/`.

TU Delft

Acknowledgements

Many people have contributed the present thesis in different ways. I was honestly surprised how many people were willing to share their knowledge, provide feedback or give advice! I would like to thank some people in particular:

Jan Willem van de Graaf for the supervision of my project. Thank you that you could always make time for Skype calls, for meeting in real-life at Shell in Rijswijk or for answering my questions by e-mail. I have learned a lot from your persistence to solve the challenges that we encountered and to really understand them. Your years of experience as an engineer have really helped me to make this research project a success.

André van der Stap for the introduction to this project. It was great to contribute to a real-life project with a very clear challenge. The fact that the results of this research can actually be used for the TetraSpar project is awesome, and something that many students would admire. I would also like to thank you for the opportunities that you have offered me within Shell. It was a very valuable experience to visit the fabrication site at Welcon in Denmark. Also, you have included me in many activities, and you introduced me to many people within Shell. This has led to valuable connections and experiences, which is greatly appreciated.

Chris Keijdener and **Peter de Vries**, supervisors of my project from university. Thank you for the time and effort that you have put in the progress meetings and supervision of my project. After every meeting you have given useful advice and valuable feedback on my work, which has really helped me to finish the project in time.

Morten Walkusch, engineer from Welcon/Stiesdal in the TetraSpar project team. I would like to thank you for the hospitality at Welcon in Denmark. Everyone at Welcon has given me a very warm welcome, but you in particular. Thank you also for making time to help me with my project. Mainly because of your help, I was able to quickly understand the FE software and to build a good model in the few days I was in Denmark. Also, the time that you made to answer questions or send new models via e-mail was greatly appreciated.

Steven Zijp, project leader of the Shell TetraSpar team. From the beginning, you have considered me as a member of the project team. You invited me for meetings, sent me useful information and documents and we had nice and useful chats over a cup of coffee. So, thank you for making me a real part of the project team and for your support during the project!

Marcel van Veen, **Ewoud van Haaften**, **Maxim Kamst** and **Jaco Vaalburg** for giving feedback on my thesis. From some point it is difficult to review your own work, or to see your own mistakes. Thank you very much that you were willing to make time to review my thesis. You came up with some very useful feedback.

Abstract

In a world with an increasing population and level of welfare, there is a large demand for more and cleaner sources of energy. Floating wind turbines have great potential to meet a significant part of this demand. They are however not yet commercially available, because of huge technical and economic challenges. Most of the concepts that are currently developed focus on technical feasibility.

The TetraSpar concept is designed with a focus on both technical and economic challenges. One of the main advantages of the concept is the type of connection, with which the steel tubular members are connected. This connection allows for industrialization of the fabrication and assembly process, which is potentially a huge competitive advantage. However, there are major concerns about the fatigue strength. The variable nature of the environmental loads, and the dynamic behavior of a floating structure result in continuously varying internal forces, which could cause significant fatigue damage

The fatigue strength of the pin connection is assessed in the research project presented in this thesis. The fatigue strength is quantified by an estimated fatigue lifetime, which is the expected time to failure of the most critical point in the connection. The lifetime is estimated based on the yearly accumulated fatigue damage. A computer model of the structure has been constructed, with which time signals of the internal forces in the structure are calculated, based on the environmental loads.

The pin connection was not included in this model, so internal forces in the steel tubular members have been translated manually to forces in the pin connection. The connection was decomposed in its basic components and nine potential critical locations have been identified. Stress concentrations are expected at these locations, which make them sensitive to fatigue. The internal forces were combined with the dimensions of the components, so that nominal stresses could be calculated. The hotspot stress at the potential critical locations was estimated with stress concentration factors (SCFs), which are found in literature. Relationships between the internal force and the hotspot stresses are derived in this way, and time signals of the hotspot stresses are obtained. Most of the identified locations could be assessed with hand calculations, except for two locations. They are analyzed with finite element software (ANSYS). The time signals of the hotspot stresses have been used to calculate the expected fatigue damage with the Palmgren-Miner rule. The damage is calculated for all wave directions and based on real wave statistics.

Results have shown that there are two locations in the design that have an expected fatigue life time of less than 100 years. None of them have an expected lifetime of less than 60 years, which is the absolute minimum according to the standard for floating offshore wind turbines. Although results are expected to be conservative, one of the recommendations is to do a more detailed stress analysis on the critical locations in the pin connections, because fatigue problems are very sensitive to input by nature.

Nomenclature

Abbreviations

ANSYS	Finite element software package
DFF	Design Fatigue Factor
DNV	Det Norske Veritas
DOF	Degree of Freedom
FE	Finite Element
FFT	Fast Fourier Transform
FS	Force-Stress relationship
IF	Irregularity Factor
IFFT	Inverse Fast Fourier Transform
JONSWAP	JOint North Sea WAve Project
MATLAB	Mathematical software package
MSL	Mean Sea Level
N.A.	Neutral Axis
PCC	Pearson's Correlation Coefficient
PSD	Power Spectral Density
SCF	Stress Concentration Factor
SOT	Stiesdal Offshore Technologies
StdDev	Standard Deviation
USFOS	Finite element software package

Greek symbols

α	angle
ζ_a	wave amplitude
η	sea surface elevation
μ	mean value
ρ	density
σ	stress (or standard deviation)
τ	shear stress
ϕ	velocity potential
ω	wave frequency

Latin symbols

a	wave particle acceleration
A	area
C_d	drag coefficient
C_m	mass coefficient
D	damage (or diameter)
e	eccentricity
E_p	expected number of peaks
f	frequency
F	force
F_s	Sampling frequency
g	gravitational acceleration
H_{eq}	equivalent wave height
H_s	significant wave height
I	second moment of area
k	wave number
$\mathbf{K}$	stiffness matrix
L	length of stress signal (or distance)
m	fatigue strength parameter
m_n	n^{th} order spectral moment
M	moment
n	number of stress cycles in signal
N	maximum number of stress cycles
r	distance
R	radius
t	time (or wall thickness)
T_{eq}	equivalent peak period
T_p	peak period
T_z	zero crossing period
u	wave particle velocity
$\bar{u}$	vector with node displacements of FE model
W	section modulus
y	distance from neutral axis
z	depth from sea surface

List of Figures

1.1 Some concepts for floating wind turbines [2] . . . 2
1.2 The TetraSpar concept, developed by SOT . . . 2
1.3 Different types of pin connections in the TetraSpar concept . . . 3
1.4 Example of fatigue damage . . . 3
1.5 Test location 10 [km] offshore Norway . . . 4

2.1 Pin connections that allow for a quick and easy assembly process . . . 6
2.2 TetraSpar concept with the main components . . . 7
2.3 Floater structure with the different types of members . . . 8

3.1 General flow diagram for the fatigue strength analysis . . . 11
3.2 USFOS model with all the phenomena that should be assessed . . . 13
3.3 Approach for the calculation of external loads on the structure . . . 15
3.4 Directional spread of the wave data at the test location . . . 16
3.5 Scatter diagram of the sea state statistics at the test location . . . 16
3.6 Wave scatter diagram divided into eight blocks . . . 17
3.7 Symmetry of the geometry is used, so that there are only 3 unique wave directions 18
3.8 Example of a JONSWAP spectrum . . . 18
3.9 Graphical representation of the method to obtain an approximation of the sea surface elevation from a wave energy spectrum . . . 19
3.10 The calculation of internal forces is the second step in the general flow diagram . . 20
3.11 Comparison between the real geometry and the USFOS geometry. Internal forces are read out at the dashed lines . . . 21
3.12 Sample of the internal force data that is transferred to Excel and MATLAB . . . 21
3.13 Approach that is followed for calculating stresses . . . 22
3.14 The equilibrium of section A-A is used to calculate the forces in the pin connections 22
3.15 Example of a stress hotspot in an axially loaded plate. The lines are a visualization of the stress distribution . . . 23
3.16 Approach that is followed for calculating the fatigue damage . . . 23
3.17 SN-curves for the different detail classes . . . 24
3.18 Graphical representation of the Rainflow counting method . . . 25
3.19 Caption . . . 26
3.20 Number of occurrences per year for different the stress ranges . . . 28
3.21 Yearly damage per stress range . . . 28

4.1 The four connection types in the design . . . 30
4.2 Sample of the time signal of the variation of the internal forces in the lateral member 30
4.3 Flow diagram that shows the steps for the calculation of the stresses in this chapter 31
4.4 Terminology for the components in the pin connections . . . 31
4.5 Weld between the lateral member and the casting . . . 32
4.6 Potential critical point at the thickness transition of the lower ear . . . 33
4.7 The equilibrium on cross-section A-A is used to derive the forces in the ear parts . 34
4.8 Forces on the lower ear with the critical location indicated in red . . . 34
4.9 The critical locations in red result from a tensile stress . . . 35
4.10 Shear load mechanism documented in [23] . . . 36
4.11 Top and side view of the locations next to the hole in the fork . . . 37
4.12 Resultant of the distributed load and the arm to the critical location . . . 37

4.13 The equivalent axial force is decomposed in perpendicular and parallel component 37
4.14 Schematic representation of the critical spot at the base of the fork 38
4.15 Ring stiffener at the inside of the radial member 38
4.16 Free body diagram of the casting that is welded in the radial member 39
4.17 Top view of the casting showing the force transfer of the perpendicular force . . . 40
4.18 The perpendicular of the force is assumed to be transferred through only a part of the weld 40
4.19 The force transfer to the ring stiffener is similar to this situation [23] 40
4.20 Cross-section at the critical location of the welds. The welds are indicated with red lines. 41

5.1 Part of the structure that is considered for the FE analysis 44
5.2 Detail of the radial member end with the forces of the connected elements 44
5.3 Potential critical locations that are considered in the FE analysis 44
5.4 ANSYS model with the boundary condition and the symmetry condition 45
5.5 Mesh of the ANSYS model (1) 45
5.6 Mesh of the ANSYS model (2) 45
5.7 General flow diagram for the FE analysis 46
5.8 Flow diagram for the calculation of the Force-Stress relationship 47
5.9 Graphical representation of the load cases 48
5.10 Example of the observed stress pattern from an FE analysis 49
5.11 Geometrical discontinuity between the casting and the radial element 50
5.12 Explanation of the hotspot method to estimate the hotspot stress 50
5.13 Sample of the five force signals 53
5.14 Variation of the stress signal for hotspot 1 54
5.15 Variation of the stress signal for hotspot 2 54

6.1 Variation of the stress signals of both methods 58
6.2 Schematic representation of a stress path starting at the hotspot 59
6.3 Stress on the in- and outside of the radial member as a function of the distance along the stress path 60
6.4 Visualization of the local load effects 60
6.5 Stress path from the FE model, corrected for the local effects 61
6.6 Definition of the path along which the stress distribution is checked 62
6.7 Stress distribution along the path. The dashed lines indicate the locations of the castings 62
6.8 The stress distribution is decomposed in an axial stress and a bending stress . . . 63
6.9 Stress distributions of the FE analysis and the theoretical distribution calculated with Eq. (6.8) 64
6.10 Connection as modelled in USFOS 65
6.11 Real geometry of the connection 65

7.1 Flow diagram with the steps for the fatigue damage calculations 67
7.2 Definitions of the wave directions and the numbers of the pin connections 68
7.3 Original approach to reduce the number of simulations 68
7.4 Alternative method for the calculation of the results 69
7.5 Linear relationships between significant wave height and standard deviation for the relevant T_p-values 69
7.6 Identified locations that are potentially sensitive to fatigue damage 70
7.7 Reduced wave scatter diagram 71
7.8 Relative damage results for a single sea state 71
7.9 Fatigue damage diagram with the yearly fatigue damage (in 10^{-3}) for each sea state 72
7.10 Results for the most critical locations for the 0°wave direction 73
7.11 Directional spread of the waves 74
7.12 The symmetrical geometry is used, so that simulations are limited to only 3 unique wave directions 74
7.13 Yearly accumulated damage per wave direction for connection 1 75
7.14 Yearly fatigue damage considering all wave directions 76
7.15 Expected damage per year for the critical locations in all three connections 76

A.1 SCF diagram for a component with a thickness change 91
A.2 SCF diagram for a lug connection 92

B.1 Equivalent axial force on the lower casting decomposed in a parallel and perpendicular component 93
B.2 Free body diagram of the casting 94
B.3 Model used to calculate forces on the casting 94

D.1 Fatigue damage diagram for location 1 for the 0°wave direction only 101
D.2 Fatigue damage diagram for location 3 for the 0°wave direction only 101
D.3 Fatigue damage diagram for location 8 for the 0°wave direction only 101
D.4 Fatigue damage results per wave direction for connection 1 102
D.5 Fatigue damage results per wave direction for connection 2 102
D.6 Fatigue damage results per wave direction for connection 3 103

List of Tables

2.1 Wind turbine characteristics 8
2.2 Floater characteristics 9
2.3 Dimensions of the members in the floater 9
2.4 Main characteristics of the keel 9
2.5 Characteristics of the two segments of the mooring chain 9

3.1 Equivalent paramters for the blocks in the wave scatter diagram 17

4.1 The different type of connections in the structure 30
4.2 Summary of the results for the potential critical locations 42

5.1 Loads on the radial member 47
5.2 Overview of the load cases with the standard deviations of the forces 48
5.3 Normal stress results for location 1 52
5.4 Shear stress results for location 1 52
5.5 Normal stress results for location 2 52
5.6 Shear stress results for location 2 52
5.7 Correlation coefficients for the full force signals 53
5.8 α-values for the force signals 53
5.9 Results of the mesh convergence test 55

6.1 Input and assumptions for the two methods of stress calculation 58
6.2 Correlation coefficient and ratio between the standard deviations of the stress signals 58
6.3 Axial force and bending moment for the two methods 63
6.4 Summary of the findings in this chapter 66

7.1 Relative damage results for a single sea state 70
7.2 Results for the most critical locations for the 0°wave direction 72
7.3 Probability of the wave directions 73
7.4 Combined results for the critical locations for all wave directions 74
7.5 Comparison between the results for all the wave directions and the 0°direction only 75
7.6 Expected fatigue life times, considering all wave directions, for the critical locations in all three connections. 75
7.7 Critical locations with an expected fatigue lifetime of less than 120 years 77

C.1 All the load components on the radial member end 97
C.2 Difference in hotspot stresses for LC4 and LC5 97

D.1 Results for all identified locations for the 0°wave direction 100
D.2 Results for all identified locations for the 30°wave direction 100
D.3 Results for all identified locations for the 180°wave direction 100
D.4 Results for all locations, wave directions and connections 103

Contents

Abstract i

Nomenclature iii

List of Figures v

List of Tables ix

1 Introduction 1
- 1.1 Fatigue . . . 3
- 1.2 Objectives . . . 3
- 1.3 Prototype . . . 4

2 The concept 5
- 2.1 Unique aspects . . . 5
- 2.2 Pin connection . . . 6
- 2.3 Design & Geometry . . . 6
  - 2.3.1 Wind Turbine . . . 8
  - 2.3.2 Floater . . . 8
  - 2.3.3 Keel . . . 8
  - 2.3.4 Mooring . . . 10

3 Theory 11
- 3.1 USFOS model . . . 12
- 3.2 External loads . . . 15
  - 3.2.1 Environmental data . . . 15
  - 3.2.2 Load cases . . . 15
  - 3.2.3 Blocks . . . 17
  - 3.2.4 Sea surface elevation . . . 17
  - 3.2.5 Hydrodynamic loads . . . 18
  - 3.2.6 Incorrect equivalent parameters . . . 20
- 3.3 Internal forces . . . 20
- 3.4 Stress calculation . . . 20
  - 3.4.1 Forces in connections . . . 20
  - 3.4.2 Nominal stress . . . 22
  - 3.4.3 Hotspot stress . . . 22
- 3.5 Fatigue damage . . . 23
  - 3.5.1 Palmgren-Miner rule . . . 23
  - 3.5.2 SN-curves . . . 24
  - 3.5.3 Stress signal components . . . 25
  - 3.5.4 Rainflow counting . . . 25
  - 3.5.5 Rayleigh approximation . . . 26
  - 3.5.6 Spectral moments . . . 26
  - 3.5.7 Comparison of methods . . . 27
  - 3.5.8 Damage calculation . . . 28

4 Hand calculated stresses **29**
4.1 Considered connection . . . 29
4.2 Method . . . 31
4.3 Ear part of the connection . . . 31
4.3.1 Weld between casting and element . . . 31
4.3.2 Minimum cross-section . . . 33
4.3.3 Hole in the ear . . . 35
4.4 Pin . . . 35
4.5 Fork . . . 36
4.5.1 Hole in the fork . . . 36
4.5.2 Base of the fork . . . 37
4.6 Casting - radial member connection . . . 38
4.6.1 Perpendicular component . . . 38
4.6.2 Parallel component . . . 39
4.7 Summary . . . 42

5 Finite element modelling **43**
5.1 Objective . . . 43
5.2 Model . . . 43
5.3 Method . . . 46
5.4 Loads . . . 47
5.5 Hotspot stress . . . 48
5.6 Results . . . 51
5.7 Force-stress relationship . . . 51
5.8 Mesh convergence . . . 55

6 Comparison of methods **57**
6.1 Differences . . . 59
6.1.1 Local bending moment . . . 59
6.1.2 Stress distribution . . . 61
6.1.3 Axial force and moment transfer . . . 62
6.1.4 Bending moment difference . . . 64
6.2 Conclusion . . . 65

7 Results **67**
7.1 Method of calculation . . . 67
7.1.1 Alternative method . . . 68
7.2 Single sea state . . . 68
7.3 Single wave direction . . . 70
7.4 All wave directions . . . 73
7.4.1 All Connections . . . 75
7.5 Conclusions . . . 75

8 Discussion of results **79**
8.1 Sensitivity . . . 79
8.2 Limitations . . . 80

9 Conclusions & recommendations **83**

Bibliography **86**

Appendices **89**

A SCF diagrams **91**

B Alternative stress calculation **93**

C Additional load case FE analysis **97**

D All results **99**

Chapter 1

Introduction

Since the 1950's the world population has increased quickly to 7 billion people at the end of 2018. A further growth is expected for the coming decades, up to 10 billion in 2070 [5]. This, in combination with the average increase of the welfare, results in an increasing global energy consumption. At the same time global warming, caused by climate change, is a severe problem. The climate change is mainly caused by the emission of greenhouse gasses. This emission is closely related to the global energy consumption.

To minimize the global warming, all nations have agreed to undertake ambitious efforts to minimize the emission of greenhouse gasses and to invest in green energy sources. This is the Paris agreement and it has been made in 2015. So, there is a need for either more and cleaner energy in the near future. Shell has the ambition to meet this need, which is why they have invested in the development of a concept for a floating wind turbine.

Wind energy is a source of green energy with a large potential. Originally, wind farms used to be built onshore only, but in the last two decades they have been built offshore as well. Due to stronger and more constant wind fields, and the wide availability of space, offshore wind farms are an attractive alternative for onshore wind farms. Currently, all commercial wind farms are bottom-founded. They can be operated at a competitive rate, but they have a major disadvantage. Bottom-founded wind turbines are limited to a water depth of around fifty meters. There are many locations around the world that have a great potential for offshore wind energy, but where the water is too deep to operate bottom-founded wind turbines. Floating wind turbines could be a great alternative for these locations. However, they have not yet been installed, because there are many challenges in the design of these turbines. These challenges concern dynamic behavior, stability, structural integrity and economics.

Some concepts for a floating wind turbine have been developed of which some examples are shown in Fig. 1.1. Many of these concepts however, might be technically feasible, but are expected to be expensive to fabricate, install and operate. The Danish company Stiesdal Offshore Technologies (SOT) has developed a concept for a floating wind turbine that overcomes many of the technical challenges and could be commercially attractive as well. It is called the TetraSpar and it is shown in Fig. 1.2. Shell has decided to become a shareholder in this project, because of the great potential. They provide financial support, but also technical support, by doing technical parallel studies. This master thesis is an example of such a study.

One of the technical parallel studies is focused on the pin connections in the TetraSpar concept (Fig. 1.3). This type of connection allows for pre-fabrication of the steel members in the design, so that there is no need for welding in the assembly process. It is a very economical solution, because costs of assembly and quality control are greatly reduced. However, there are concerns about the structural integrity of this connection, mainly with regards to the fatigue strength. In this thesis, the fatigue strength of the pin connection is assessed. It aims to identify the potential critical locations in the connection and to predict the time to failure, which is also called the expected fatigue life. The outcomes of this study can be used as a confirmation of the integrity of the design or it can form a basis for an improvement of the design.

Figure 1.1: Some concepts for floating wind turbines [2]

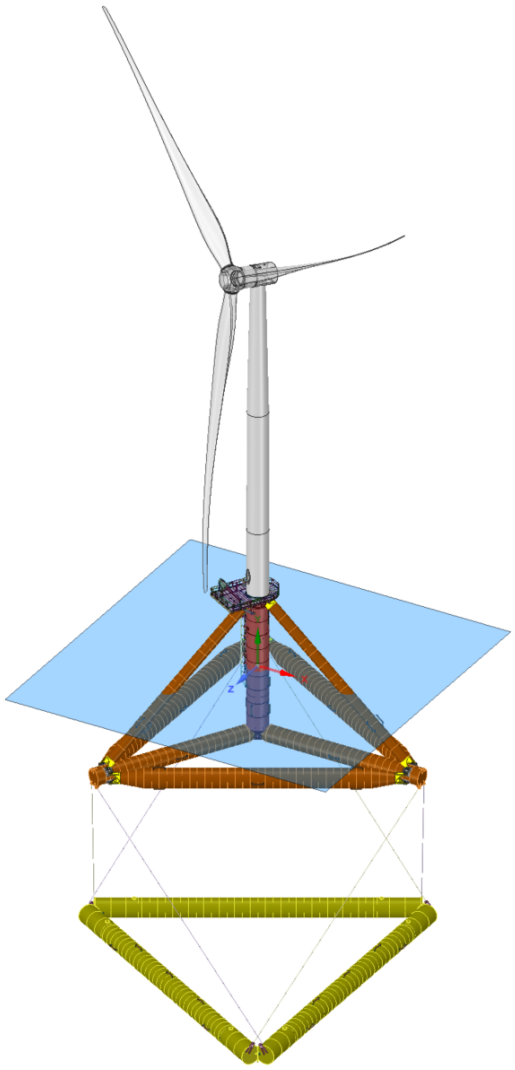

Figure 1.2: The TetraSpar concept, developed by SOT

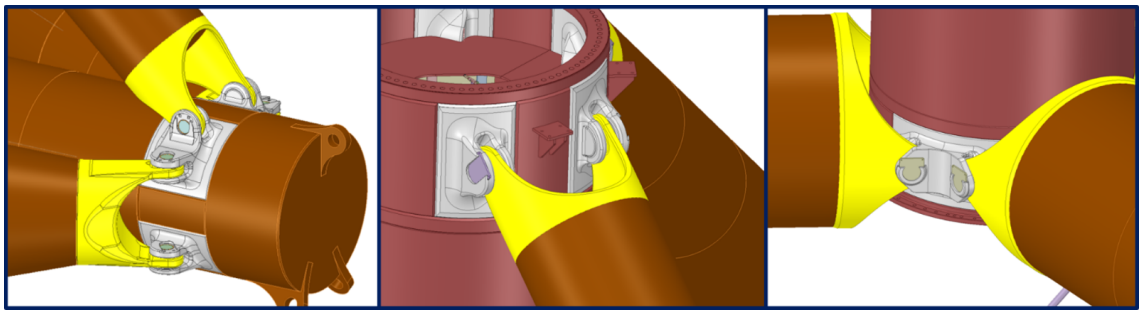

Figure 1.3: Different types of pin connections in the TetraSpar concept

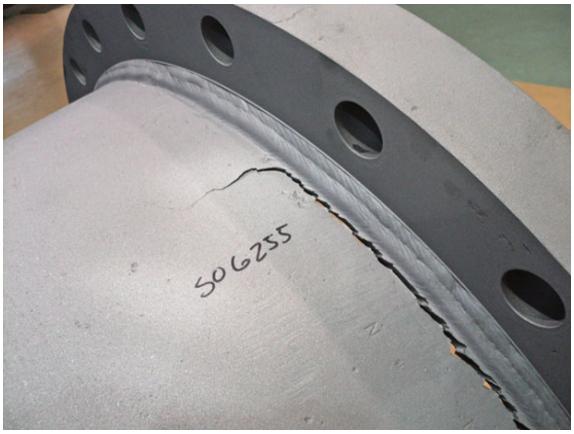

Figure 1.4: Example of fatigue damage

1.1 Fatigue

One of the biggest challenges in the design of offshore structures is fatigue. An example of fatigue damage of a steel structure is shown in Fig. 1.4. *Fatigue failure is the tendency to fracture by means of progressive brittle cracking under repeated alternating of cyclic stresses of an intensity considerable below the normal strength* [6]. Offshore structures are cyclically loaded by waves during their whole lifetime. Assuming an average wave period of 10 seconds, an offshore structure with a typical lifetime of 20 years experiences around 60 million load cycles. The fatigue strength of the structure is therefore an important design challenge. For floating structures, this challenge is even bigger. Weight of the structure is a more strict boundary condition, so it is usually difficult to add extra material at critical locations to lower the stress levels. These statements emphasize the importance of a good structural design and the relevance of the study that is done in this thesis.

1.2 Objectives

The main objective of the research presented in this thesis is to determine whether the fatigue strength of the pin connection is sufficiently high to survive it's design life time. This objective is formulated as follows and consists of several parts.

Assess the fatigue strength of the pin connection in the design of the TetraSpar concept.

- Find the most critical connection in the design
- Decompose the complex connection in its components and understand how loads are transferred
- Identify potential critical locations where stresses are concentrated
- Estimate the stress level at these locations

- Calculate the fatigue damage based on the recommendations in DNV-RP-C203 [23] and determine the expected fatigue life

In order to achieve the research objectives, a model of the TetraSpar is used, that generates input for a MATLAB script. The model is constructed by an engineer in the TetraSpar project team of Shell. The model calculates internal forces in the structure that result from the environmental loads. The internal forces are transferred to MATLAB. A script is developed with which stresses and fatigue damage are estimated. The final outcome - the expected fatigue life of the pin connection based on realistic environmental conditions - is calculated by combining results from different environmental conditions and directional data with the corresponding probability of occurrence. With these results, conclusions can be drawn with regards to the expected fatigue life of the pin connections.

1.3 Prototype

The design of the concept is still to be tested. A full-scale prototype is currently being built that will be installed offshore, for real life measurements. The prototype will be tested at the same test location that has been used for the Hywind project. The Hywind project is currently the only operational commercial floating wind farm, consisting of five floating wind turbines. The test location is approximately 10 [km] offshore Norway, see Fig. 1.5

Figure 1.5: Test location 10 [km] offshore Norway

Chapter 2

The concept

Offshore floating wind turbines are a topic for many research projects since several years. There are many technical and economic challenges that should be dealt with, before floating wind turbines can be operated on a large scale. Most of the research has focused around technical aspects. This has led to the development of several floating wind turbine concepts. Many of these concepts are designed against technical challenges, and to a lesser extent against economic challenges. It is expected that the production and installation of these concepts will be expensive and might not even be commercially attractive (enough).

The TetraSpar concept is designed with an extensive focus on a cost-effective way of fabrication, assembly and installation. It is suitable for industrialization, so it is expected that it can deliver a more economic solution than the other concepts that are currently being developed.

In this chapter, the concept is presented and described. The first sections discuss the unique aspects and the potential weaknesses of the concept. In the last section the characteristics of the different parts of the design are discussed.

2.1 Unique aspects

The TetraSpar (shown in Fig. 2.2) is a concept that offers the following unique advantages [20]. They are the main aspects that enable an efficient and cost-effective way of fabrication, assembly and installation, which allow for industrialization.

- The steel structure can be assembled in a time-efficient way, because of the pin connection. The pin connection is discussed in more detail in the next section
- The system can be completely assembled onshore. This includes the wind turbine, which is installed while the structure is floating at the quay side
- The structure is towed offshore using tug boats. No expensive offshore installation vessels are required
- The draft is minimized by holding the keel to the floater, up until the point of tow-out. This offers advantages with regards to the assembly, installation and inspection
- The system is moored with a simple catenary mooring system

Other advantages, that are not related to the industrialization, are listed below.

- With the open structure of the floater, the loads of waves are minimized
- The keel that is used for ballasting offers attractive dynamic properties
- Decommissioning is easily done by reversal of the installation process
- With small modifications, the design can also be deployed as a bottom-founded foundation

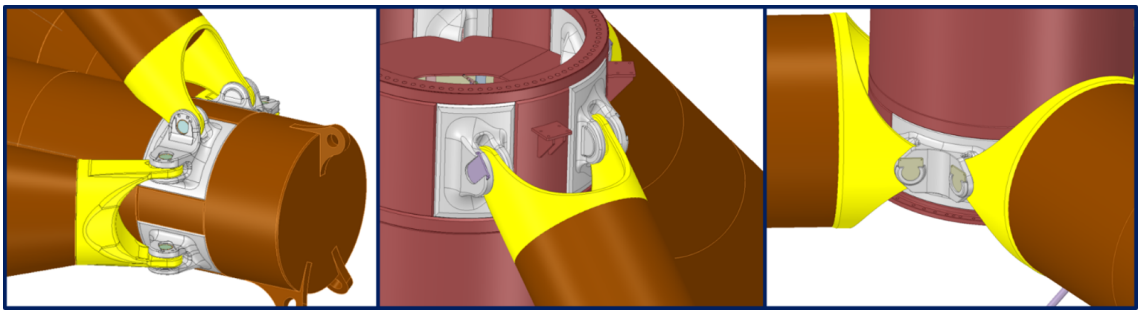

Figure 2.1: Pin connections that allow for a quick and easy assembly process

2.2 Pin connection

The main advantage of the TetraSpar concept is the efficient assembly process, which is supported by the pin connection (shown in Fig. 2.1). This type of connection allows for pre-fabrication of the steel members, so that they arrive as "LEGO-blocks" at the construction site. On sight, they only need to be assembled, using the pins of the connection; there is no need for welding activities in the assembly process. The steel members are simply connected by means of pins, using regular land cranes. The absence of welding activities at the construction site offers several advantages. The number of man-hours used for the assembly is expected to be significantly reduced. Furthermore, there is no need for quality control of welds at the construction site and the level of safety is increased.

However, there are concerns about the structural integrity of the pin connections, and specifically about its fatigue strength. The geometry is less robust as a fully welded connection and large stress cycles are expected. The statements that are listed below show the relevance of the concerns about the fatigue strength.

- Fatigue failure is one of the most common failure mechanisms in structures (not only offshore)
- Fatigue damage is expected to occur at the pin connections
- The pin connections are essential for the structural integrity of the whole structure
- There is no redundancy
- There are 18 pin connections in a single TetraSpar design

The importance of these aspects becomes even more evident, considering that a typical wind farm consists of at least fifty wind turbines. Hence, the risk of a fatigue failure becomes even more significant. A possible risk mitigation could be intensive monitoring of the structure. However, extensive inspection and maintenance of the pin connections is difficult. In a single floater there are already 18 connections. Most of them are located below the sea surface, which makes it a more difficult and expensive to reach them. In the Oil & Gas industry, critical components would be inspected and maintained regularly. However, profit margins in the offshore wind industry are tight, which makes it difficult to set up a robust inspection and maintenance program.

It is concluded that the pin connection offers many advantages, that could result in a huge competitive advantage. However, concerns about the fatigue strength should be reduced, before the potential of this concept can be enabled. This emphasizes the relevance of the research discussed in this thesis.

2.3 Design & Geometry

The TetraSpar concept (shown in Fig. 2.2) consists of four main components: the wind turbine, the floater, the keel and the mooring system. The focus in this thesis is on the pin connections in the floater. In the next sub-sections, the four components are described. The presented information is derived from [17].

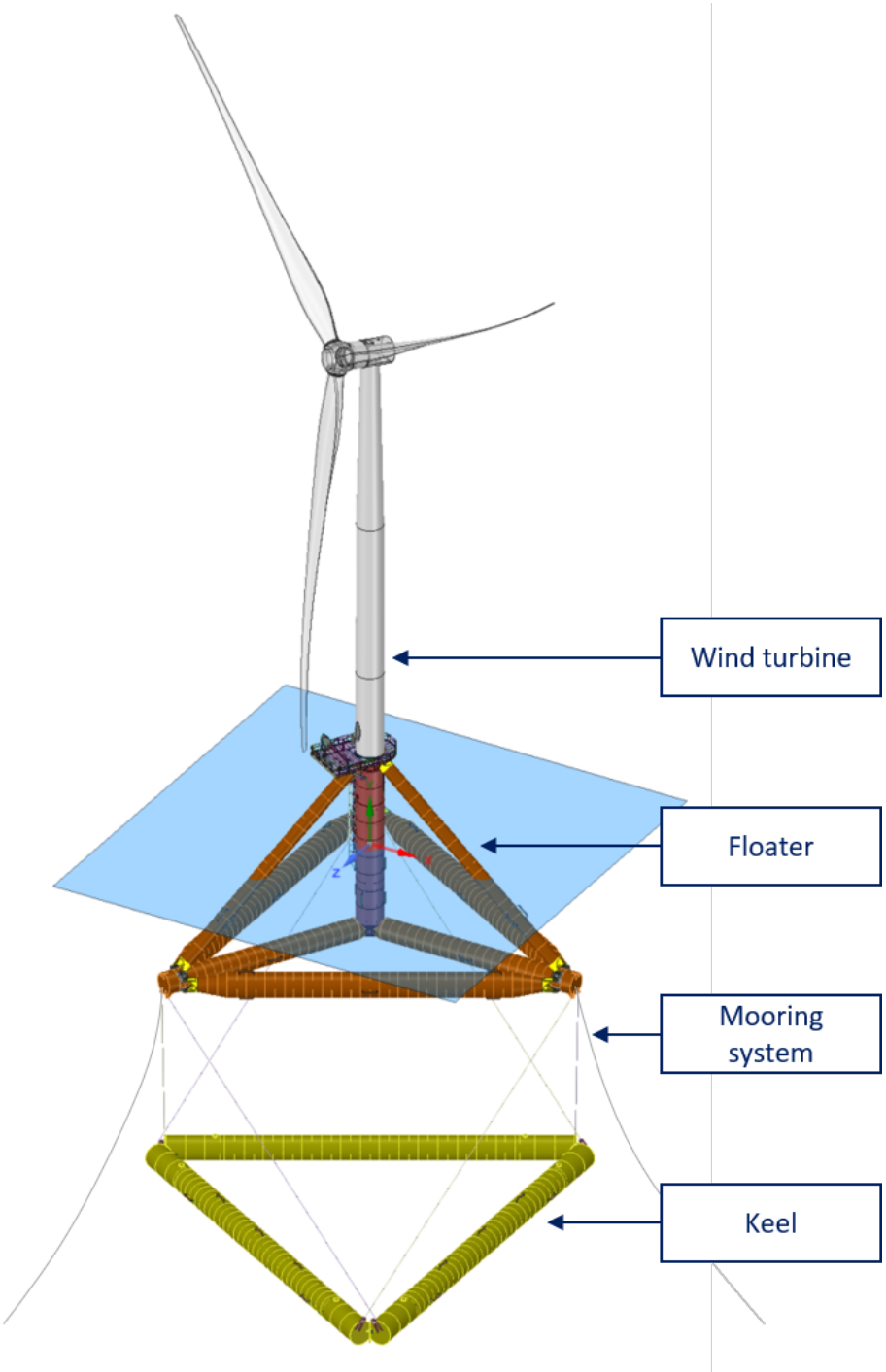

Figure 2.2: TetraSpar concept with the main components

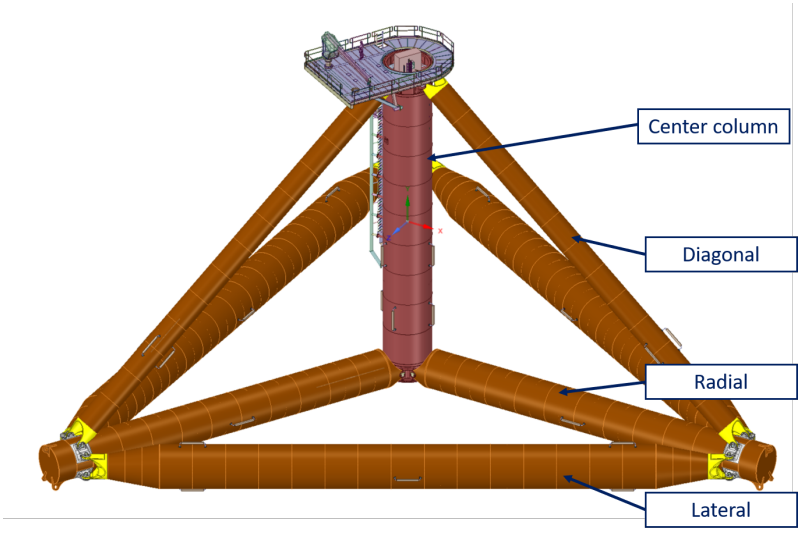

Figure 2.3: Floater structure with the different types of members

2.3.1 Wind Turbine

The wind turbine that will be used on the prototype is the Siemens Gamesa 3.6 MW [8]. It's main characteristics are shown in Table 2.1.

Table 2.1: Wind turbine characteristics

Description	Quantity	Unit
Power	3.6	MW
Configuration	3 blades	-
Rotor diameter	$\pm$ 130	m
Hub diameter	$\pm$ 3.3	m
Nominal rotor speed	12.2	rpm
RNA mass	265	tons
RNA elevation above MSL	93	m
Tower mass	208	tons
Tower COG above MSL	69	m

2.3.2 Floater

The floater consists of steel members with various lengths, diameters and wall thicknesses. Fig. 2.3 shows the floater with the names of the member types. The base is a vertical center column with three radial members attached to it, which make an angle of 120°with each other. The radial members are interconnected with lateral elements. Together they provide the main part of the buoyancy. The radial elements are also attached to diagonal elements, so that the structure forms a rigid body. On top of the floater there is a transition piece where the wind turbine and the floater are connected. The main characteristics of the members in the floater are shown in Table 2.2 and Table 2.3. The steel members are also equipped with internal ring stiffeners to prevent hydro static collapse.

2.3.3 Keel

The keel is attached to the floater with cables. The cables are Dyneema lines, and every suspension line is composed of two lines in parallel. The keel is ballasted and filled with concrete. Its purpose is to provide dynamic stability to the structure. The main characteristics of the keel are shown in Table 2.4.

Table 2.2: Floater characteristics

Description	Quantity	Unit
Mass	946	tons
Vertical distance COG below MSL	8.7	m
Displacement	3295	m^3
Floater draft	16	m

Table 2.3: Dimensions of the members in the floater

Element type	Outer diameter [m]	Wall thickness [cm]	Length [m]
Center column	4.3	2.6 – 6.0	± 35
Radial	3.5	2.0	± 35
Lateral	4.1	2.0	± 60
Diagonal	2.0	2.0	± 50

Table 2.4: Main characteristics of the keel

Description	Quantity	Unit
Dry mass	996	tons
Ballasted mass	1478	tons
Concrete mass	1067	tons
Displacement	840	m^3
Vertical distance COG below MSL	55.8	m

Table 2.5: Characteristics of the two segments of the mooring chain

Upper section	
Dry mass [kg/m]	140.4
Effective diameter [m]	0.151

Lower section	
Dry mass [kg/m]	750.0
Effective diameter [m]	0.350

2.3.4 Mooring

The mooring system consists of three catenary chain lines. Every mooring line consists of two segments. The lower part consists of three 107 [mm] chains and the upper section consist of a single 84 [mm] chain. The water depth at the location is approximately 210 meters. The characteristics of the mooring lines are shown in Table 2.5.

Chapter 3

Theory

In the introduction of this thesis, the main objective for the research have been formulated: to assess the fatigue strength of the pin connection. In this chapter, the approach for the fatigue strength analysis is discussed, and the theoretical background is explained. The main steps are shown in the general flow diagram in Fig. 3.1. They are discussed in more detail in the sections of this chapter.

The input for the analysis consists of the environmental conditions. They are summarized in a wave scatter diagram, tables with wind data and some site characteristic parameters. In the first step of the analysis, the environmental conditions are divided into load cases. The load cases are used to generate an approximation of the real conditions in the software package USFOS. Together with a model of the TetraSpar, the environmental loads on the structure are calculated. The external loads are translated to the internal forces in the members of the structure.

Internal forces are the input for the stress calculations in the pin connection. This is the main topic of this thesis. The connection is a complex assembly, in which stresses are not simply determined. To reduce the complexity, the connection is decomposed in its basic components, which are in general loaded in only one or two degrees of freedom. Stress distributions in the components can therefore be approximated with basic stress equations.

Based on literature and engineering knowledge, potential critical locations, also known as stress hotspots, are identified. Stresses are concentrated here, and fatigue damage is expected to initiate at these locations. The potential critical locations in all the components are listed, and hotspot stresses are calculated. Most of the hotspot stresses can be approximated with hand calculations, in MATLAB. The remaining locations are analyzed with the FE software package ANSYS.

The hotspot stresses for the potential critical locations form the input for the fatigue damage calculations, which are performed in MATLAB. The fatigue strength of the individual components is determined based on the accumulated fatigue damage per year. With these results, the objective of the presented research is achieved.

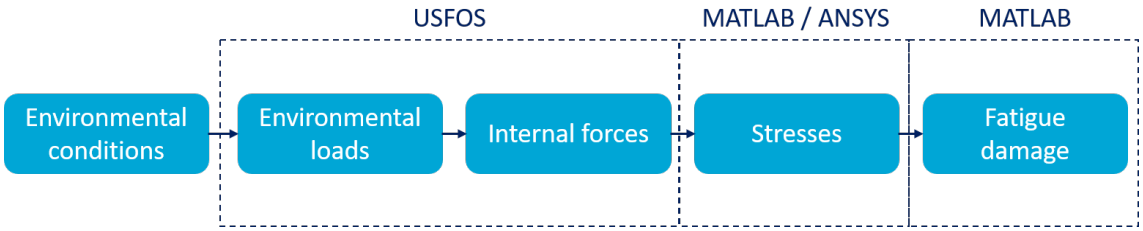

Figure 3.1: General flow diagram for the fatigue strength analysis

3.1 USFOS model

The first two steps in the general flow diagram are performed in USFOS. USFOS is a finite element software package, mainly designed to do load and motion analyses for steel tubular structures. A model of the TetraSpar concept in USFOS is used to calculate the internal forces in the members of the structure, based on realistic environmental conditions. This model is discussed in this section. It is explained how relevant phenomena are modeled and which assumptions have been made. The two steps in the flow diagram, in which internal forces are calculated from environmental conditions, are discussed afterwards.

Model description

Time signals of internal forces in specific members of interest are the output of the USFOS analyses. They form the basis for the stress signal calculation in the components of the pin connection. The stress signals are used to calculate the fatigue damage. The amount of fatigue damage is very sensitive to the variation of the stress signal, and thus indirectly also for the variation in the internal force signal. It is therefore important to have a clear overview of the phenomena that are included in the calculation of the internal forces and how they are modelled in USFOS.

Fig. 3.2 shows a model of the geometry and the actions and phenomena that are to be assessed for the modelling of the structure and conditions. For the presented research it is not realistic to model all of them accurately, so simplifications and assumptions are made. In the next paragraphs it is explained if the individual actions and phenomena from the figure have been considered, and how they are modelled.

Hydrodynamic loads

Hydrodynamic loads are expected to be the governing loads; they represent the external forcing on the structure. They are discussed in more detail in Section 3.2. It is explained how a wave field is generated and how the loads on the structure are calculated.

Wave direction

USFOS can simulate one wave direction at a time. This means that all the waves come from the same direction, without any spread. This is not a realistic representation of reality. However, it is expected that results will be conservative, because spread of wave directions is believed to result in a spread of (critically) loaded locations in the connections as well.

Wind loads

Wind loads have a large influence on the dynamic behavior and the internal forces in the structure. However, they are not considered in the simulations, for the following reasons:

- It is expected that wind loads do not produce significantly more or more severe internal force *fluctuations* than hydrodynamic loads only. Hydrodynamic loads are expected to be the main driver of fatigue damage. Note that it is expected that wind loads do have an influence on the (quasi-) static part of the internal forces, but these are not of interest for fatigue.
- The USFOS software cannot calculate the dynamic coupling between the motions of the support platform and the wind turbine. Instead, it approximates the combined effect of wind and wave loads by superposition. This approximation is not an accurate representation of reality [12].
- USFOS is not suitable for producing realistic wind fields. It is possible to simulate a constant, or semi-fluctuating wind field. A realistic wind field, that produces realistic load fluctuations on the structure, cannot be simulated however.

Omitting the wind loads also means that the wind-wave alignment and the dynamic effects of the wind turbine (blades) are not relevant. Note that only the wind loads are not considered. The wind turbine itself is modelled, to capture the behavior of the structure as accurate as possible.

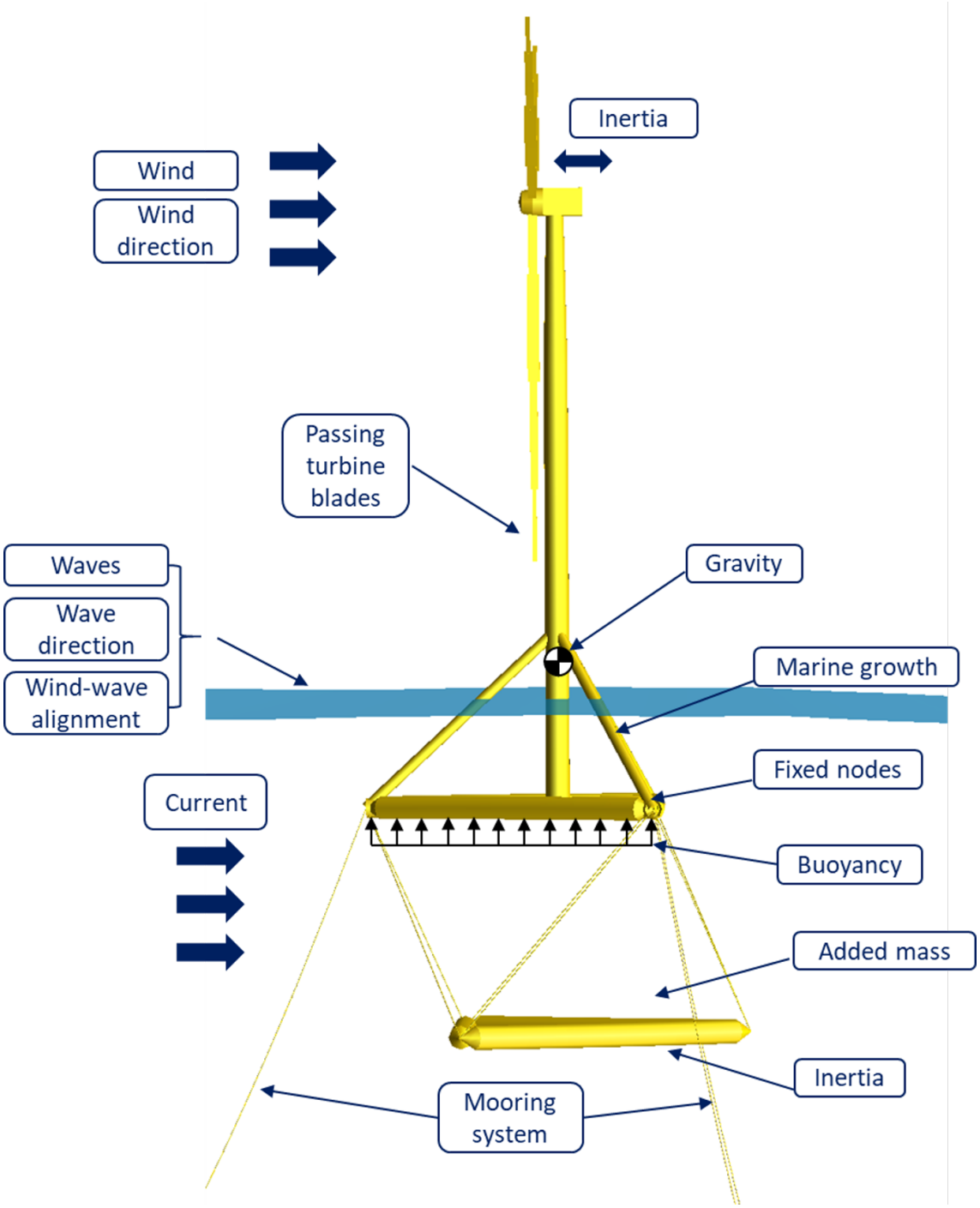

Figure 3.2: USFOS model with all the phenomena that should be assessed

Current

Currents are not considered in the USFOS model. They influence the total load on the structure, but they have no significant influence on the fatigue life of the structure, because the variability of the current velocity is negligible compared to the other loads. In [23] it is also stated that the effect of currents can be ignored for fatigue analyses.

Gravity and inertia

Inertia and gravity forces are considered in the simulations. The steel structure of the TetraSpar is modelled with the real dimensions, material properties and cross-sections, so that the model accurately represents the primary structure in terms of dimensions and masses. To account for materials other than the primary cross-section material (for example internal stiffeners), point masses have been defined at the end of the members. The gravity and inertia forces are calculated, based on the dynamics, dimensions and material properties of the members of the structure.

The wind turbine is modelled with multiple elements of different cross-sections and materials, to approximate the actual shape, mass and strength. It is also ensured that the most important characteristics of the wind turbine, the mass and the moment of inertia, are implemented accurately.

Buoyancy

Buoyancy is calculated using Archimedes' principle, which states that the buoyancy force is equal to the weight of the displaced fluid. For the model, this means that the software calculates the external volume of the submerged members. Buoyancy can also be removed from the internal volume, by specifying that the element is (partly) flooded. Buoyancy is assigned to all elements in the model, except for the keel, which is modeled (conform the actual design) with a flooded internal volume.

Fixed bottom node

In some simulations the structure started rotating about the vertical axis after a certain amount time. This happened also for wave directions for which the structure was symmetrically loaded. It is believed that this behavior is not an accurate representation of reality, and that it is a numerical error in the program. The mooring of the system is namely stiff compared to the force that the waves can exert on the structure. The floater is relatively "open" for the waves, which means that the area loaded by the waves is small. Therefore, the bottom node of the center column is restrained around the vertical axis (for the symmetrical load cases only), to prevent rotation in this direction.

Pin connections

USFOS is mainly designed to model structures with fixed joints. This means that no rotations are allowed and that moments are transferred through the connections between members. It is possible to implement hinges, but this is a cumbersome process and it increases the complexity of the model significantly. It is therefore decided to model all the joints in the structure as fixed connections, although some of them are hinges in reality (the pin connections). They allow rotation about one axis but act as moment restraint for the other axis, depending on the orientation. However, if it is assumed that the bending moment responses about the two axes are independent, one can simply ignore the bending moment around the axis that can freely rotate in reality. The fact that the moment distribution along a member changes as a result, is not relevant for the forces at the element ends.

Mooring system

The mooring system is considered as part of the structure in the model. The catenary chain lines are modeled as beam elements. They are modelled with an equivalent diameter and the realistic strength and material properties. The parts of the mooring lines that are lying on the seabed are modeled as being fixed in the USFOS model. This is done to improve the stability of the model

during the calculations. It is assumed that the heavy chain line will not come loose from the seabed.

Marine growth

USFOS provides the option to consider marine growth on the structure. Marine growth results in an increase of the element diameter and consequently the loads on the element. The significance of the effect depends on the marine growth thickness, with respect to the element diameter. In the structure of the TetraSpar, the elements with the smallest diameter are the diagonals, with a diameter of two meters. With a typical marine growth thickness of several centimeters the total diameter increases with only a few percent. The effect is expected to be negligible, and marine growth is therefore not considered in the model.

3.2 External loads

In this section it is explained how environmental conditions are generated in USFOS and how they are translated to the external loads exerted on the structure. This is the first step in the general flow diagram and consists of several sub-steps, as shown in Fig. 3.3. The sub-steps are discussed in the next sub-sections.

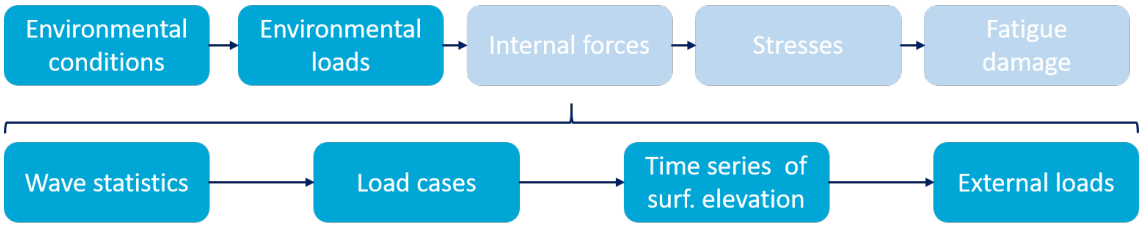

Figure 3.3: Approach for the calculation of external loads on the structure

3.2.1 Environmental data

The data about the environmental conditions at site is derived from a MetOcean report [14]. The water depth is around 210 [m]. Environmental conditions are available from offshore measurements offshore for the period October 1974 - June 1986. Also, hindcast data are available for the period 1957 – 2002. The model agrees well with the measurements during the overlapping period [14]. Wind, wave and current data can be extracted from this document. In the research presented in this thesis, only wave actions are considered. The wave scatter diagram and the directional spread of the waves, obtained from the hindcast data, are shown in Fig. 3.4 and Fig. 3.5.

3.2.2 Load cases

The wave scatter diagram in Fig. 3.5, is composed of many entries, each representing a sea state. Simulating all the sea states in USFOS would require too much time and computation effort, and therefore simplifications are made. This section describes the steps that are taken to reduce the number of simulations, and to define a number of load cases

A commonly used method divides the wave scatter diagram in blocks and lumps the sea states within the blocks. In [3] it is proposed that a block can be represented by equivalent fatigue damage parameters. It is stated that the fatigue damage is roughly proportional to the significant wave height to the power m, see Eq. (3.1). In this equation m is the fatigue strength parameter, which is equal to the slope of the SN-curves (refer to Section 3.5) that are used. The α-parameter is proportional to the number of stress cycles, which depends on the peak period of the sea state that is simulated.

$$d(H_s, T_p) = \alpha(T_p) H_s^m \tag{3.1}$$

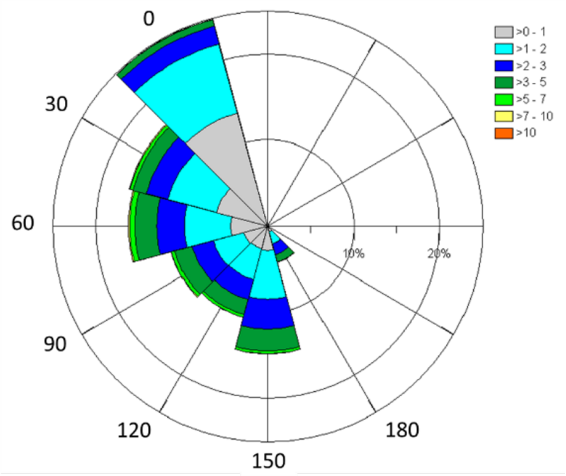

Figure 3.4: Directional spread of the wave data at the test location

Hs [m]		Tp [s]																			Sum	Cum
		2	3	4	5	6	7	8	9	10	11	12	13	14	15	16	17	18	19	20		
		3	4	5	6	7	8	9	10	11	12	13	14	15	16	17	18	19	20	21		
0	1	0.20	1.21	2.95	4.36	4.78	4.37	3.55	2.66	1.90	1.30	0.87	0.57	0.37	0.24	0.16	0.10	0.06	0.04	0.08	29.8	29.8
1	2	0.01	0.26	1.42	3.57	5.64	6.58	6.28	5.22	3.94	2.77	1.85	1.19	0.75	0.46	0.28	0.17	0.10	0.06	0.09	40.6	70.4
2	3		0.01	0.12	0.60	1.55	2.51	2.97	2.83	2.31	1.67	1.11	0.69	0.41	0.23	0.13	0.07	0.04	0.02	0.02	17.3	87.7
3	4				0.05	0.27	0.69	1.13	1.32	1.22	0.94	0.64	0.39	0.22	0.11	0.06	0.03	0.01	0.01		7.1	94.8
4	5					0.03	0.13	0.34	0.56	0.63	0.55	0.39	0.24	0.13	0.06	0.03	0.01				3.1	97.9
5	6						0.01	0.07	0.17	0.27	0.28	0.22	0.14	0.07	0.03	0.01					1.3	99.2
6	7							0.01	0.03	0.08	0.12	0.12	0.08	0.04	0.02	0.01					0.5	99.7
7	8									0.02	0.04	0.05	0.04	0.03	0.01						0.2	99.9
8	9										0.01	0.02	0.02	0.01	0.01						0.1	100.0
9	10												0.01	0.01							0.0	100.0
10	11																				0.0	100.0
11	12																				0.0	100.0
12	13																				0.0	100.0
13	14																				0.0	100.0
14	15																				0.0	100.0
Sum		0.2	1.5	4.5	8.6	12.3	14.3	14.3	12.8	10.4	7.7	5.3	3.4	2.0	1.2	0.7	0.4	0.2	0.1	0.2	100.0	
Cum		0.2	1.7	6.2	14.8	27.0	41.3	55.7	68.5	78.8	86.5	91.8	95.2	97.2	98.4	99.1	99.5	99.7	99.8	100.0		

Figure 3.5: Scatter diagram of the sea state statistics at the test location

Hs [m]		Tp [s]																			Sum	Cum
		2	3	4	5	6	7	8	9	10	11	12	13	14	15	16	17	18	19	20		
		3	4	5	6	7	8	9	10	11	12	13	14	15	16	17	18	19	20	21		
0	1	0.20	1.21	2.95	4.36	4.78	4.37	3.55	2.66	1.90	1.30	0.87	0.57	0.37	0.24	0.16	0.10	0.06	0.04	0.08	29.8	29.8
1	2	0.01	0.26	1.42	3.57	5.64	6.58	6.28	5.22	3.94	2.77	1.85	1.19	0.75	0.46	0.28	0.17	0.10	0.06	0.09	40.6	70.4
2	3		0.01	0.12	0.60	1.55	2.51	2.97	2.83	2.31	1.67	1.11	0.69	0.41	0.23	0.13	0.07	0.04	0.02	0.02	17.3	87.7
3	4				0.05	0.27	0.69	1.13	1.32	1.22	0.94	0.64	0.39	0.22	0.11	0.06	0.03	0.01	0.01		7.1	94.8
4	5					0.03	0.13	0.34	0.56	0.63	0.55	0.39	0.24	0.13	0.06	0.03	0.01				3.1	97.9
5	6						0.01	0.07	0.17	0.27	0.28	0.22	0.14	0.07	0.03	0.01					1.3	99.2
6	7							0.01	0.03	0.08	0.12	0.12	0.08	0.04	0.02	0.01					0.5	99.7
7	8									0.02	0.04	0.05	0.04	0.03	0.01						0.2	99.9
8	9										0.01	0.02	0.02	0.01	0.01						0.1	100.0
9	10												0.01	0.01							0.0	100.0
10	11																				0.0	100.0
11	12																				0.0	100.0
12	13																				0.0	100.0
13	14																				0.0	100.0
14	15																				0.0	100.0
Sum		14.8				26.6		27.2		18.0		8.6		3.2		1.1		0.5			100.0	
Cum		14.8				41.3		68.5		86.5		95.2		98.4		99.5		100.0				

Figure 3.6: Wave scatter diagram divided into eight blocks

Table 3.1: Equivalent paramters for the blocks in the wave scatter diagram

Block	1	2	3	4	5	6	7	8
H_{eq} [m]	1.31	1.83	2.39	2.96	3.38	3.40	2.88	2.01
T_{eq} [s]	5.0	7.0	9.0	10.9	12.9	14.9	16.9	19.4

3.2.3 Blocks

With the blocking of the wave scatter diagram comes a trade-off. On one hand, the blocks should be as small as possible to minimize the effect of the lumping strategy. On the other hand, it is efficient to have as few blocks as possible to minimize the computation time. A compromise is found for eight blocks, as shown in Fig. 3.6.

The sea states in the blocks are represented by an equivalent wave height and an equivalent peak period. These parameters should describe a sea state at the center of fatigue damage of the block. This means that the equivalent sea state results in the same fatigue damage as the sum of the damages of the individual sea states in the block (times their probability). The equivalent parameters are calculated with Eq. (3.2) and Eq. (3.3). Initially, the factor m in Eq. (3.2) was assumed to be equal to three[1]. The equivalent wave heights of the blocks have been calculated with this value and the results are shown in Table 3.1.

$$H_{eq} = \sum_{i=1}^{N} \frac{p_i}{p_{block}} \cdot H_{s,i}^{m} \qquad (3.2)$$

$$T_{eq} = \sum_{i=1}^{N} \frac{p_i}{p_{block}} \cdot T_{p,i} \qquad (3.3)$$

Fig. 3.4 shows that there are seven wave directions with a significant probability. However, using the symmetry of the geometry, the number of unique wave directions can be reduced to three, see Fig. 3.7. It is shown that the 0°, 30°and 180°are selected as the unique directions, whilst the other directions correspond with one these directions. It is assumed that the wave scatter diagram is independent of the wave direction. Consequently, there are 24 unique load cases, that are simulated in USFOS. They consist of the eight blocks (Fig. 3.6), for the three unique wave directions.

3.2.4 Sea surface elevation

A sea state represents a time series of three hours of the sea surface elevation. The sea state consists of a combination of waves with different periods, amplitudes and directions. The combination of the waves can be represented by a spectrum. A spectrum plots the relative amount of energy per wave period (or frequency, the inverse of the period). Different types of spectra are known, depending mainly on the geographical location. The most widely used spectrum for North Sea locations is the JONSWAP spectrum (refer to Fig. 3.8 for an example). For this spectrum type, the

[1]The value of three turned out to be incorrect. Refer to Section 3.2.6

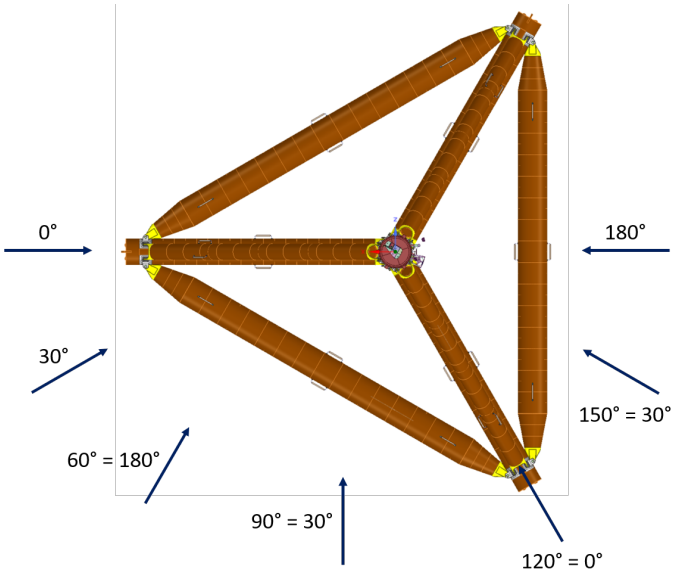

Figure 3.7: Symmetry of the geometry is used, so that there are only 3 unique wave directions

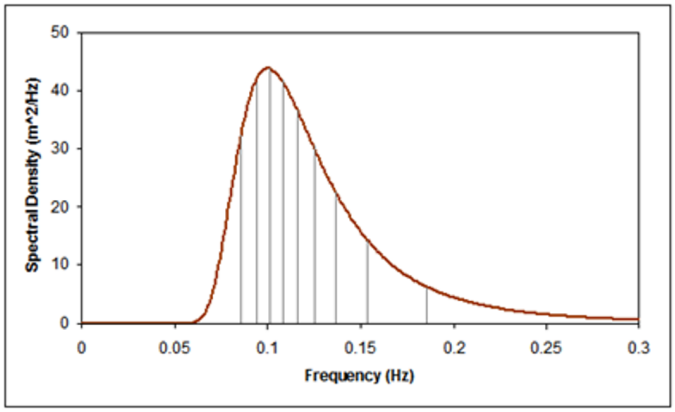

Figure 3.8: Example of a JONSWAP spectrum

peak period (or peak frequency) indicates the period at which the peak of the spectrum is found. The significant wave height is related to the total amount of energy present in the spectrum.
To generate a time series that approximates the sea surface elevation, the following approach is used in USFOS. The user specifies the spectrum type, the peak period, the significant wave height and the direction of the sea state, based on the site conditions. With these parameters, the wave energy spectrum is obtained. The time series is generated by taking an Inverse Fast Fourier Transform (IFFT) of the spectrum. The IFFT results in a set of discrete wave components. Each component is expressed as a harmonic wave with a wave amplitude, a wave frequency and a random phase angle. By superposition of all harmonic wave components, the surface elevation of the irregular sea is approximated. A visualization of this approach is shown in Fig. 3.9. Refer to Eq. (3.4) for the expression of the sea surface elevation.

$$\eta = \sum_{i=1}^{N} a_i \cdot cos(2\pi f_i \cdot t - \phi_i) \tag{3.4}$$

3.2.5 Hydrodynamic loads

The time series of the surface elevation, calculated by USFOS, is a signal with a duration of three hours. This time series is not fully simulated, because this would exceed the computational and data storage capacity. Instead, a sample of five hundred seconds of the full signal is simulated. To ensure that the sample is not non-conservative, USFOS searches in the full signal for the highest

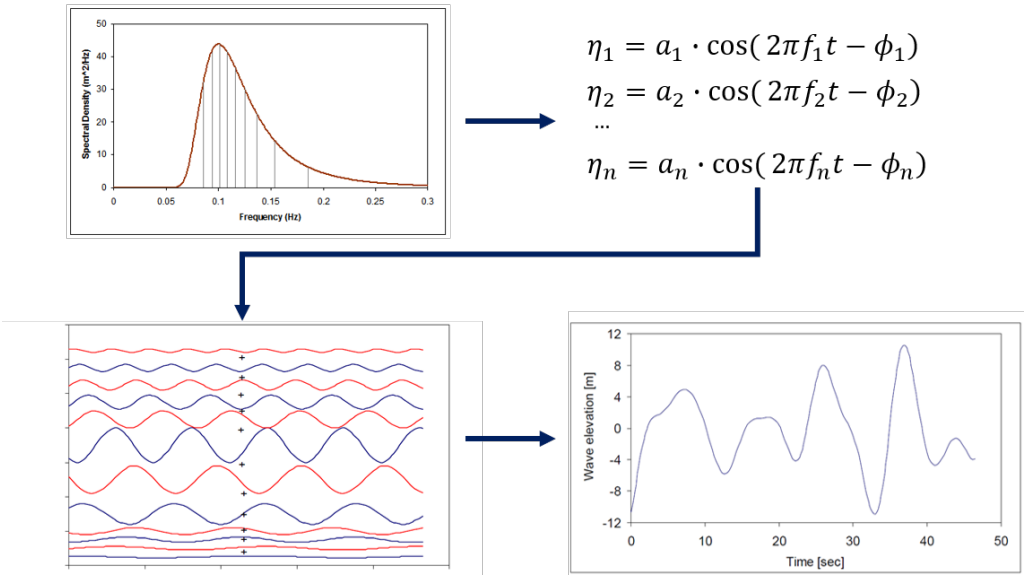

Figure 3.9: Graphical representation of the method to obtain an approximation of the sea surface elevation from a wave energy spectrum

wave and starts the simulation 100 seconds before this wave. Consequently, the highest wave in the time series is always considered in the simulation.

Variation of the sea surface elevation represent waves, which result in hydrodynamic loads on the structure. Wave forces are calculated with Morison's equation (Eq. (3.5)). This expression shows that the force on a piece of a cylindrical element consists of two parts. The first part is the inertia force, and the second part is the drag force. In the equation, the wave particle velocity (v_n) and acceleration (a_n) are the only variable terms. The other terms are the element diameter (D), the mass and drag coefficient (C_m and C_d) and the sea water density (ρ), which are all (assumed to be) constants.

The velocity and acceleration are calculated using potential flow theory. In this theory, *a potential function is defined as a continuous function that satisfies the basic laws of fluid mechanics: conservation of mass and momentum, assuming incompressible, inviscid and irrotational flow* [22]. The velocity potential function is shown in Eq. (3.6). In 2D, the horizontal and vertical components of the velocity can be obtained by taking the spatial derivative with respect to the x and z directions [10]. The accelerations are found in a similar way. Eq. (3.7) to Eq. (3.10) show the expressions.

USFOS automatically determines which part of the structure are 'wet', for every time step. Hence the total hydrodynamic load on a member is calculated by computing the integral of Eq. (3.5) over the wet part of the member.

$$dF = \left[\rho \frac{\pi}{4} D^2 C_M a_n + \frac{1}{2}\rho C_D D v_n |v_n|\right] dL \tag{3.5}$$

$$\phi = \frac{\zeta_a g}{\omega} \cdot \frac{cosh(k(h+z))}{cosh(kh)} \cdot sin(kx - 2\pi ft) \tag{3.6}$$

$$u_x = \frac{\partial \phi}{\partial x} \quad (3.7) \qquad u_z = \frac{\partial \phi}{\partial z} \quad (3.8) \qquad a_x = \frac{\partial^2 \phi}{\partial x^2} \quad (3.9) \qquad a_z = \frac{\partial^2 \phi}{\partial z^2} \quad (3.10)$$

3.2.6 Incorrect equivalent parameters

In Section 3.2 it is explained that the factor m in Eq. (3.2) is assumed to be equal to three. After calculation of the results, it turned out that this value is not accurate. It should be equal to the slope of the SN-curve, which effectively ranges between 3 and 5 (refer to Section 3.5), depending on the sea state. The calculated wave heights in Table 3.1 therefore underestimate the actual equivalent wave heights, because they are calculated with a fixed value of three.

Consequently, the equivalent wave heights in Table 3.1, are not at the center of fatigue damage of the blocks. For the USFOS simulations this does not lead to any problems. The results are valid for the sea state that is simulated, and they can also be used for the stress calculations. For the calculation of fatigue damage however, an alternative approach is used. This approach is discussed in Section 7.1.

3.3 Internal forces

The hydrodynamic loads on the structure result internal forces in the elements of the structure. In this section it is explained how the internal forces are calculated from the external loads. This is the second step in the general flow diagram, as shown in Fig. 3.10.

Figure 3.10: The calculation of internal forces is the second step in the general flow diagram

All the members of the TetraSpar structure are modelled with accurate dimensions and material properties. Based on these data, USFOS constructs the stiffness matrix for each element, which describes the mechanical properties. The stiffness matrix for the structure is obtained by combining the matrices of the elements. Hooke's law can then be used to solve the system, with the known stiffness matrix and the external loads, as shown in Eq. (3.11).

$$\bar{F} = \mathbf{K}\bar{u} \tag{3.11}$$

In this equation, F is the vector with the external forces distributed over the nodes in the model. K is the stiffness matrix of the full structure. The software calculates the node displacements, which are stored in the vector u. Element strains, stresses and internal forces are derived from the displacement vector. The internal forces and moments in the elements are the output of the USFOS model and they form the input for the calculation of the stresses.

The pin connections are not modeled in the USFOS model, as discussed in Section 3.1. Therefore, the internal forces close to the location of the connections, are derived. This is at the ends of the members, as shown in the lower panel of Fig. 3.11. At these locations, forces in six degrees of freedom are obtained, for every time step. The results from USFOS are transferred to Excel to put them in a clear overview. An example of this is shown in Fig. 3.12. The data is also transferred to MATLAB, where the internal forces are used for the stress calculations.

3.4 Stress calculation

The internal forces at the member ends that are extracted from USFOS are the input for the stress calculations, which is the third step in the global flow diagram. The stress calculations consist of several sub-steps, as illustrated in Fig. 3.13. In this section the sub-steps are discussed in more detail.

3.4.1 Forces in connections

The pin connections are not modelled in the USFOS model, because it would result in a too complex model. Therefore, the forces in the components of the pin connections are determined

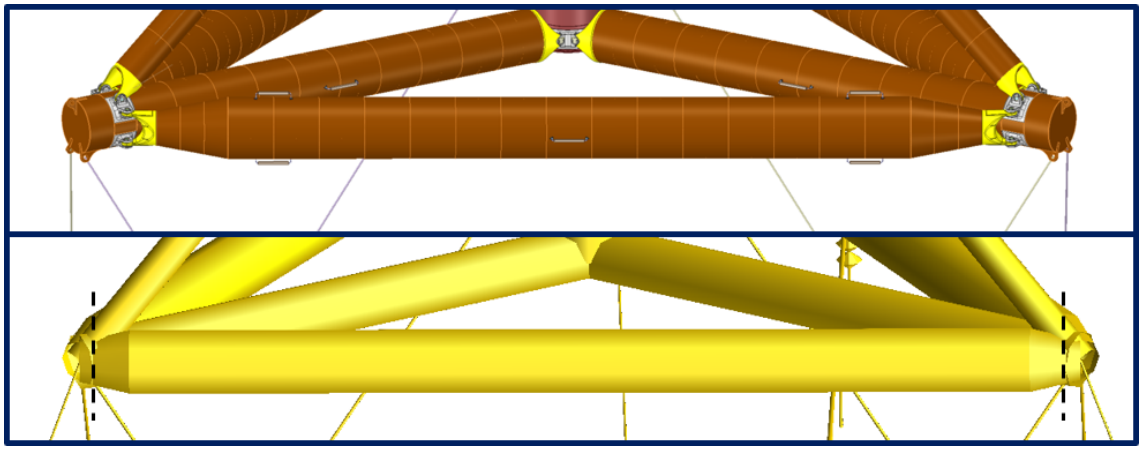

Figure 3.11: Comparison between the real geometry and the USFOS geometry. Internal forces are read out at the dashed lines

	NODE A						NODE B					
t [s]	Fx [N]	Fy [N]	Fz [N]	Mx [Nm]	My [Nm]	Mz [Nm]	Fx [N]	Fy [N]	Fz [N]	Mx [Nm]	My [Nm]	Mz [Nm]
0.0	1.33E+06	1.18E+05	-2.98E+06	3.81E+03	1.40E+07	8.08E+05	-1.33E+06	118094	-2.98E+06	3825.74	-1.40E+07	-8.08E+05
0.2	1.32E+06	1.35E+05	-3.00E+06	2.54E+03	1.41E+07	8.78E+05	-1.32E+06	135327	-3.00E+06	2565.05	-1.41E+07	-8.78E+05
0.4	1.31E+06	1.50E+05	-3.01E+06	1.44E+03	1.42E+07	9.30E+05	-1.31E+06	149945	-3.01E+06	1457.21	-1.42E+07	-9.30E+05
0.6	1.29E+06	1.58E+05	-3.04E+06	8.07E+02	1.43E+07	9.42E+05	-1.29E+06	158288	-3.04E+06	830.846	-1.43E+07	-9.42E+05
0.8	1.28E+06	1.70E+05	-3.07E+06	-1.34E+02	1.44E+07	9.81E+05	-1.28E+06	170380	-3.07E+06	-110.913	-1.44E+07	-9.81E+05
1.0	1.27E+06	1.82E+05	-3.09E+06	-1.08E+03	1.46E+07	1.02E+06	-1.27E+06	181769	-3.09E+06	-1060.45	-1.46E+07	-1.02E+06
1.2	1.26E+06	1.85E+05	-3.12E+06	-1.42E+03	1.47E+07	1.00E+06	-1.26E+06	185477	-3.12E+06	-1395.43	-1.47E+07	-1.00E+06
1.4	1.25E+06	1.89E+05	-3.15E+06	-1.85E+03	1.49E+07	9.93E+05	-1.25E+06	188712	-3.15E+06	-1820.43	-1.49E+07	-9.93E+05
1.6	1.24E+06	1.89E+05	-3.19E+06	-2.00E+03	1.51E+07	9.68E+05	-1.24E+06	188832	-3.19E+06	-1976.43	-1.51E+07	-9.68E+05
1.8	1.23E+06	1.81E+05	-3.19E+06	-1.65E+03	1.51E+07	8.91E+05	-1.23E+06	180743	-3.19E+06	-1626.81	-1.51E+07	-8.91E+05
2.0	1.22E+06	1.75E+05	-3.20E+06	-1.53E+03	1.51E+07	8.36E+05	-1.22E+06	174956	-3.20E+06	-1510.21	-1.51E+07	-8.36E+05
2.2	1.20E+06	1.67E+05	-3.22E+06	-1.16E+03	1.52E+07	7.69E+05	-1.20E+06	166751	-3.22E+06	-1142.4	-1.52E+07	-7.69E+05
2.4	1.20E+06	1.55E+05	-3.23E+06	-4.63E+02	1.52E+07	6.80E+05	-1.20E+06	154915	-3.23E+06	-439.739	-1.52E+07	-6.80E+05
2.6	1.20E+06	1.50E+05	-3.25E+06	-3.19E+02	1.53E+07	6.44E+05	-1.20E+06	149524	-3.25E+06	-297.285	-1.53E+07	-6.44E+05
2.8	1.20E+06	1.36E+05	-3.27E+06	5.73E+02	1.54E+07	5.54E+05	-1.20E+06	135780	-3.27E+06	594.802	-1.54E+07	-5.54E+05
3.0	1.20E+06	1.23E+05	-3.29E+06	1.38E+03	1.55E+07	476489	-1.20E+06	122951	-3.29E+06	1403.75	-1.55E+07	-4.76E+05

Figure 3.12: Sample of the internal force data that is transferred to Excel and MATLAB

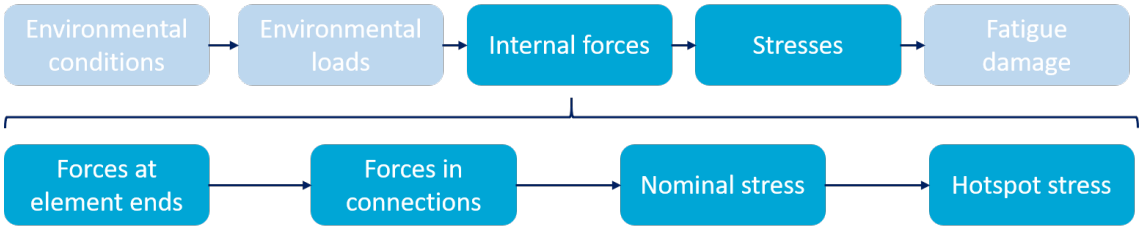

Figure 3.13: Approach that is followed for calculating stresses

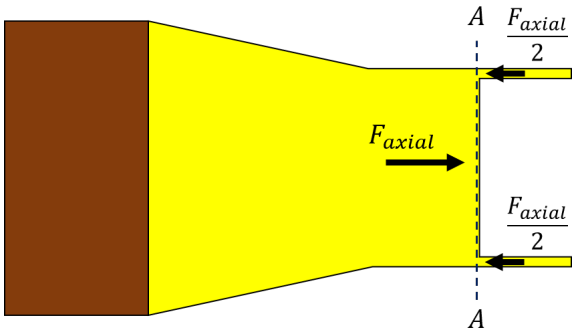

Figure 3.14: The equilibrium of section A-A is used to calculate the forces in the pin connections

manually, with equilibrium equations. An example is shown in Fig. 3.14, where the axial force in the ear of a pin connection is calculated based on the equilibrium on section A-A. From the previous section it is known that the forces are extracted from USFOS at cross-section A-A, which means that forces in six degrees of freedom are known at the left side of the cross-section. If the equilibrium of A-A is considered, the forces on the right side of the cross-section can be determined. A similar approach is followed for forces in other degrees of freedom, and for the other components in the pin connection.

3.4.2 Nominal stress

The nominal stress in a component is calculated based on the force on the component and its dimensions. For most of the components, the nominal stress is calculated with basic stress equations. The total stress is in general composed of an axial stress and a bending stress. The applied force is related to the stress in the component. The relationship between the force and the stress is used for the whole force signal, so that a stress signal is obtained. Note that only tensile stresses are considered for fatigue damage calculations. So, critical components or locations are identified, based on the (expected) highest tensile stress variations.

3.4.3 Hotspot stress

Nominal stress is no issue for a properly designed component. The dimensions are such that the stresses are at an acceptable level, and fatigue damage is not expected to be critical. However, there are features of a geometry that can result in an increased stress level. These are features such as holes, welds or a change in thickness or diameter. This results in stress concentrations zones, where stresses can be significantly higher than the nominal stress. Fatigue is expected to initiate at these locations. They are identified as potential critical locations or stress hotspots

It is difficult to calculate the magnitude of the hotspot stress. A common way to estimate the stress level at hotspots, is by means of a stress concentration factor (SCF). An SCF is multiplied with the nominal stress in the component, which is usually easy to estimate. Extensive research has been done on SCFs for all types of geometries. Approximate values, usually derived from experiments, are found in literature. The SCF depends mainly on the geometry of the feature and the dimensions of the component.

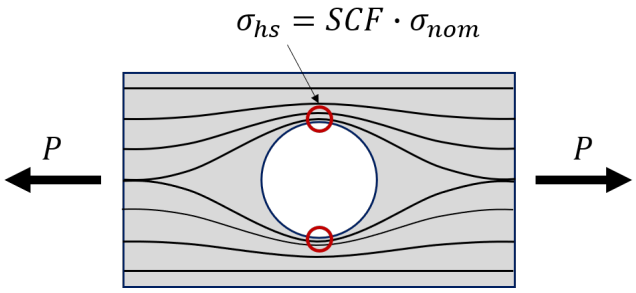

Figure 3.15: Example of a stress hotspot in an axially loaded plate. The lines are a visualization of the stress distribution

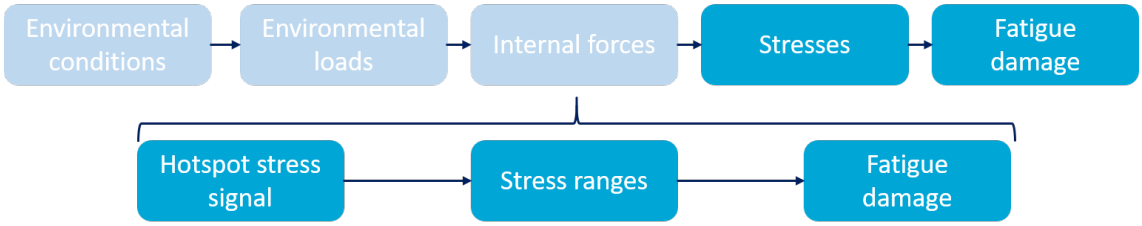

Figure 3.16: Approach that is followed for calculating the fatigue damage

An example of a stress hotspot is shown in Fig. 3.15. The figure shows an axially loaded plate with a hole in it. Stresses are concentrated in the locations next to the hole, that are indicated with red circles. The stress level is calculated based on the nominal stress and an SCF that is found in literature [15]. The nominal stress is equal to the load divided by the cross-sectional area at the hole, and the SCF for this situation is found to be around three. Hence, the stress at the hotspots is around three times higher than the stresses elsewhere in the component. The hotspots are the critical locations with regards to fatigue for this component.

All components in the pin connection are analyzed in a similar way as in the example. Potential stress hotspots are identified and the stress level at these locations is estimated, based on the nominal stress and a corresponding SCF. The resulting hotspot stress signals form the input for the fatigue damage calculations.

3.5 Fatigue damage

The fatigue damage that is accumulated at the critical locations are the results of main interest. The input for the fatigue damage calculations are the hotspot stress signals of the potential critical locations. It is the last step in the general flow diagram and consists of two sub-steps, as shown in Fig. 3.16.

3.5.1 Palmgren-Miner rule

Various methods are known to calculate fatigue damage. The most widely used method is the Palmgren-Miner rule, which is also recommended by [24]. It is assumed that the stress signal is a combination of stress cycles with different magnitudes. It is also assumed that the damage per stress cycle is constant (Eq. (3.12)) and that the total damage is equal to the sum of the damage of the different stress cycle components, see Eq. (3.13). In this equation, n_i is the number of stress cycles in the stress signal, and N_i is the maximum number of cycles until fatigue failure for the considered stress range magnitude. The expected damage is thus found by calculating the ratio between the expected number cycles, which is derived from the stress signal, and the maximum number of cycles. The maximum number of cycles to fatigue failure is derived from an SN-curve.

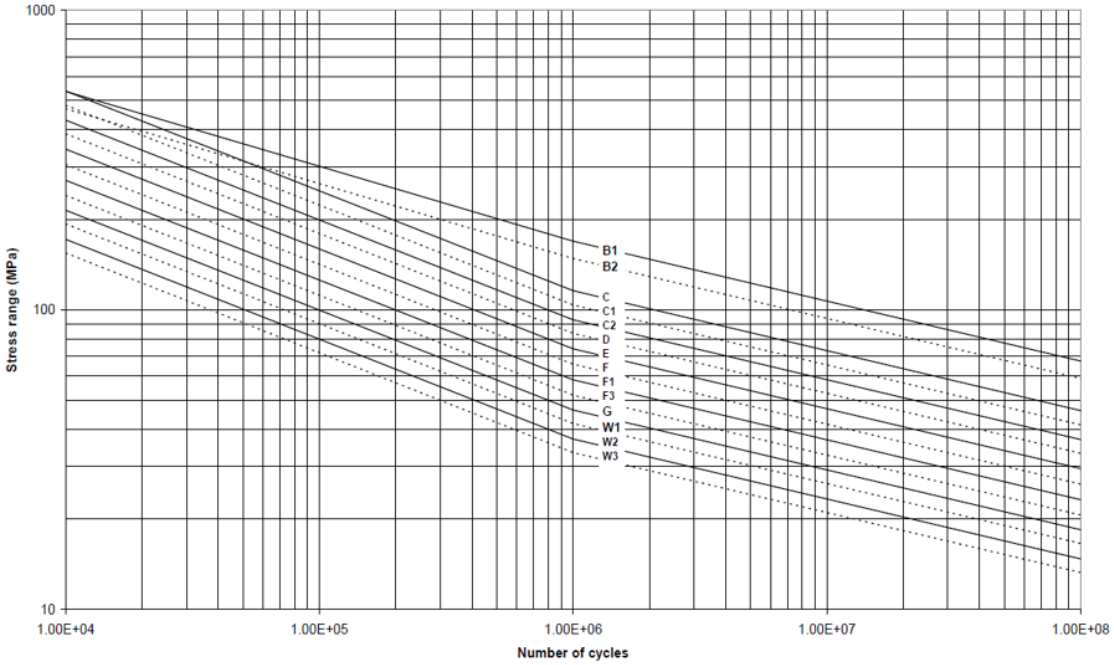

Figure 3.17: SN-curves for the different detail classes

$$D = \frac{1}{N} \tag{3.12}$$

$$D = \sum_i \frac{n_i}{N_i} \tag{3.13}$$

3.5.2 SN-curves

An SN-curve is a graphical representation of the dependence of fatigue life in cycles (N) on the stress range (S). SN-curves are determined experimentally, based on tests. During the tests, the maximum number of cycles to fatigue failure, as a function of stress range magnitude, has been studied for many geometrical arrangements. The design SN-curves are based on the mean-minus-two-standard-deviation curves for relevant experimental data. The SN-curves are thus associated with a 97.7% probability of survival [23]. A general relation between the maximum number of stress ranges and the magnitude of the stress range is shown in Eq. (3.14). In this equation, a is a constant, $\Delta\sigma$ the magnitude of the stress range and m is the fatigue strength parameter, equal to the slope of the SN-curve on loglog-scale. The curves in Fig. 3.17 have two slopes, one for high stress ranges (the fatigue life decreases quickly with an increasing stress range) and one for lower stress cycles. The transition is at one million stress cycles for structures in seawater.

$$N = a(\Delta\sigma)^{-m} \tag{3.14}$$

The SN-curves for steel structures in sea water (with cathodic protection) are derived from [23] and they are shown in Fig. 3.17. The curves represent different detail classes. The appropriate SN-curve should be selected, based on the nature of the fatigue problem, which is described by the following factors:

- The geometrical arrangement of the detail
- The direction of the fluctuating stress relative to the detail
- The method of fabrication and inspection of the detail

Note that the difference between SN-curves is simply constant factor. A lower SN-curve means that a factor is considered to account for expected stress concentrations or uncertainties.

An important assumption is made when using SN-curves for the applications in this research. The experimental data is only available from tests with small specimens. The data is not verified for

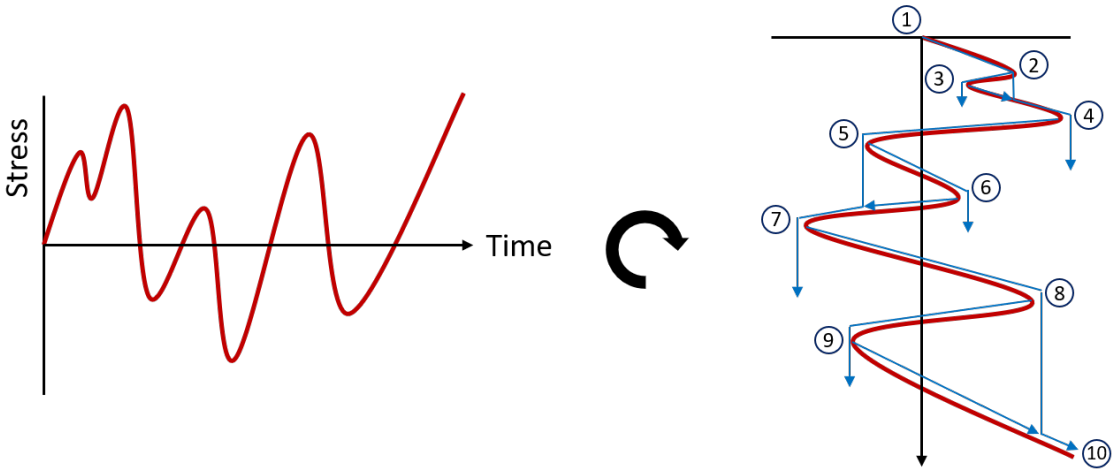

Figure 3.18: Graphical representation of the Rainflow counting method

large configurations. Therefore, possible (favorable or unfavorable) scale effects are not accounted for.

3.5.3 Stress signal components

To find the maximum numbers of cycles to failure (for Eq. (3.13)), the stress components in the signal should be identified. The stress signal is represented by a number of stress cycles with different magnitudes and number of occurrences. Two methods are used for the counting of the stress cycles. The first method uses the Rainflow counting algorithm, to find exact results. The second method approximates the number and magnitude of stress cycles, using the Rayleigh assumption for signals. In the last part of this section, the methods are compared.

3.5.4 Rainflow counting

Several counting algorithms are available, to count the frequency of occurrence and the magnitude of stress ranges in a signal. The most widely used method is the Rainflow counting method [1]. This method uses the similarity of rain that flows downwards from a rooftop with different levels. It is explained in the steps below, based on the example in Fig. 3.18.

1. The stress signal on the left is rotated by ninety degrees, so that the signal forms a similarity with a 'Pagoda roof'.
2. Rain flow starts at the start of the time series and at each 'inside' of a peak or valley
3. The rain keeps flowing downwards until:
   (a) A peak/through is reached that is higher/lower than the point from where it started. An example of this situation is at point 3 in the figure. The flow started at the peak at point 2, but the peak at point 4 is higher.
   (b) It meets a rain flow from a roof above. An example of this situation is at point 6. The rain starts flowing at the peak at point 6, but then it merges with the flow coming from point 5.
   (c) It reaches the end of the time series. This is the case at peak 10.
4. The algorithm finds the magnitude of the stress range by calculating the difference between the starting point and the end point. At the end it counts the number of occurrences for each range.

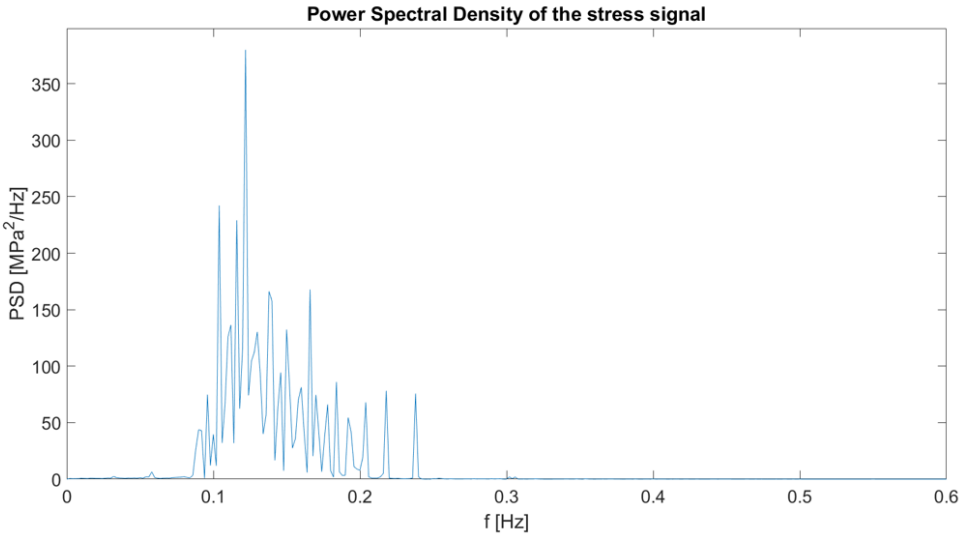

Figure 3.19: Caption

3.5.5 Rayleigh approximation

An alternative for the Rainflow counting method is the Rayleigh approximation. The statistical analysis of the periods between the zero crossings (or between the peaks) of a wave record is closely related to the distribution of energy over the frequency or period spectrum [18]. The Rayleigh approximation makes use of this relation. Also it is assumed that the stress signal is narrow-banded, and that the probability density function the stress cycle magnitude follows a Rayleigh distribution. The validity of this assumption is checked with the irregularity factor (IF), which is addressed later on in this chapter.

The equation for the Rayleigh distribution is shown in Eq. (3.15). It is observed that the only unknown parameter in this equation is the zeroth-order spectral moment. The next sub-section describes how the zeroth-order (and higher order) spectral moments are calculated and how they can be used to approximate the characteristics of the stress signal.

$$p(\Delta\sigma) = \frac{\Delta\sigma}{4m_0} \cdot e^{\frac{\Delta\sigma^2}{8m_0}} \tag{3.15}$$

3.5.6 Spectral moments

Spectral moments are calculated based on the power spectral density (PSD) of a signal. The PSD describes the distribution of power into frequency components composing that signal [21]. From this diagram, the frequency of the most dominant component in terms of energy can be found. The PSD of a signal is obtained using the Fast Fourier Transform (FFT). The FFT converts a signal from the time domain to a representation in the frequency domain. The PSD is then calculated with the expression shown in Eq. (3.16). In this equation F_s is the step size of the time vector and N is the number of datapoints in the stress signal. In Fig. 3.19 an example of a PSD of a stress signal is shown. This signal is the results of a simulation of a sea state with $H_s = 2.39[m]$ and $T_p = 9.0[s]$. The figure shows that the peak period of the spectrum (9.0 [s], equivalent to around 0.1 [Hz]), also has the main contribution to the energy in the stress signal.

$$PSD = \frac{1}{F_s \cdot N}|FFT(S)|^2 \tag{3.16}$$

From a PSD, spectral moments can be calculated which describe some characteristics of a stress signal. The definition of the n^{th} order moment is shown in Eq. (3.17). From this definition it is derived that the zeroth-order spectral moment represents the area under the curve. This is an indication of the total amount of energy that is present in all frequencies. Eq. (3.15) shows that the Rayleigh distribution is fully defined by the zeroth-order spectral moment only. More specifically, the higher the value of the zeroth-order spectral, the more 'stretched' the Rayleigh pdf is, which

means that the probability of high stress ranges increases.

Other useful spectral moments are the second- and fourth-order moment. With these parameters, the mean zero-crossing period (Eq. (3.18)), the number of peaks per second (Eq. (3.19)), and the irregularity factor (IF) can be calculated (Eq. (3.20)) [21]. The mean zero-crossing period is calculated based on the Rayleigh assumption of a narrow-band signal. This is not the actual mean zero-crossing period, but an estimation based on the statistical parameters. The same holds for the expected number of peaks per second. The validity of the Rayleigh assumptions and hence the accuracy of T_z and E_p can be checked with the irregularity factor (IF). With this factor, the number of expected peaks is divided by the expected number of zero-crossings. If this factor tends to one, it means that the assumption of the narrow-band signal is valid, as it confirms the assumption that a zero-crossing is followed by a peak. In contrary, if it takes values smaller than 0.5, it means that the signal is not narrow-band and that the *pdf* of the stress range is expected to follow a different distribution. The irregularity factor of the signals considered in this research are in general around 0.85.

$$m_n = \int_0^\infty f^n \cdot S(f) df \tag{3.17}$$

$$T_z = \sqrt{\frac{m_0}{m_2}} \tag{3.18}$$

$$E_p = \sqrt{\frac{m_4}{m_2}} \tag{3.19}$$

$$IF = \sqrt{\frac{m_2^2}{m_0 m_4}} \tag{3.20}$$

Accumulated fatigue damage can also be calculated with the Rayleigh assumption (refer to Eq. (3.21)). The damage is calculated with Eq. (3.13), but with an approximated value of n_i. It is determined by multiplication of the length of the signal (L), the expected number of peaks per unit time (E_p) and the Rayleigh distribution of the stress ranges, which is calculated with m_0.

$$D = \sum_i \frac{n_i}{N_i} = \sum_i \frac{1}{N_i} \cdot n_{cyc} \cdot p(\Delta\sigma_i) = \sum_i \frac{1}{N_i} \cdot L \cdot E_p \cdot p(\Delta\sigma_i) \tag{3.21}$$

3.5.7 Comparison of methods

With the Rainflow counting method the magnitudes and number of occurrences of the stress ranges are determined exactly. Hence, the actual stress signal is used for the fatigue damage calculation, without any approximations. This can be both an advantage and a disadvantage. The stress signals in this research have a relatively short duration of 500 [s], representing a sea sate of 3 [h]. There is thus uncertainty about the statistical parameters of the signal. An inaccurate representation of the sea state, for example because there are multiple extreme values in the stress signal, results in accurate damages as well. This is shown in the next paragraph.

The stress cycles of a random stress signal have been counted/estimated with both the Rainflow counting method and the Rayleigh approximation. Fig. 3.20 shows in blue the actual number of occurrences per stress range for the Rainflow counting. It is observed that the Rayleigh approximation (in red) is relatively accurate, with some exceptions. This figure is compared with the corresponding damage per stress range, shown in Fig. 3.21. It is observed that the highest stress ranges found with Rainflow counting, account for almost all the damage. Consequently, the damage calculation with this method is very sensitive to high stress ranges. Statistical extremes therefore have a large impact on the damage that is found. The effect is increased even more, because the 500 [s] stress signal is extrapolated to a full year. This is done with the factor shown in Eq. (3.22).

The distribution of stress ranges according to the Rayleigh approximation is based on the total energy in the stress signal. The total energy is a more stable measure for the distribution of stress ranges, because it is less dependent on extreme values. Hence, the damage that is calculated with this method is believed to be more accurate and more consistent than the Rainflow counting method. The Rayleigh approximation is therefore used to calculate the fatigue damage from the stress signals.

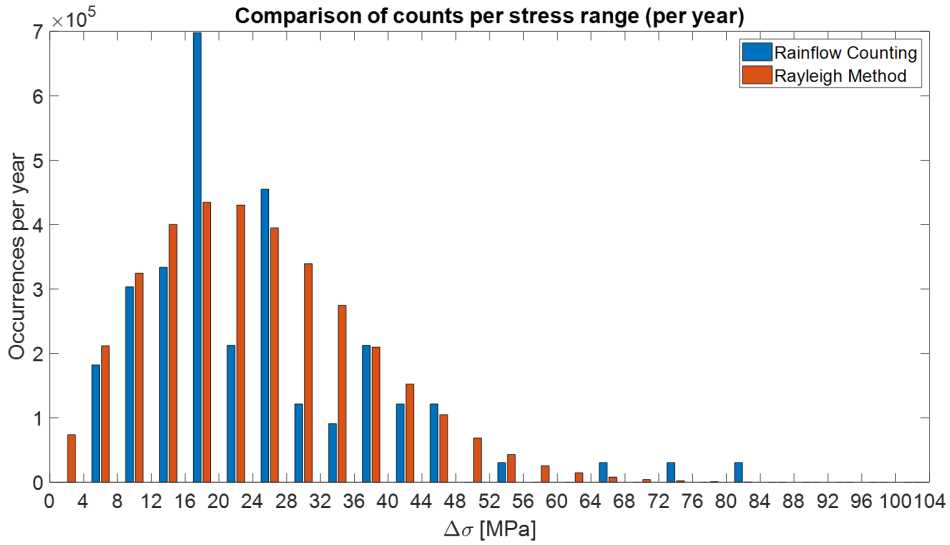

Figure 3.20: Number of occurrences per year for different the stress ranges

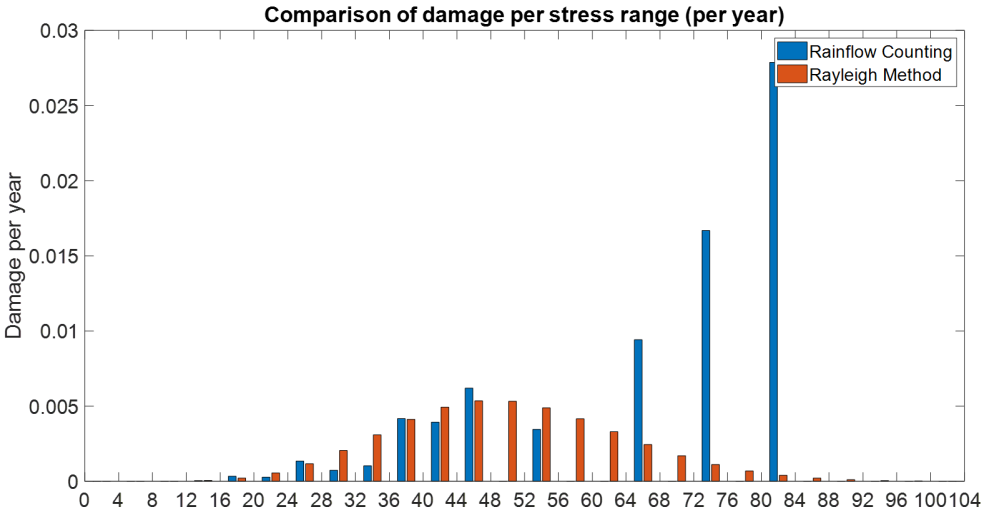

Figure 3.21: Yearly damage per stress range

$$factor = \frac{365.25 \frac{days}{year} \cdot 24 \frac{h}{day} \cdot 3600 \frac{s}{h}}{500s} \tag{3.22}$$

3.5.8 Damage calculation

The total damage per year is calculated as follows. Stress signals are calculated based on a 500 [s] representation of a single sea state. The damage for this signal is calculated and extrapolated to a full year, by multiplying with the factor in Eq. (3.22) and the probability of the sea state. The total damage is found by summing the yearly damage results of the individual sea states, see Eq. (3.23). This results in a yearly accumulated damage, with which either the expected fatigue lifetime (Eq. (3.24)) or the damage during the design lifetime of the structure can be calculated.

$$D_{yearly} = \sum_{i=1}^{N_{seastates}} D_i \cdot p_i \tag{3.23}$$

$$Lifetime = \frac{1}{D_{yearly}} \tag{3.24}$$

Chapter 4

Hand calculated stresses

The calculation of the stresses in the pin connection is the main topic of this thesis. In this chapter, it is explained how stresses are estimated, based on the geometry of the structure and the internal forces in the members, obtained from USFOS.

The pin connections are considered as the critical parts in the design of the TetraSpar, with regards to fatigue. Due to complex geometries and details, there are stress concentration zones in which the stress is higher than the nominal stress. The potential locations where stress concentrations might be critical are identified in this section. It is explained which forces are transferred through the detail, and how the nominal stress and hotspot stress in the components of the connection are calculated. An estimation of the SCF is made and the appropriate SN-curve is selected, both by comparing the geometry to standard details as documented in [23] and [15]. Not all potential critical spots can be assessed properly based on hand calculations. In some spots the load paths are unknown, or the geometry is too complex to compare it with a simplified situation. Stresses, SCFs and SN-curves are estimated in these cases, but they are to be validated with finite element analysis.

4.1 Considered connection

There are a total of eighteen pin connections in the design of the TetraSpar floater, consisting of four unique geometries, as shown in Fig. 4.1. They are not analyzed individually. Instead, only the connection type that is expected to be the most critical one is assessed.

In every member, the force that has the highest contribution to the total load on the pin connection, is determined. For each connection type, the main force is identified, and the standard deviation of its time signal is determined. Recall from Chapter 3, that the standard deviation of a stress signal is the governing factor for fatigue damage in a component. Hence, if the standard deviations of the main force signals are compared, it can be determined which pin connection is expected to be the most critical one. The results of the comparison are shown in Table 4.1. Note that the ratios between the standard deviations are shown. The actual values of the standard deviations depend on the environmental conditions. Based on the presented results, the connections between the lateral and radial member are selected for the fatigue strength assessment. These connections are shown in the lower right panel in Fig. 4.1.

The loads on these connections are the internal forces in the lateral member. They are in five degrees of freedom, because the moment in the rotation plane of the pin connection is assumed to be zero. The variation of the five internal force components is plotted in Fig. 4.2. From the figure it is concluded that the load mechanism on the connection is governed by the moment around the transverse axis. The influence of the other load components is much smaller.

Table 4.1: The different type of connections in the structure

Connection	Governing force signal	Relative standard deviation
Diagonal – Center column	Axial force (diagonal)	0.42
Radial – Center column	Axial force (radial)	0.46
Lateral – Radial	Bending moment (lateral)	1.00
Diagonal - Radial	Axial force (diagonal)	0.42

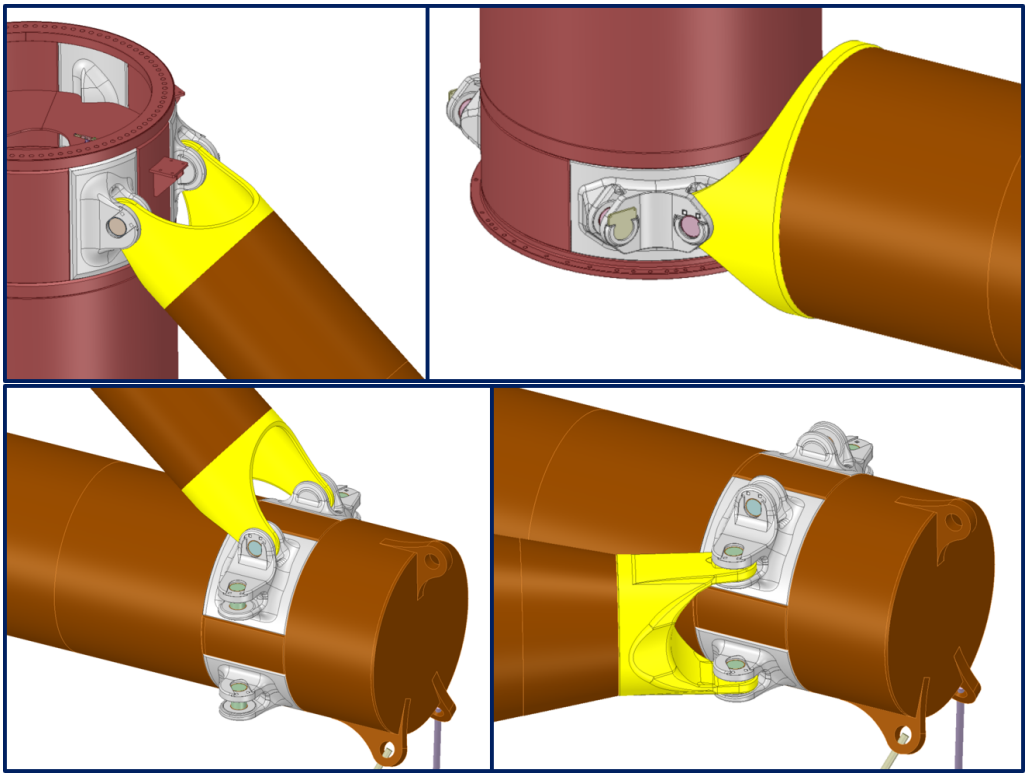

Figure 4.1: The four connection types in the design

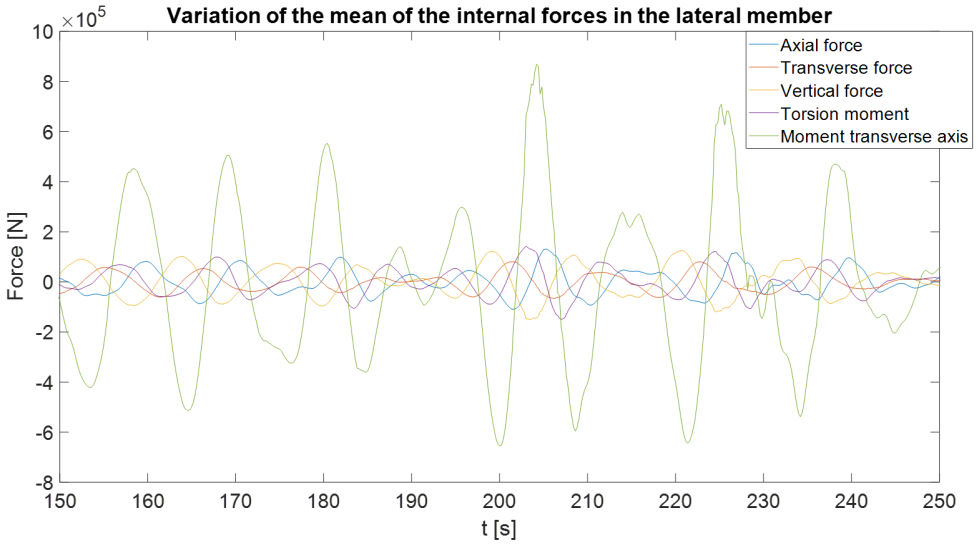

Figure 4.2: Sample of the time signal of the variation of the internal forces in the lateral member

4.2 Method

The method that is used to find the hotspot stress signal and the appropriate SN-curve is shown in Fig. 4.3. The internal forces in the tubular members of the floater are derived from the USFOS simulations. Simplified stress distributions in the member cross-sections are obtained based on equilibrium with the member end loads. Combined with empirical SCFs (obtained from literature), these distributions generate an estimate of the hotspot stress time series. Together with an appropriate SN-curve for the considered detail, this forms the output of the stress calculations and the input for the fatigue damage calculations. In the next sections, the individual components of the pin connection are analyzed to find potential stress hotspots. It is discussed how the stresses for the hotspots are calculated and which SN-curve is recommended. Refer to Fig. 4.4 for the names of the components in the pin connection.

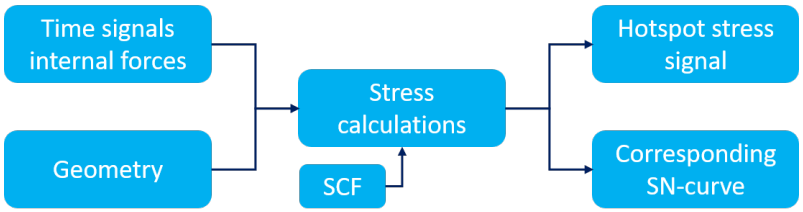

Figure 4.3: Flow diagram that shows the steps for the calculation of the stresses in this chapter

4.3 Ear part of the connection

The end of the lateral member is a casting where the ears are integrated in the shell of the tubular member (yellow part in Fig. 4.4). Forces are transferred from the lateral member via the casting to the pin connection. Three potential critical locations are identified in the yellow casting component. They are discussed in the next sub-sections.

4.3.1 Weld between casting and element

The first location is the weld that connects the casting with the regular part of the lateral member (brown part in Fig. 4.5). It is expected that a large fraction of the loads in the lateral member is transferred through this weld, to the ear of the casting. For the stress calculation, it is assumed that all the forces are transferred through the length of the weld, equal to the width of the ear, see Fig. 4.5. SCFs are calculated to translate the nominal stress in the full circumference, to stresses in the circumference covered by the indicated part of the weld only (and the same weld

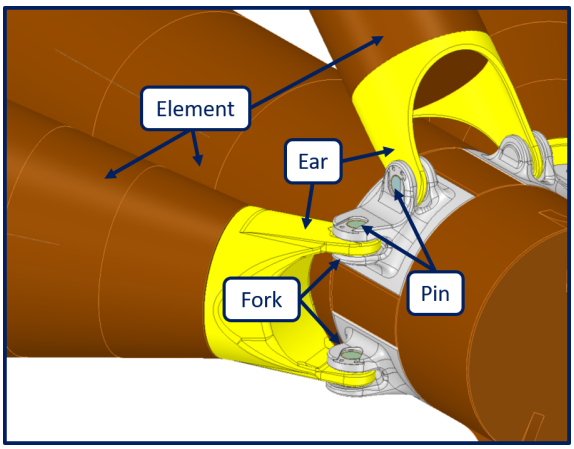

Figure 4.4: Terminology for the components in the pin connections

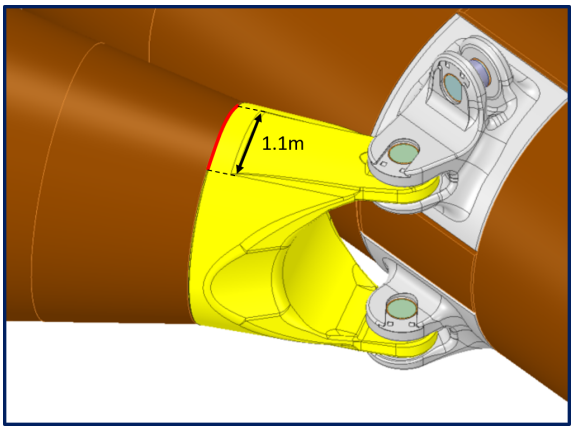

Figure 4.5: Weld between the lateral member and the casting

on the opposite site). The SCFs for axial stress and bending stress are not equal, as shown in the derivations below (refer to Eq. (4.1) to Eq. (4.5)).

The SCF for bending stress is equal to the ratio between the stress in the indicated part of the weld and the nominal stress in the lateral member, which is distributed over the full circumference.

$$SCF_b = \frac{\sigma_{weld}}{\sigma_{nom}} = \frac{M/W_{weld}}{M/W_{nom}} = \frac{W_{nom}}{W_{weld}} \tag{4.1}$$

Using the approximation for shells with a small wall thickness, the section moduli of the full cross-section and the part of the welds only are respectively

$$W_{nom} = \pi R^2 t \quad W_{weld} = 2(\alpha \cdot 2\pi Rt \cdot R) = 4\pi R^2 t \cdot \alpha \tag{4.2}$$

$$\alpha = \frac{A_{weld}}{A_{tot}} = \frac{t \cdot L_{weld}}{t \cdot L_{tot}} = \frac{1.1}{2\pi R} = \frac{1.1}{6.9} \tag{4.3}$$

Substituting these expressions in Eq. (4.1), yields

$$SCF_b = \frac{W_{nom}}{W_{weld}} = \frac{\pi R^2 t}{4\pi R^2 t \cdot \alpha} = \frac{1}{4\alpha} = 1.58 \tag{4.4}$$

The axial stress concentration depends on the ratio of the cross-sectional areas. The SCF is calculated with Eq. (4.5)

$$SCF_a = \frac{\sigma_{weld}}{\sigma_{nom}} = \frac{F/A_{weld}}{F/A_{tot}} = \frac{A_{tot}}{A_{weld}} = \frac{2\pi Rt}{2(2\pi Rt \cdot \alpha)} = \frac{1}{2\alpha} = 3.13 \tag{4.5}$$

At the location of the weld, there is also a difference in plate thickness between the casting and the shell of the lateral element. An additional SCF is therefore introduced, which is calculated with Eq. (4.6). This equation is documented in [23] for butt welds between shells of different thicknesses. In the equation δ_m is the maximum misalignment, δ_t the misalignment due to the change in plate thickness and δ_0 the misalignment inherent in the SN-data, which is equal to $0.1t$. For the weld shown in Fig. 4.5, this results in an SCF of approximately 1.3. The total stress in the butt weld is finally calculated with Eq. (4.7). The recommended SN-curve for a transversely loaded butt weld is the D-curve, according to [23].

$$SCF_t = 1 + \frac{6(\delta_m + \delta_t - \delta_0)}{t(1 + \frac{T^{1.5}}{t^{1.5}})} \tag{4.6}$$

$$\sigma = SCF_t \cdot \left(SCF_a \cdot \frac{F}{A_{nom}} + SCF_b \cdot \frac{M}{W_{nom}} \right) \tag{4.7}$$

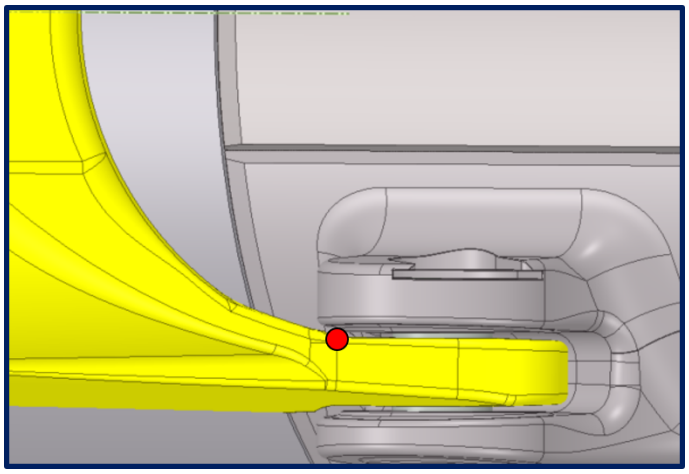

Figure 4.6: Potential critical point at the thickness transition of the lower ear

4.3.2 Minimum cross-section

The second potential critical location in the ear part is shown in Fig. 4.6. The forces that are transferred through the ear are determined by solving the equilibrium equations on cross-section A-A (Fig. 4.7). The reaction forces at this cross-section are the loads that are transferred to the ears. There are three relevant loads acting on the left side of the cross section. The first load is the lateral load, which is reacted by two equal forces with half the magnitude. The second load is a moment. It is reacted by two forces with the same magnitude but pointing in opposite directions. The magnitude is equal to the moment divided by the distance between the forces. The third load is the axial force. Equilibrium on the cross-section is maintained with two reaction forces in the opposite direction. Reaction forces resulting from the axial load and the moment can be summed, because they act in the same direction. This results in equivalent axial forces. The expression for the calculation of the equivalent axial forces is shown in Eq. (4.8).

$$F_{ax,eq} = \frac{F_{ax}}{2} \pm \frac{M}{r} \tag{4.8}$$

Refer to Fig. 4.8 for a schematic representation of the ear, with the potential critical spot indicated with a red dot. Note that the ear shown in the figure is the lower ear of the casting, which is under tensile stress. The upper ear is under compression stress and it is therefore not considered as critical element. The different directions of the forces on the ears is caused by the moment, which is much larger than the axial force. Equilibrium of the ear is maintained by the reaction forces of the fork and the pin. It is assumed that the reaction force from the fork on the ear is a triangular distributed load. This is explained by the fact that there is a small tolerance between ear and the fork. The ear is pushed against the upper flange of the fork, by the static buoyancy force. This load will force the lateral member to bend slightly, so the ear will slightly rotate as well. It is therefore expected that the reaction force is most accurately represented by a triangular distributed load.

The stress in the hotspot is a combination of axial stress and bending stress. It is calculated with Eq. (4.9). In this equation F_{res} is the resultant force of the triangular distributed load, and r is the distance between the resultant force and the critical spot. There is a stress concentration at the critical spot, because the thickness of the ear increases at this point. Diagrams for SCF values for such details are found in [15]. The SCF depends on the difference in thickness and the radius of the fillet. The full diagram can be found in Appendix A. Both parameters (thickness difference and fillet radius) are difficult to quantify for this situation, as can be observed in Fig. 4.6. The values are therefore estimated, resulting in an SCF of approximately 1.50. The recommended SN-curve is the C-curve, which applies to plain cast steel.

$$\sigma_{ear} = SCF \cdot (\sigma_{axial} + \sigma_{bending}) = SCF \cdot \left(\frac{F_{ax,eq}}{A_{ear}} + \frac{F_{res} \cdot r}{W_{ear}} \right) \tag{4.9}$$

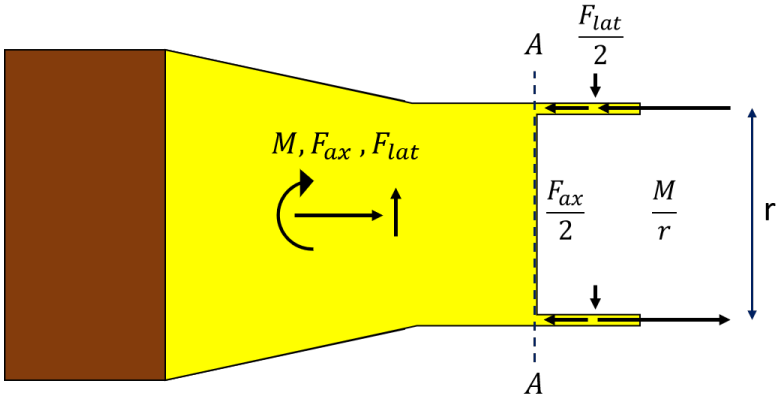

Figure 4.7: The equilibrium on cross-section A-A is used to derive the forces in the ear parts

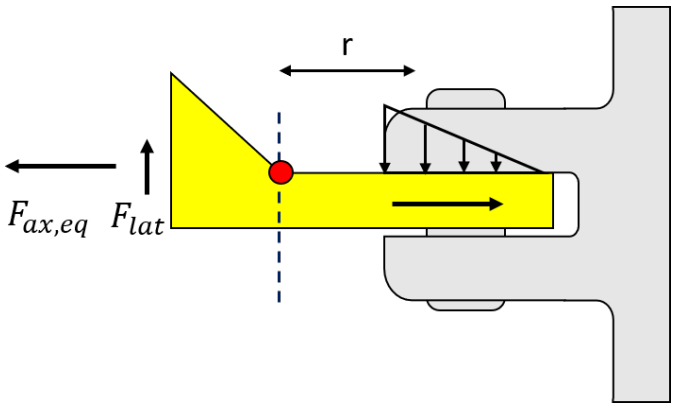

Figure 4.8: Forces on the lower ear with the critical location indicated in red

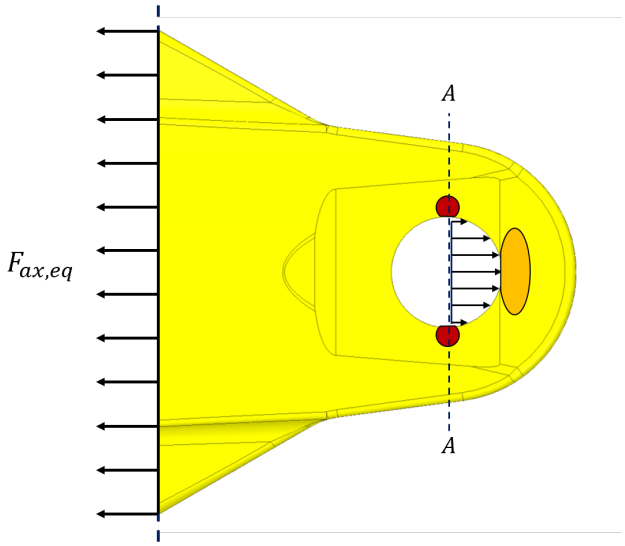

Figure 4.9: The critical locations in red result from a tensile stress

4.3.3 Hole in the ear

The third potential critical detail in the ear component are the spots next to the hole in the ear. At the hole, loads from the lateral member are transferred to the pin and the fork of the connection.

A top view of the free body diagram of the ear for this situation is shown in Fig. 4.9. The equivalent axial force is the only relevant load (refer to Eq. (4.8) and Fig. 4.7). It results in a reaction force from the pin on the inside of the hole. From literature [7] it is known that a load transfer through such a connection induces stress concentration zones at the locations indicated with orange and red in Fig. 4.9 . In [19], this type of connection is called a 'lug connection' and stress concentration zones are discussed in detail. For a lug connection, which is equivalent to the ear-pin connection, the SCF in the red zones can be high, as can be observed in the diagram shown in Appendix A. The figure shows a diagram from [15] of the SCF as a function of the dimensions of the ear. The SCF is found to be equal to 3.00 and the proper SN-curve is again the C-curve. The stress is calculated by multiplication of the SCF and the nominal stress, as shown in **??**. The nominal stress is equal to the equivalent axial force divided by the cross-sectional area at the critical location (A-A in Fig. 4.9).

It should be noted that the theory explained above only holds for ears under a tensile load. If a part of the load cycle, or the full load cycle, results in compression loads in the ear then for the compression part of the cycle the load is reacted on the other side of the eye. Hence, there is no load transferred in the critical cross-section. The fatigue loading reduces accordingly. The locations next to the hole are therefore only critical for the lower ear. The upper ear is in permanent compression, so it is not considered as a critical component.

$$\sigma = SCF \cdot \sigma_{nom} = SCF \cdot \frac{F_{ax,eq}}{A_{a-a}} \tag{4.10}$$

4.4 Pin

The second component of the connection is the pin. It forms the connecting element between the ear and the fork part. The relevant load on the pin is the equivalent axial force only, which results in a pure shear stress. The shear stress is calculated with Eq. (4.11).

In [23] there is not much information about fatigue damage resulting from a shear stress mechanism. However, it does report about a bolt connection that is is transversely loaded. This is essentially the same situation. Fig. 4.10 shows the connection. No specific SN-curve is recommended. Instead a similar equation as for a part of an SN-curve is given for this situation, see

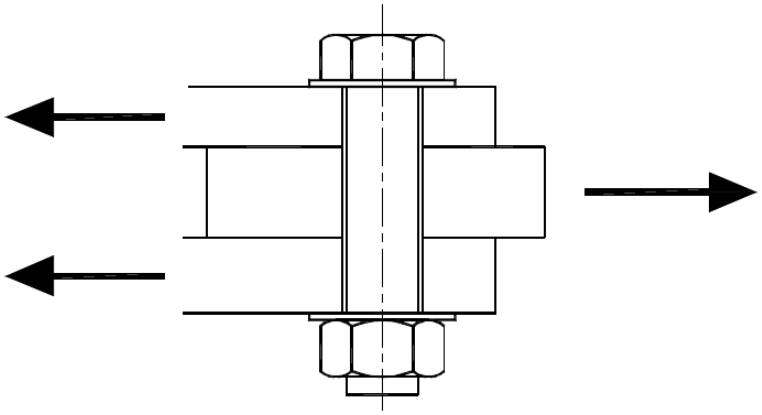

Figure 4.10: Shear load mechanism documented in [23]

Eq. (4.12). Essentially, this is an SN-curve with a single slope, instead of a double slope. The only restraint that is given, is that the thread of the thread of the bolt is not in the shear plane, but this is not applicable to the pin. An SCF is not known for this specific situation, but it is expected that it is equal to one, as there are no notches or other irregularities in the cross-section of the pin.

$$\tau = \frac{F_{ax,eq}/2}{A_{pin}} \tag{4.11}$$

$$log(N) = 16.301 - 5.0 \cdot log(\Delta\tau) \tag{4.12}$$

4.5 Fork

The fork is connected to the pin and it transfers loads to the radial element. There are two potential critical locations in the fork. They are discussed in the next sub-sections.

4.5.1 Hole in the fork

There are two important load mechanisms for this location. The first one is the tensile force exerted by the pin, coming from the ear part. The ear and the fork make an angle with each other, so the equivalent axial force is applied under an angle as well. The critical cross-section is perpendicular to the force, as shown in Fig. 4.11. So, a different critical cross-section is found than for the ear component. Also, the equivalent axial force is distributed over two flanges, so the force is divided by two. The resulting stress mechanism however, is the same, where stress concentration zones occur next to the hole. The SCF for these zones is determined with the diagram that can be found in Appendix A. An SCF of 3.00 is obtained. The material of the fork is cast steel, so the appropriate SN-curve is the C-curve.

The second load transfer mechanism results from the lateral force (right panel in Fig. 4.11). This force is exerted by the ear, which is pushed against the upper flange of the fork. Recall that this load is modelled as a triangular load. The result of the distributed load is a bending stress in the flange of the fork. The load increases from zero at the tip of the ear to a maximum value at the base of the ear. Hence, at the critical cross-section (A-A in Fig. 4.11), there is also a bending stress, next to the axial stress (resulting form the equivalent axial force). The bending stress is calculated with the maximum moment, which is equal to the resultant of the triangular distributed load, multiplied with the distance r between the critical spot and the resultant force. There is compression in the upper side of the flange, and tension in the lower side of the flange. Consequently, the critical part in cross-section A-A is next to the hole, at the lower side of the upper flange, highlighted in red in the right panel in Fig. 4.11. The stress is calculated by summing the axial stress and the bending stress, Eq. (4.13).

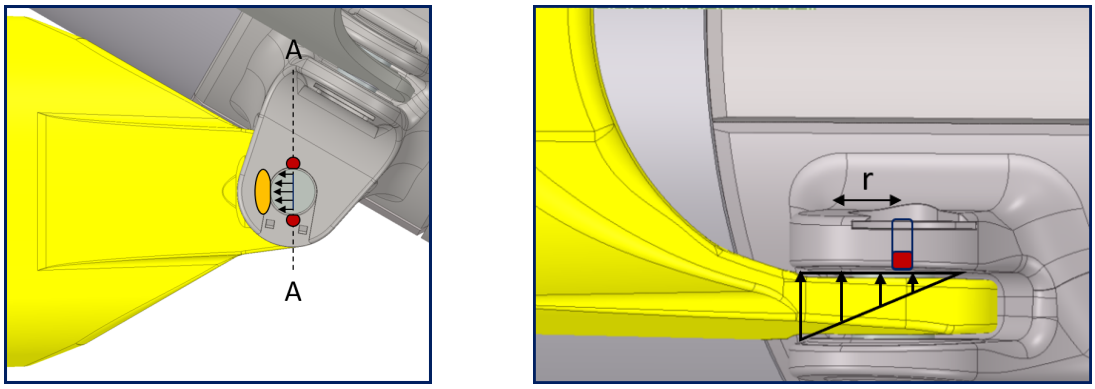

Figure 4.11: Top and side view of the locations next to the hole in the fork

$$\sigma = SCF \cdot \sigma_{ax} + \sigma_{bend} = SCF \cdot \left(\frac{F_{ax,eq}}{A_{a-a}} \right) + \frac{F_{res} \cdot r}{W_{a-a}} \tag{4.13}$$

4.5.2 Base of the fork

The lateral load applied on the upper flange also results in bending moments in the direction parallel to the fork. The triangular distributed load, shown in 2D in Fig. 4.11, is represented by the resultant force shown in Fig. 4.12. The bending stress that results from this force is maximum at the base of the fork, at the maximum distance r from the resultant load. Additionally, this spot experiences a part of the equivalent axial load, namely the component that is perpendicular to the base. The perpendicular component is found by decomposing the equivalent axial load in a component parallel and perpendicular to the base of the fork, as shown in Fig. 4.13. The perpendicular component results in an axial stress. This is added to the normal stress resulting from the bending moment at the base and the total stress is obtained. Eq. (4.14) shows the expression for the calculation of the stress. The SCF in this equation results the change of thickness of the cast fork, similar to the ear part discussed in Section 4.3. The intensity of the stress concentration depends on the ratio between the radius of the fillet at the critical spot and the thickness of the flange. An estimation of the SCF is derived from the diagram shown in Appendix A. Based on the dimensions of the flange of the fork, an SCF of 1.65 is estimated. The recommended SN-curve for cast steel is the C-curve.

$$\sigma_{base} = SCF \cdot (\sigma_{axial} + \sigma_{bend}) = SCF \cdot \left(\frac{F_{perp}/2}{A_{base}} + \frac{F_{res} \cdot r}{W_{base}} \right) \tag{4.14}$$

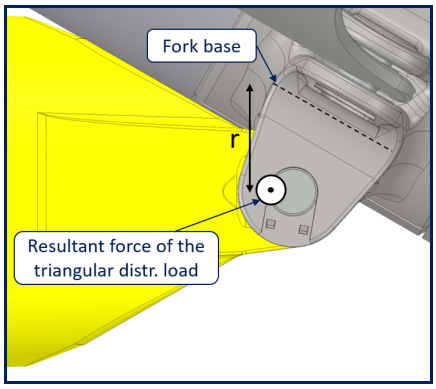

Figure 4.12: Resultant of the distributed load and the arm to the critical location

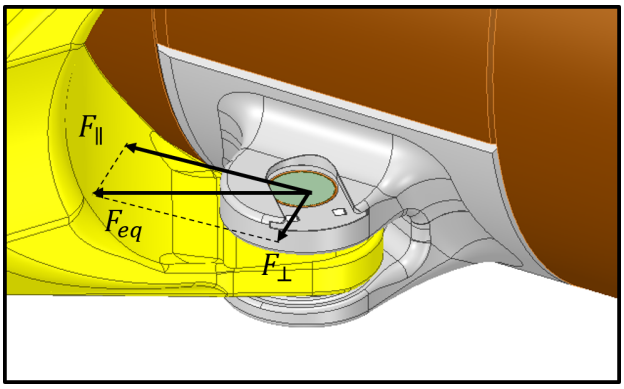

Figure 4.13: The equivalent axial force is decomposed in perpendicular and parallel component

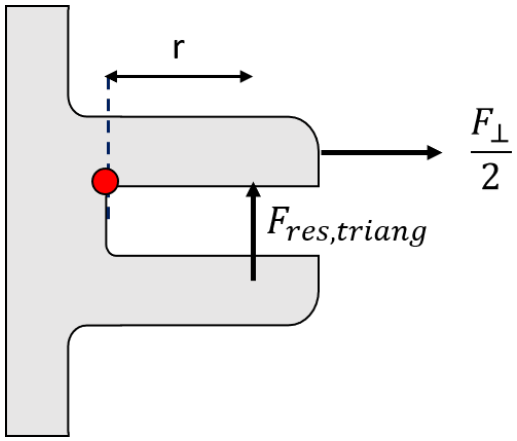

Figure 4.14: Schematic representation of the critical spot at the base of the fork

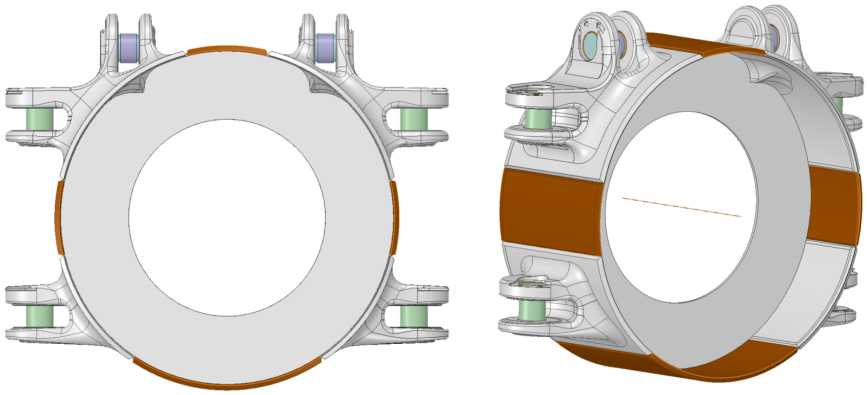

Figure 4.15: Ring stiffener at the inside of the radial member

4.6 Casting - radial member connection

The last step in the load path is the force transfer from the casting to the circular shell element, the radial member. The casting is welded in a cut-out in a circular ring stiffened shell. Also, at the inside of the circular shell element, below the middle of the casting, a ring stiffener is welded to support the casting and prevent the element from deforming. Fig. 4.15 shows the ring stiffener at the connection. The stiffener is welded with a full penetration weld in the complete circumference of the element.

The load on the casting is applied under an angle (equal to the angle between the lateral and radial member). This load is the equivalent axial force that is used in the other parts of the connection as well. It is convenient to decompose it in two components: one perpendicular and one parallel to the shell of the radial. In this way, the load transfer can be analyzed, which is done in the next sub-sections. The load transfer of the parallel component is discussed first and thereafter the transfer of the perpendicular component. Refer to Fig. 4.16 for the decomposed equivalent axial force, and the resulting reaction forces.

4.6.1 Perpendicular component

The ring stiffener from Fig. 4.15 is right under the point of application of the load, as schematically shown in Fig. 4.17. As load always follows the stiffest load path, it is assumed that the load coming from the perpendicular force is transferred to the ring stiffener only. The stiffness of the ring stiffener is namely much higher than the stiffness of the shell around the casting. The resulting stress in the weld between the ring and the casting is calculated using Eq. (4.15). The area of the weld is found by multiplying the thickness of the ring stiffener with the length of the weld. The

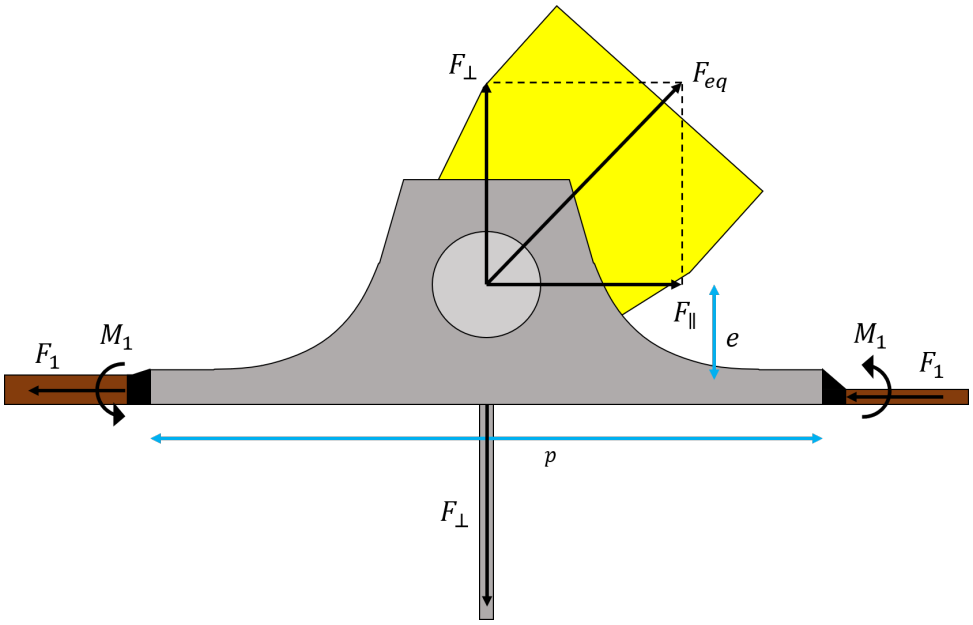

Figure 4.16: Free body diagram of the casting that is welded in the radial member

length that is assumed to transfer the full load is the part of the weld that is equal to the width of the fork, as shown in Fig. 4.18. This load mechanism can be compared to the situation shown in Fig. 4.19, which is derived from [23]. The critical point of the weld is at the weld toe. The recommended SN-curve is the F-curve. No SCF is expected for this situation.

$$\sigma = \frac{F_\perp}{A_{ring}} \quad where \quad A_{ring} = t_{ring} \cdot L_{weld} \tag{4.15}$$

4.6.2 Parallel component

The parallel component of the applied force results in a more complex load mechanism. Because of the eccentricity (e in Fig. 4.16) there is not only a reaction force on the casting, but a local reaction moment as well. It has been tried to simplify the load transfer mechanism to a model that can be solved with hand calculations. However, this model results in nominal stresses in the welds, that are around ten times higher than the yield strength. Hence, it is concluded that this model is too conservative. Although it is not used for the fatigue calculations, a description of the model can be found in Appendix B.

A simpler model is therefore developed. Instead of using the loads exerted *on* the radial, this model uses the reaction force *in* the radial. So, this approach is based on the assumption that the internal forces in the radial member are in equilibrium with the forces on the member. The model is used to approximate the stresses in the welds between the casting and the radial member. This approach is described below.

- It is assumed that the axial force in the radial member is distributed over the welds on the castings only (highlighted with red lines in Fig. 4.20). The stresses are calculated by dividing the axial force by the cross-sectional area of the welds, Eq. (4.16).
- It is assumed that the moment in the radial members is also resisted by the welds on the castings only. The stresses are calculated by dividing the moment by the section modulus of the area of the welds, Eq. (4.16).

To calculate the stress in the welds, the same approach as for the first hotspot (Section 4.3) is used. The stress in the welds is calculated with Eq. (4.16). In this equation, the nominal (axial and bending) stresses in the radial member are multiplied with an SCF for the axial and bending stress respectively. An additional SCF is introduced because there is a difference in wall thickness between the casting and the shell of the radial member. The SCF for axial stress is derived in

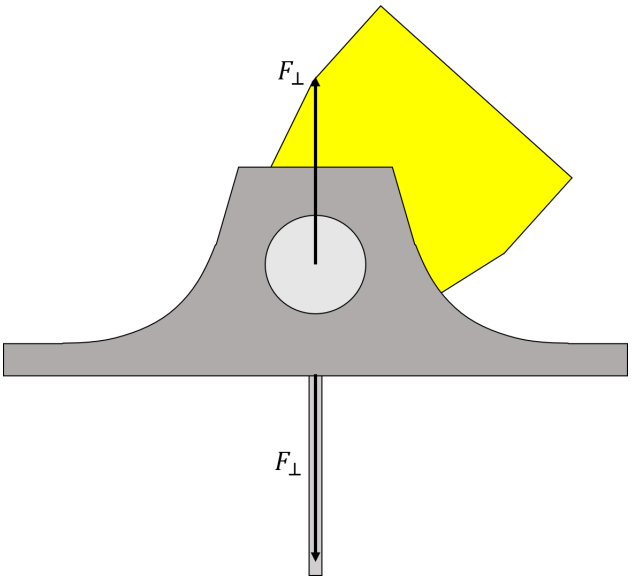

Figure 4.17: Top view of the casting showing the force transfer of the perpendicular force

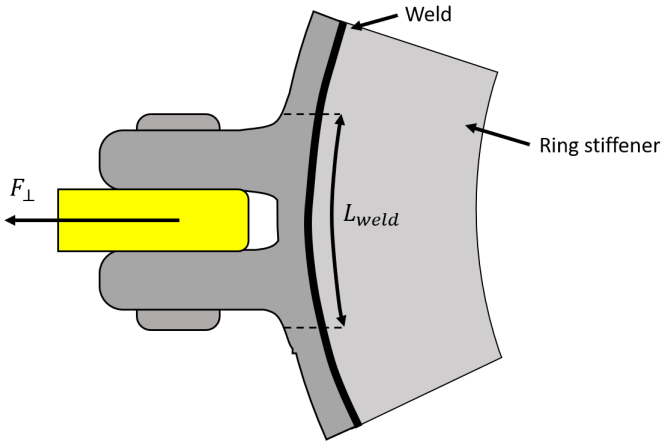

Figure 4.18: The perpendicular of the force is assumed to be transferred through only a part of the weld

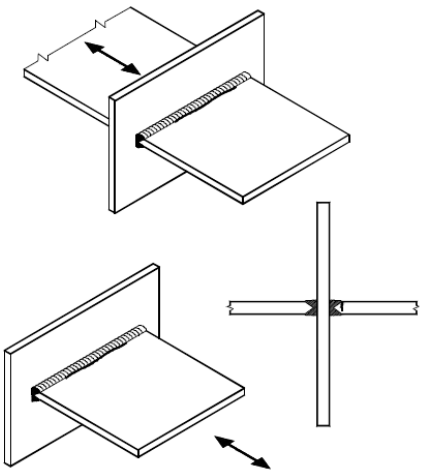

Figure 4.19: The force transfer to the ring stiffener is similar to this situation [23]

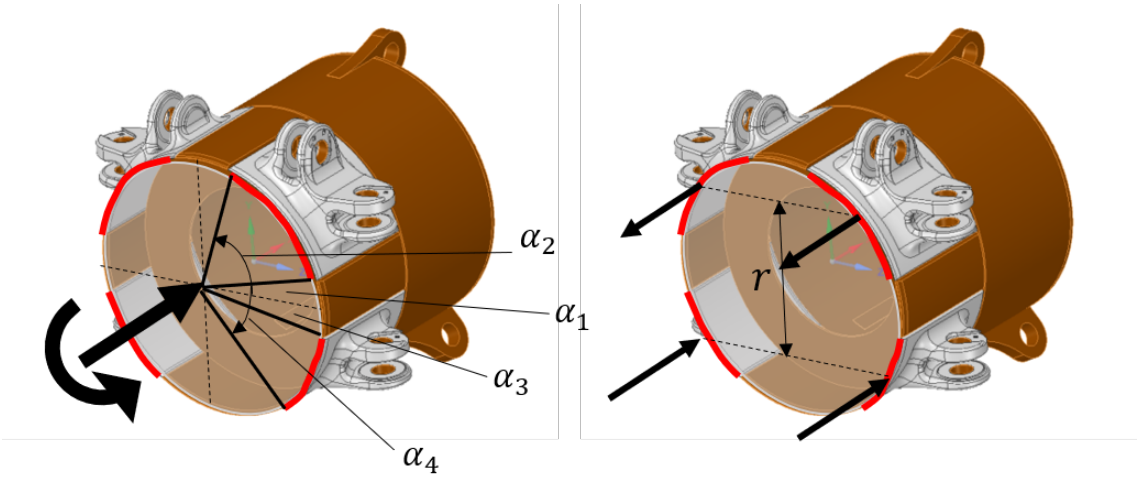

Figure 4.20: Cross-section at the critical location of the welds. The welds are indicated with red lines.

Eq. (4.17). It is defined as the ratio between the hotspot stress (in the weld) and the nominal stress. Simplifying this expression yields the ratio between total circumference of the radial member and the cumulative length of the welds. The result is an SCF for axial stress of 1.70.

$$\sigma_{weld} = SCF_t \cdot (SCF_a \cdot \sigma_{a,nom} + SCF_b \cdot \sigma_{b,nom}) \tag{4.16}$$

$$SCF_a = \frac{\sigma_{a,weld}}{\sigma_{a,nom}} = \frac{F/A_{welds}}{F/A_{total}} = \frac{t \cdot L_{total}}{t \cdot L_{welds}} = \frac{2\pi R}{2R(\alpha_2 - \alpha_1 + \alpha_4 - \alpha_3)} = \frac{\pi}{\alpha_2 - \alpha_1 + \alpha_4 - \alpha_3} = 1.70 \tag{4.17}$$

The SCF for bending stress is defined as the ratio between the maximum bending stress in the welds and the maximum nominal bending stress (Eq. (4.18)). Simplifying this expression yields the ratio between the section moduli of the cross-section of the radial member and the welds only.

$$SCF_b = \frac{\sigma_{b,weld}}{\sigma_{b,nom}} = \frac{M/W_{weld}}{M/W_{tot}} = \frac{W_{tot}}{W_{weld}} = \frac{\pi R^2 t}{I_{weld}/y_{max}} \tag{4.18}$$

The section modulus of the welds is, by definition, equal to the second moment of area divided by the maximum distance from the neutral axis. The second moment of area is calculated with Eq. (4.19). The vertical shift of the neutral axis (because of the non-symmetrical cross-section) is not considered here.

$$I_{weld} = 2\left[\int_{\alpha_1}^{\alpha_2} y^2 dA + \int_{\alpha_3}^{\alpha_4} y^2 dA\right] \tag{4.19}$$

In a cylindrical coordinate system, the integral is expressed as shown in Eq. (4.20).

$$\int_{\alpha_1}^{\alpha_2} y^2 dA = \int_{\alpha_1}^{\alpha_2} R^3 t sin^2(\alpha) d\alpha = \frac{R^3 t}{2}\left[\alpha_2 - \frac{1}{2}sin(2\alpha_2) - \alpha_1 + \frac{1}{2}sin(2\alpha_1)\right] \tag{4.20}$$

This expression is also calculated for α_3 and α_4 and both are substituted in Eq. (4.19). Eq. (4.19) is substituted in Eq. (4.21) and the maximum distance is simply determined by multiplying the radius with the sine of a2. The SCF is finally determined by substitution of Eq. (4.21) in Eq. (4.18). The result is an SCF of 1.95, as shown in Eq. (4.22).

$$W_{weld} = \frac{I_{welds}}{y_{max}} = \frac{R^3 t \left[\alpha_2 - \frac{1}{2}sin(2\alpha_2) - \alpha_1 + \frac{1}{2}sin(2\alpha_1) + \alpha_4 - \frac{1}{2}sin(2\alpha_4) - \alpha_3 + \frac{1}{2}sin(2\alpha_3)\right]}{R \cdot sin(\alpha_2)} \tag{4.21}$$

$$SCF_b = \frac{\pi \cdot sin(\alpha_2)}{\alpha_2 - \frac{1}{2}sin(2\alpha_2) - \alpha_1 + \frac{1}{2}sin(2\alpha_1) + \alpha_4 - \frac{1}{2}sin(2\alpha_4) - \alpha_3 + \frac{1}{2}sin(2\alpha_3)} = 1.95 \tag{4.22}$$

Note that only the stresses in the welds shown in Fig. 4.20 are calculated with these equations. The welds on the opposite side of the casting do not experience significant loads, because the end of the radial member is not restrained. The recommended SN-curve for this detail is the D-curve [23].

4.7 Summary

In this chapter, the complex geometry of the pin connection is decomposed in its basic parts. The load and stress mechanisms for the components are less complex, so nominal stress levels could be estimated. Stress concentration factors are found in literature by comparing the stress mechanisms in the components to more standard situations for which SCFs are known. The appropriate SN-curves are determined in a similar way, by comparing the components to basic details that are documented in [23]. The results of this chapter are summarized in Table 4.2. It is concluded that stress levels could be estimated with hand calculations for all locations. However, it is expected that for the stress calculation for the last location (the weld between the casting and the radial member) the model is too much simplified. Hence, this specific location is analyzed in more detail in the next chapter, using finite element software.

Table 4.2: Summary of the results for the potential critical locations

Geometry	Driving force	SCF (geometry)	SCF (Δthickness)	SN-curve
Element-casting weld	Axial	1.6 / 3.1	1.3	D
Ear (hole)	Axial	3.00-3.20	1.3	C
Ear (base)	Bending moment	1.50	-	C
Pin	Shear	1.00	-	specific
Fork (hole)	Axial	3.00	-	C
Fork (base)	Bending moment	1.65	-	C
Weld toe ring stiffener	Axial	1.00	-	F
Casting-radial weld	Bending moment	1.7 / 1.9	1.9	D

Chapter 5

Finite element modelling

In the previous chapter, potential critical locations in the pin connection have been identified. The stress levels in most of these locations could be estimated with hand calculations. The load mechanisms are relatively simple, so the relevant stresses could be calculated with basic equations. The conclusion of this chapter was that not all potential hotspots could be assessed properly. The load mechanism for this location (Fig. 4.20) is more complex and stresses are not easily determined. It is therefore analyzed with finite element (FE) software. FE software is a powerful tool that can be used to solve complex situations. The software package ANSYS is used for the analysis.

Fig. 5.1 shows the floater of the structure. The part that is modeled in ANSYS (the end of the radial member), is indicated. The detail is also shown in Fig. 5.2, including the forces that are exerted by the connected members. Based on the directions and magnitudes of the loads, the potential critical locations in Fig. 5.3 have been identified. This part of the structure is modeled in ANSYS. Note that a second location is identified that was not considered in the previous chapter. It is included in the FE analysis though.

5.1 Objective

The objective of the FE analysis is to find the stress hotspots in the welds at location 1 and 2 (Fig. 5.3). The stress values in these locations can be used to find a relationship that relates the applied loads to the hotspot stress. This relationship is used to calculate a time signal for the hotspot stress, which is used as input for the fatigue damage calculation. The results of the analysis are also used to compare them with the results from the hand calculations from Chapter 4.

5.2 Model

The ANSYS model that is constructed for the analysis is shown in Fig. 5.4. The model is imported from a 3D CAD computer program and modified to make it suitable for the FE analysis. The modifications consist of applying bonded connections between bodies, modelling welds and creating stress read-out points for the regions of interest.

Only one half of the component is modelled. The full model is represented by means of the symmetry condition. This condition restrains displacements perpendicular to the symmetry plane and rotations around the axes in the symmetry plane. Hence, a full geometry is represented by only one half. Using symmetry saves much computation time, compared to a full model. The drawback is that the analysis is restricted to symmetric load cases only. For this study that means that only the 0°and 180°wave direction can be modelled. Non-symmetrical load cases should be analyzed with a full model, although the approach described in this chapter is the same. The wave direction that is simulated in the FE analysis is the 0°wave direction.

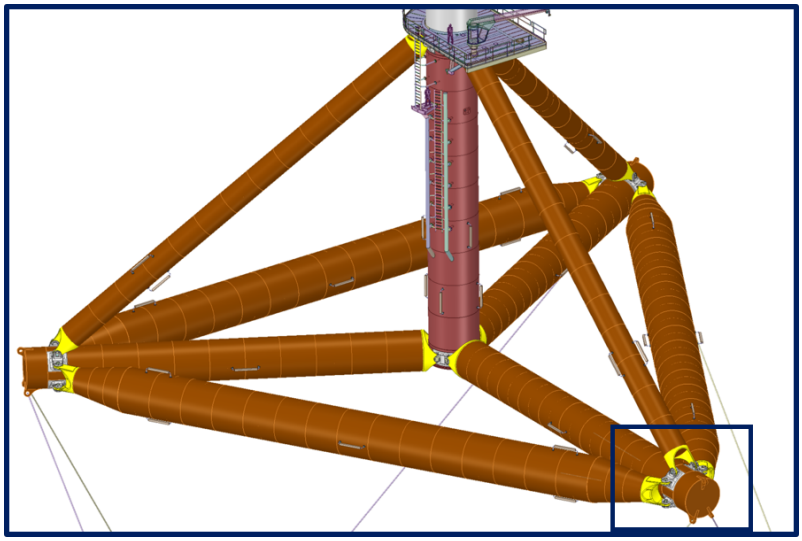

Figure 5.1: Part of the structure that is considered for the FE analysis

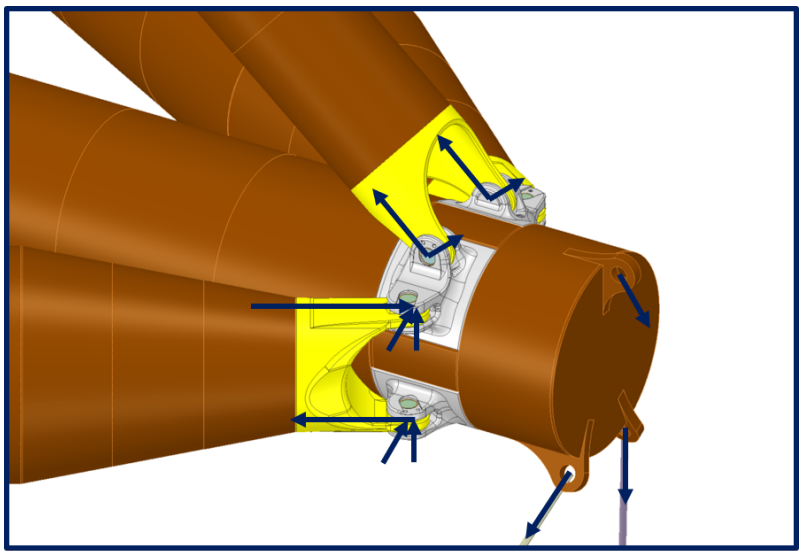

Figure 5.2: Detail of the radial member end with the forces of the connected elements

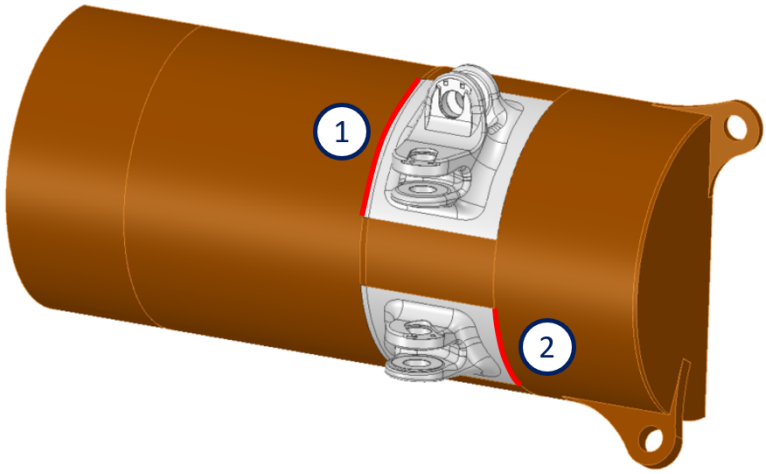

Figure 5.3: Potential critical locations that are considered in the FE analysis

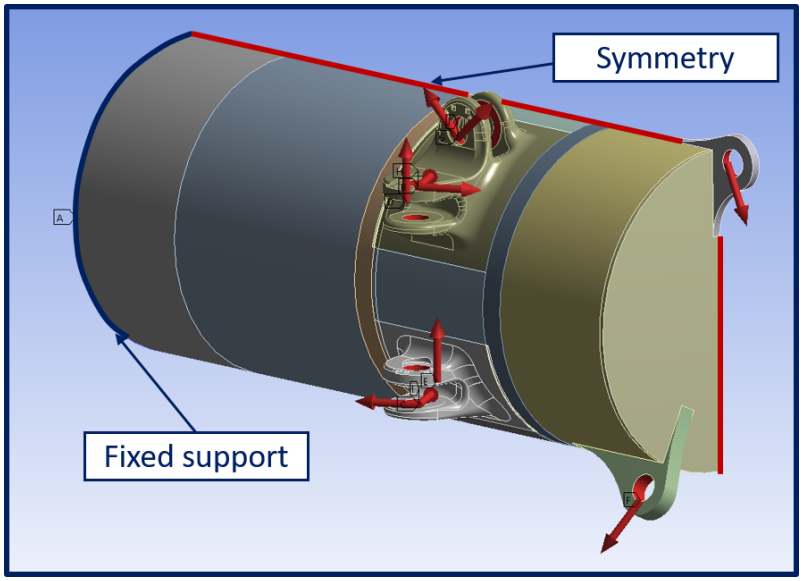

Figure 5.4: ANSYS model with the boundary condition and the symmetry condition

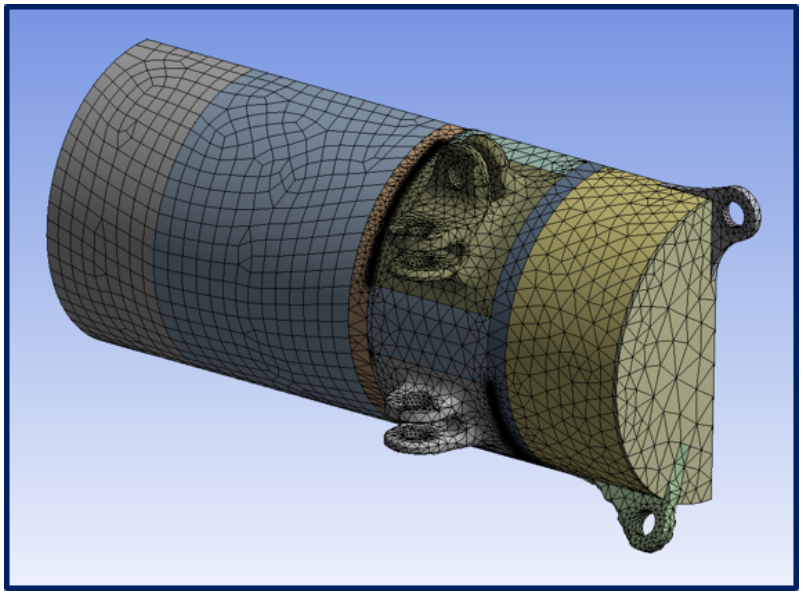

Figure 5.5: Mesh of the ANSYS model (1)

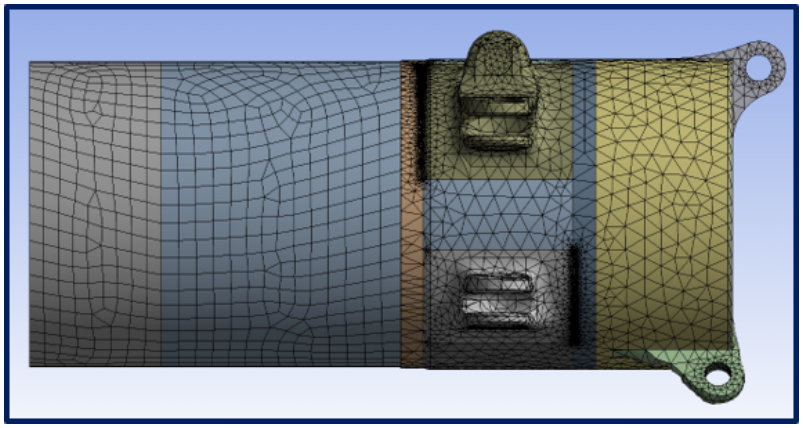

Figure 5.6: Mesh of the ANSYS model (2)

If FE software is used, it is important to keep the limitations in mind. FE software is a powerful tool, but it can be dangerous to rely on the results without properly assessing them. This means that a good FE model should be used, for which the following main criteria should be considered.

1. The detail that is analyzed should be represented by a model at which boundary conditions and loads can be applied at the right locations. In other words, the model should consist of sufficient components, so that the relevant equilibrium can be described.
2. The boundary conditions should not influence the results in the regions of interest.
3. The mesh of the model should be such that it can capture accurate results in the regions of interest.

Below it is explained how these criteria are satisfied for the model.

1. The model includes the locations where loads and boundary conditions are applied. Although the boundary condition for the radial element is actually at the center column, this has been modelled as a fixed support at a distance described in step (2). The underlying assumption of the fixed support is that the internal forces in the radial member are in equilibrium with the forces on the radial member.
2. The only boundary condition is the fixed support at the cut of the radial member. According to the Saint-Venant principle, the effect of a boundary condition slowly vanishes as the distance from the boundary condition increases. In general, this is the case at a distance that is equal to at least the largest dimension of the loaded cross-section [9]. In this model, this is the diameter of the radial member, which is equal to 3.5 [m]. The boundary condition is applied at a distance of $\pm$ 4.5 [m] from the weld, so the criterium is satisfied.
3. For the hotspot method that is described in Chapter 3, [23] recommends an element size in the region of interest of t, where t is the wall thickness of the radial member (equal to 22 [mm]). The mesh elements in the model have a size of 15 [mm], so this criterion is satisfied. Also, at the end of this chapter, a mesh convergence test is performed to confirm that the element size does not significantly influence the results. Note that the element size is mainly important in the regions of interest. Fig. 5.5 and Fig. 5.6 show that only the regions around the potential critical spots are modelled with a fine mesh. For the other parts of the model, a bigger element size is used.

5.3 Method

The objective of this chapter is to translate multiple force signals into one stress signal (for both potential critical locations). The force signals are from the elements that are connected to the radial end. They are calculated in USFOS and used as input for the FE analysis. The output of the analysis is a relationship that relates the applied loads to the resulting hotspot stress. A hotspot stress signal can be calculated in MATLAB, based on this relationship. The stress signal is used for the fatigue calculations. The general flow diagram in Fig. 5.7 shows the steps.

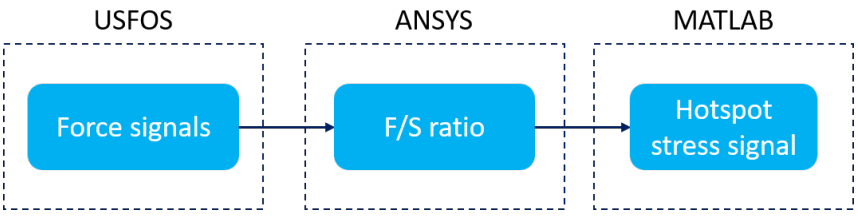

Figure 5.7: General flow diagram for the FE analysis

Fig. 5.8 shows the detailed steps of the calculation of the relationship. First, the relevant loads are determined, based on their expected influence on the stress in the hotspots. The static parts of the force components (the mean values) result from the static equilibrium between weight and buoyancy forces and are not of interest. The time varying part of the forces results from the wave action and ensuing motion and are required for calculating the relevant equilibrium that generate

Figure 5.8: Flow diagram for the calculation of the Force-Stress relationship

Table 5.1: Loads on the radial member

Load description	Standard deviation [kN]	Main load mechanism
Lateral – eq.axial force (upper casting)	**246**	Buoyancy
Lateral – eq.axial force (lower casting)	**200**	Buoyancy
Lateral – transversal force	25	Waves
Lateral – vertical force	**43**	Buoyancy
Diagonal – equivalent axial force	**93**	Inertia
Diagonal – transversal force	0	Waves
Diagonal – vertical force	13	Waves
Suspension line – axial force	**191**	Inertia
Mooring line – axial force	4	Inertia

the fatigue at the hotspots. The varying part is quantified by the standard deviation. The standard deviation is therefore used to identify relevant loads. Loads with an insignificant standard deviation are omitted. The remaining loads are applied to the model and the resulting stresses are calculated by the software. The correctness of the chosen forces for determining the equilibrium required to calculate the hotspot stresses ranges is confirmed by verifying that the force components are all in phase with each other. This is addressed later on in the report. The force-stress ratio is finally calculated by relating the hotspot stress to one of the applied loads. The steps in Fig. 5.8 are discussed in more detail in the next sections.

5.4 Loads

Loads acting on the model of the radial member are from the connected elements, i.e. the lateral member, a diagonal member, a suspension line and a mooring line. Theoretically, each element can exert forces in six degrees of freedom on the radial. However, many force components can be eliminated, so that only nine components remain. The relevant loads are kept, and the irrelevant loads are eliminated based on the following assumptions.

- The internal moments in the diagonal and lateral elements can be represented by a force couple. These forces are in the same direction as the axial force and can therefore be combined with the axial force. Note that this approach is also used and explained in Section 4.3.
- Some forces (for example the vertical force on the lateral member) are evenly distributed over the upper and lower casting
- Torsion forces in the elements are neglected, as they are found to be insignificant
- Moments in the rotation planes of the hinges are negligible
- The suspension line and mooring line are cables and transfer axial force only

The number of unique remaining loads is nine, see Table 5.1. The significance of each remaining load is checked, so that the model can be further simplified by eliminating insignificant loads. This is done by calculating the standard deviation of each force signal. The standard deviation is a measure for the variability of the signal, and it is the governing factor for the calculation of the fatigue damage. The fatigue damage is calculated based on the Rayleigh distribution of the stress ranges and the Rayleigh distribution depends on the standard deviation only (refer to Chapter 3).

Table 5.1 shows the loads, the standard deviation and the main load mechanism behind the load. The significant loads are highlighted in bold. The values in the table show that there are multiple force signals with a very small standard deviation, compared to the other ones. These non-significant loads are omitted, as their influence on the hotspot stress (and the fatigue damage) are

Table 5.2: Overview of the load cases with the standard deviations of the forces

	Lateral			Diagonal	Susp. line
Load case	Eq.ax. force (upper casting)	Eq.ax. force (lower casting)	Vertical force	Eq.ax. force	Axial force
1	245.9	200.2	42.9	-	-
2	-	-	-	92.9	-
3	-	-	-	-	191.3
4	245.9	200.2	42.9	92.9	191.3

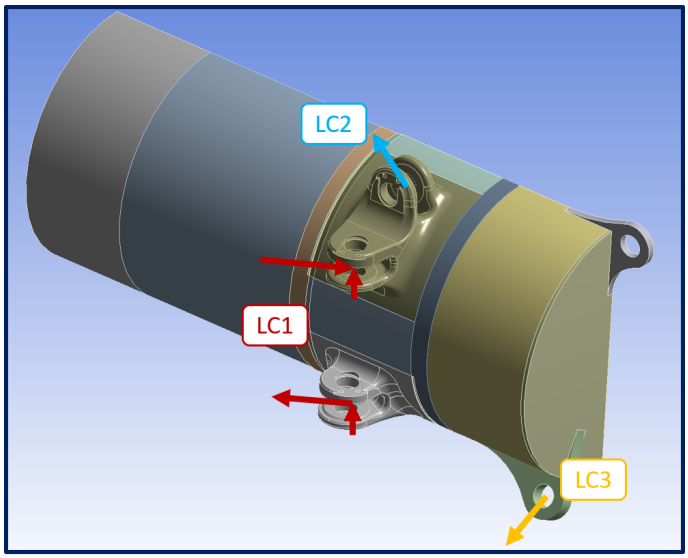

Figure 5.9: Graphical representation of the load cases

expected to be negligible.

Multiple load cases are defined, so that the influence of the individual load cases on the hotspot stresses can be determined. The number of load cases can be reduced if multiple forces are combined in one load case, which is done for the loads with the same main load mechanism. This holds for the vertical force and the equivalent axial forces in the lateral element, which are mainly caused by the vertical buoyancy load on the lateral member. Two other load cases consist of only one force and the last load case consists of all relevant loads. The forces are applied to the model, with a magnitude equal to the standard deviation of the force signal. The load cases are summarized in Table 5.2 and graphically shown in Fig. 5.9. Refer to Appendix C for the results of a fifth load case. This load case consists of all the loads shown in Table 5.1. It is shown that the omitted loads have a negligible influence on the results, as expected based on the standard deviations.

5.5 Hotspot stress

After construction of the model and application of the loads, the software solves the system and calculates the stresses. The stresses are obtained at the locations of the hotspots. However, it is not straight-forward to determine which stress value should be used as 'the hotspot stress'. Fig. 5.10 shows an example of the stress map around location 1. Every node in the mesh has a different value, so a definition for the hotspot stress is needed. Also, there are other aspects that should be considered when the fatigue damage is calculated based on the results of an FE analysis. This is discussed in more detail in this section.

Stress concentrations result from global geometry (items such as holes and stiffness changes) and weld geometry (items such as weld notches and heat affected zones). For the hand calculations in Chapter 4, the SCF from the global geometry is obtained from literature or is manually derived.

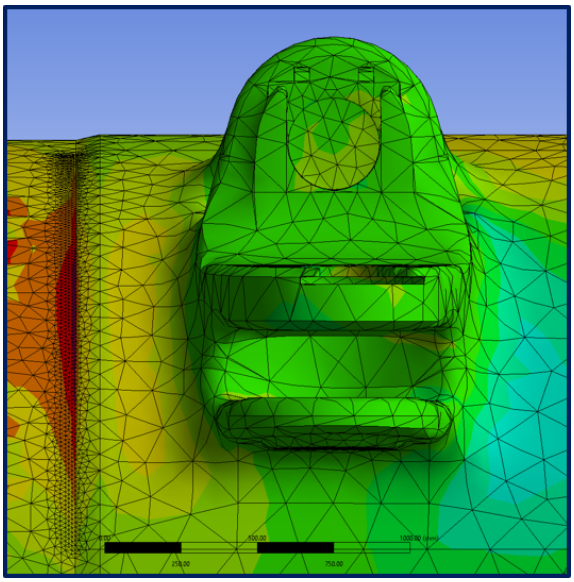

Figure 5.10: Example of the observed stress pattern from an FE analysis

The hotspot stress is calculated by multiplying the SCF with the nominal stress. The SCF resulting from weld geometry was accounted for in the SN-curve used for the detail.

For an FE analysis however, it is difficult to distinguish the nominal stress and the hotspot stress, and which SN-curve should be used. This could be solved by constructing a model with a realistic geometry of the welds, to calculate the hotspot stress at the toe of the weld. This stress could directly be used with a C-curve, because all the stress concentrations are already considered in the FE model. The realistic weld geometry should then include all weld features, including the weld toe which is typically in the order of magnitude of a millimeter. Hence, very small mesh elements should be used, and the model would increase to an unacceptable size.

It is therefore recommended in [23] to model the weld with a simple geometry (usually a fillet), so that only the stress concentrations from the geometry are considered. The stress concentrations resulting from the weld are considered by using a lower SN-curve, the D-curve. In this way, a more coarse mesh can be used, resulting in reduced computation time. The consequence of modelling the weld as a fillet is a geometrical discontinuity at the weld toe (see Fig. 5.11). This leads to a stress that goes to infinity as the mesh element size goes to zero. This makes it difficult to determine the hotspot stress at this location.

The hotspot method is used to overcome this problem [23]. In this method, the stress levels are read out at two distances from the stress hotspot. The stress, as function of the distance from the hotspot, is extrapolated to the location of the hotspot. The distance of the read-out points should be close enough to capture the stress concentration, but far enough to not result in unrealistic stress values. The recommended distances are at $0.5t$ and $1.5t$, where t is the thickness of the plate of the radial element. The method is graphically shown in Fig. 5.12.

Once the hotspot stress is known, a force-stress relationship can be determined. [23] prescribes that for fatigue calculations the effective stress range should be used as 'the hotspot stress'. The effective stress is given by the maximum value of the three stress values shown in Eq. (5.1). In this equation, σ_1 and σ_2 are the maximum and minimum principle stresses respectively. The value of α depends on the quality of the weld, i.e. for a high-quality weld the reduction factor α is lower. For the modelled situation, alpha is equal to 0.72 according to the requirements in [23].

$$\sigma_{eff} = max \begin{cases} \sqrt{\Delta\sigma_{\perp}^2 + 0.81\Delta\tau_{\parallel}^2} \\ \alpha|\Delta\sigma_1| \\ \alpha|\Delta\sigma_1| \end{cases} \tag{5.1}$$

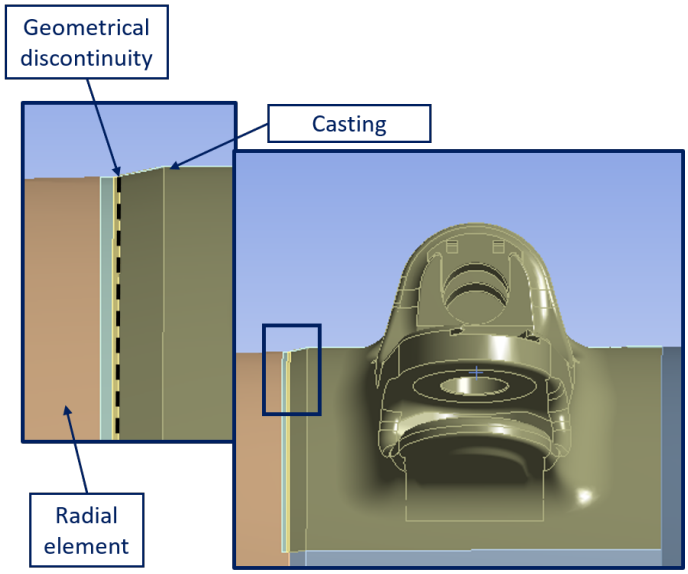

Figure 5.11: Geometrical discontinuity between the casting and the radial element

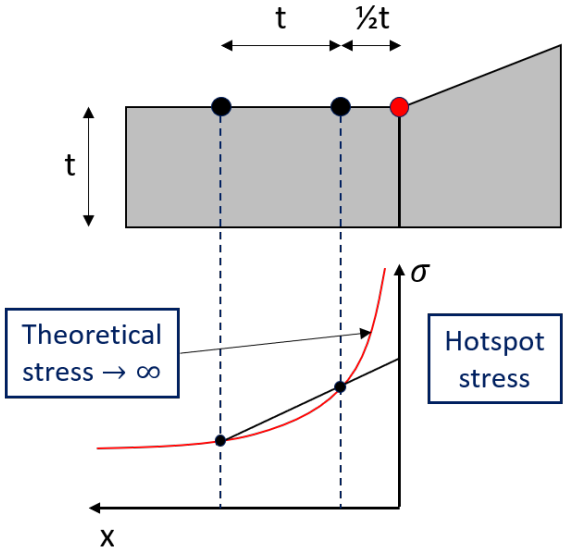

Figure 5.12: Explanation of the hotspot method to estimate the hotspot stress

5.6 Results

The load cases are applied on the model and the stresses are calculated. The results are shown in Table 5.3 and Table 5.4 for location 1 and in Table 5.5 and Table 5.6 for location 2. The results for the individual load cases (LC1 to LC3) are presented, and the contribution to the total stress is shown. LC4 is the load case that includes all the relevant loads, and it is used for the calculation of the force-stress relationship. In Appendix C the results of a fifth load case can be found. This load case includes all the loads from Table 5.1. Note that the results for the principal stress are not shown. For both locations and all load cases, the first term in Eq. (5.1) was the highest effective stress value. Also note that the presented stresses are based on the standard deviations of the forces, and not the actual value of the forces.

The following conclusions can be drawn from the presented results. These conclusions are used for the calculation of the force-stress relation in the next section.

- LC1, LC2 and LC3 are all relevant for the effective stress in hotspot 1.
- Only LC1 and LC3 are relevant for the effective stress in hotspot 2. The effect of LC2 is negligible.
- The maximum value for the effective stress in Eq. (5.1) is in all cases the combined normal and shear stress. The principle stresses are therefore not relevant for this analysis.
- The contribution of shear stress to the effective stress is small

5.7 Force-stress relationship

The results from the FE analysis (table Table 5.3 to Table 5.6) are for only one combination of applied loads. However, the loads are actually signals, in which the magnitude of the force varies as a function of time. It is not possible to do an FE analysis for every step in the time signal. Therefore, two ratios are calculated that relate the applied loads to the stresses in the hotspots for location 1 and 2 respectively. The relationships are obtained from the results of the FE analysis and they are used to translate the force signal to a stress signal.

The derivation is based on the assumption that the five variables loads represent a state of equilibrium. Consequently, four variables can be expressed as a function of the fifth load, as shown in Eq. (5.2). However, this approach is only valid if α_i is not dependent on time. In other words, there should be a constant ratio between the five load signals. This means that the signals should be in-phase with each other and the variation of the signals (around their mean) should have a constant ratio. In Fig. 5.13, the variation of the five time signals is shown. These plots are obtained by subtracting the mean value of the signals. Note that only a sample of the signal is plotted, to increase the readability.

$$F_i(t) = \alpha_i \cdot F_1(t) \tag{5.2}$$

From the figure it is observed that the signals are very much in phase and they appear to have approximately a constant ratio as well. To quantify these observations, Pearson's Correlation Coefficient is used [4]. This coefficient is a measure of the linear correlation between the signals, and it is calculated with Eq. (5.3) The value of this coefficient can range from 1 to -1. A value 1 or -1 indicates a perfect linear correlation, whereas a value of 0 indicates no linear correlation at all. Though, if the value is (close to) zero, there can still be a different correlation, for example a quadratic one. If there is a linear correlation between two signals, it means that one signal can be expressed as a linear combination of the other signal, i.e. in the form of Eq. (5.2).

Table 5.7 shows the correlation coefficients for the force signals. Please note that these coefficients are for the full signal, and not only for the sample shown in Fig. 5.13. It is shown that there tend to be a linear correlation between the signals. The strongest correlation is between the force signals in the lateral element and in the suspension line. The correlation coefficients of the force signal in the diagonal element is somewhat lower, but it is assumed that they are sufficiently high to express the signal as a function of one of the other signals.

Table 5.3: Normal stress results for location 1

Normal stress		
Load case	Hotspot stress [MPa]	Contribution
1	8.21	53%
2	-2.88	19%
3	4.42	28%
4	9.76	

Table 5.4: Shear stress results for location 1

Shear stress		
Load case	Hotspot stress [MPa]	Contribution
1	-0.71	21%
2	-0.84	24%
3	1.91	55%
4	0.36	

Table 5.5: Normal stress results for location 2

Normal stress		
Load case	Hotspot stress [MPa]	Contribution
1	4.72	79%
2	-0.08	1%
3	-1.18	20%
4	3.46	

Table 5.6: Shear stress results for location 2

Shear stress		
Load case	Hotspot stress [MPa]	Contribution
1	0.53	40%
2	-0.11	8%
3	0.69	52%
4	1.11	

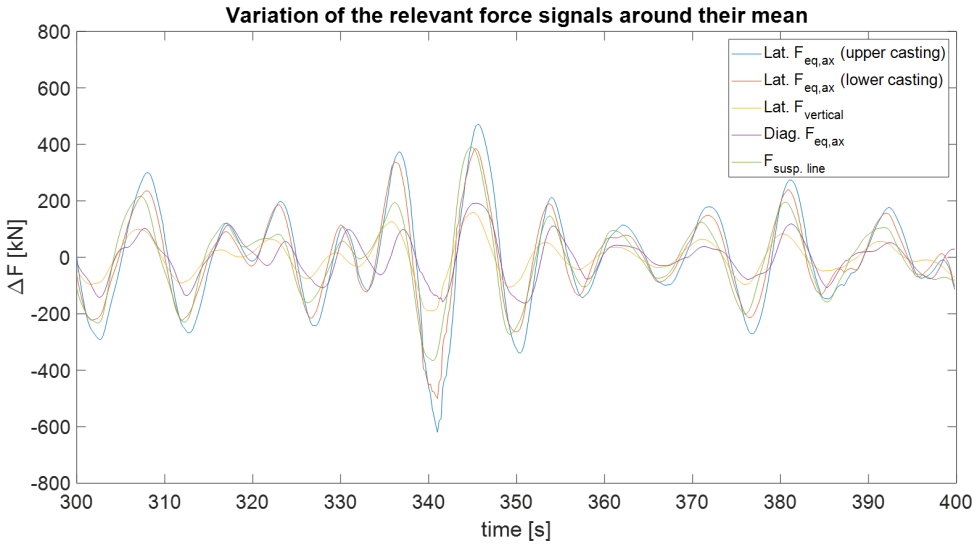

Figure 5.13: Sample of the five force signals

Table 5.7: Correlation coefficients for the full force signals

		Lateral			Diagonal	Suspension line
		$F_{ax,eq}$ (U)	$F_{ax,eq}$ (L)	F_z	$F_{ax,eq}$	F_{ax}
	$F_{ax,eq}$ (U)	1.00	0.97	0.96	0.86	0.93
Lateral	$F_{ax,eq}$ (L)	0.97	1.00	0.90	0.87	0.87
	F_z	0.96	0.90	1.00	0.83	0.97
Diagonal	$F_{ax,eq}$	0.86	0.87	0.83	1.00	0.91
Susp	F_{ax}	0.93	0.87	0.97	0.91	1.00

$$PCC(F_j, F_k) = \frac{1}{N-1} \cdot \sum_{i=1}^{N} \left(\frac{F_{j,i} - \mu_{Fj}}{\sigma_{Fj}} \right) \left(\frac{F_{k,i} - \mu_{Fk}}{\sigma_{Fk}} \right) \tag{5.3}$$

Based on the results in Table 5.7, the loads are expressed as function of a force signal times a certain constant, α_i. The constant is equal to the ratio between the standard deviations of the signals. The load with the highest standard deviation is selected as the representative force. In Table 5.8, the values for α_i are listed.
The underlying assumption for this approach is that the magnitudes of the loads always have the same ratio, because of equilibrium. Consequently, the force-stress ratio is calculated based on one representative force only. The force-stress ratio is calculated by dividing the hotspot stress by the magnitude of the representative load, which is equal to the standard deviation, as shown in Eq. (5.4).

$$FS_i = \frac{\sigma_{hotspot,i}}{StdDev(F_{repr})} \tag{5.4}$$

The value of the hotspot stress is the effective stress (calculated with Eq. (5.1)) and based on the results shown in Table 5.3 and Table 5.4 for hotspot 1 and Table 5.5 and Table 5.6 for hotspot 2.

Table 5.8: α-values for the force signals

Force signal	StdDev [kN]	α
Lateral – equivalent axial force (upper casting)	246	1.00
Lateral – equivalent axial force (lower casting)	200	0.81
Lateral – vertical force	42	0.17
Diagonal – equivalent axial force	93	0.38
Suspension line – axial force	191	0.76

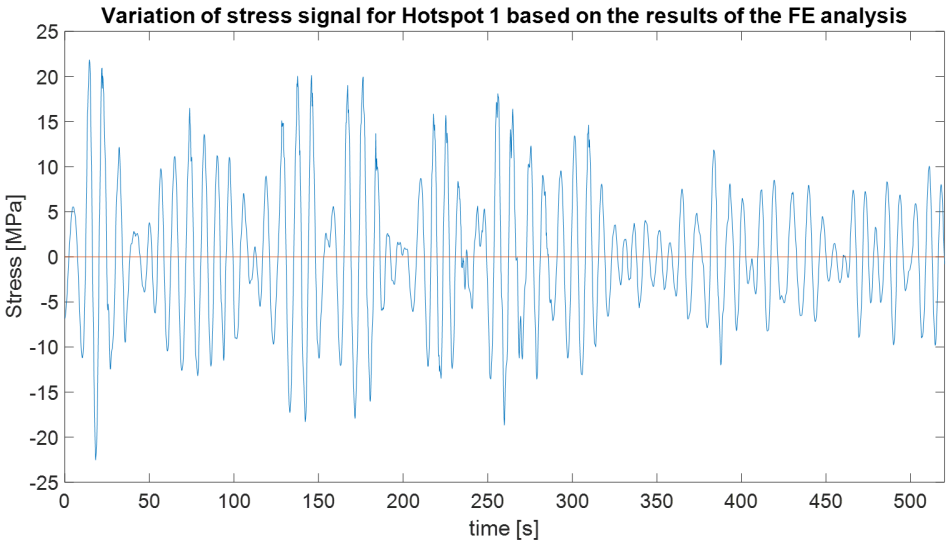

Figure 5.14: Variation of the stress signal for hotspot 1

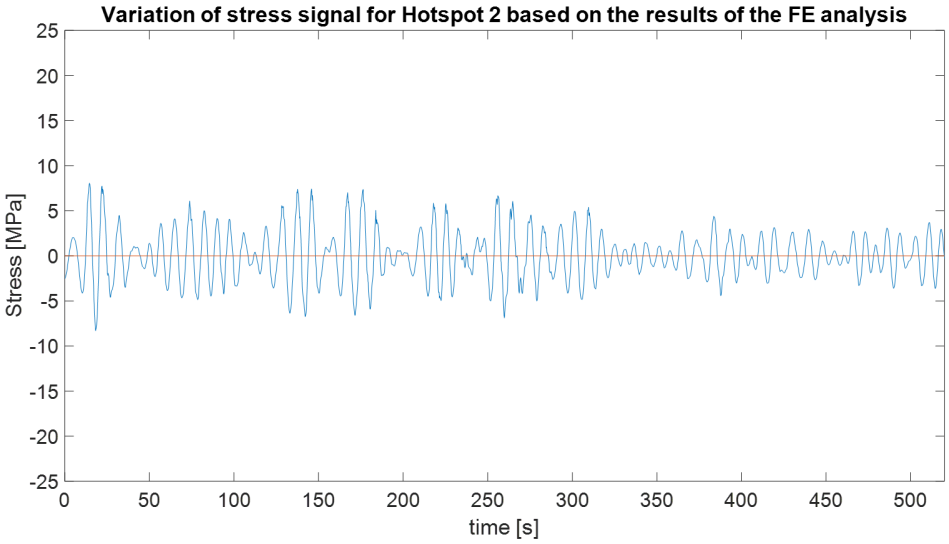

Figure 5.15: Variation of the stress signal for hotspot 2

Eq. (5.5) and Eq. (5.6) show the calculation of the force-stress ratios.

$$FS_1 = \frac{9.77[MPa]}{246[kN]} = 0.0579 \left[\frac{MPa}{kN}\right] \tag{5.5}$$

$$FS_2 = \frac{3.60[MPa]}{246[kN]} = 0.0182 \left[\frac{MPa}{kN}\right] \tag{5.6}$$

The stress signals for hotspot 1 and 2 can finally be expressed as shown in Eq. (5.7). Note that the discussed approach is based on the ratio of the standard deviations, which is not necessarily equal to the ratio in mean values. Therefore, only the variation of the signals can be used for further calculations. The variations of the stress signals are shown in Fig. 5.14 and Fig. 5.15. These signals are used as input for the fatigue calculations in the same way as the stress signals calculated in Chapter 4.

$$\sigma_i(t) = FS_i \cdot F_{repr}(t) \tag{5.7}$$

5.8 Mesh convergence

A common issue with FE analyses is that results can be dependent on the size of the mesh elements. An example of this is already discussed in Section 5.5, where the stress at the discontinuity tended to go to infinity for a decreasing mesh element size. A similar problem can arise at locations other than discontinuities. In general, this problem is caused by a too coarse mesh. Although a mesh size smaller than the recommended size by [23] is used for the analyses in this thesis, a mesh convergence test is carried out to ensure that the results do not depend on the mesh size. The test consists of a simulation with exactly the same input parameters, but with a very fine mesh. The objective is to compare the hotspot stresses of both meshes. The results are shown in Table 5.9. The table shows the element size, the corresponding number of nodes and the resulting hotspot stress at hotspot 1. Note that the hotspot stress is calculated, using the method, discussed in Section 5.5. From the data in the table it is observed that the difference in hotspot stress is only five per cent, whilst the number of nodes is almost four times higher. It is therefore concluded that for an element size of 15 [mm] there is a good trade-off between accurate results and the number of nodes.

Table 5.9: Results of the mesh convergence test

Element size [mm]	Number of nodes	Hotspot stress [MPa]
15	50201	9.76
4	191973	9.29
	difference	**-5.2%**

Chapter 6

Comparison of methods

In Chapter 4 and Chapter 5, stress signals have been calculated for several locations in the pin connection. One of the locations was difficult to assess with hand calculations and hence an FE-analysis was performed to find more accurate results. In this chapter, the results of the methods are compared. The objective of the comparison is to determine whether hand calculations can be used to approximate the hotspot stress signal and to gain a more in-depth insight in the results of the FE analysis.

The stress signals for the methods are based on the input and assumptions shown in Table 6.1. The first row shows the reference force signals on which the stress signals are based. For the hand calculations, the results are based on the signals of the relevant internal forces *in* the radial member. That is, the axial force and the bending moment. The stress signal resulting from the FE procedure is based on a force signal of the force applied *on* the radial member. More specific, the loads applied on the member are represented by a single force signal (refer to Chapter 5). This load is the equivalent axial force on the upper casting, which is a combination of the internal axial force and bending moment in the lateral member.

In the second row of the table it is described how the hotspot stress is calculated. For the hand calculations, it is assumed that both the axial force and the bending moment in the radial member are transferred through the welds only. The corresponding SCFs are derived, based on the ratios between areas (for axial stress) and section moduli (for bending stress) of the total circumference and the circumference covered by the welds. Also, an SCF is introduced to account for the difference in plate thickness at the hotspot. The expression for the hand calculated hotspot stress is shown in Eq. (6.1)

The hotspot stress signal calculated from the FE analysis uses the results from ANSYS to obtain a relationship between the applied loads and the resulting hotspot stresses.

$$\sigma_{hand} = SCF_t \cdot \left(SCF_a \cdot \frac{F_{ax,R}}{A_{tot}} + SCF_b \cdot \frac{M_{b,R}}{W_{tot}} \right) \tag{6.1}$$

The variation of the stress signals is shown in Fig. 6.1 (recall that fatigue damage is governed by the standard deviation of the stress signal). The signals are obtained by subtracting their respective mean values and they are used to assess whether the calculation methods will result in equal fatigue damage results. Some observations are made from the figure (see below). The observations are quantified with the values shown in Table 6.2. The table shows Pearson's Correlation Coefficient (calculated with Eq. (5.3)) and the ratio of the standard deviations.

- The signals are very strongly correlated. This suggests that they represent a state of equilibrium.
- The standard deviation of the hand calculated signal is lower than the standard deviation of the signal from FE analysis. The fatigue damage calculated from this signal will therefore be lower as well. The difference can result from several causes.

Table 6.1: Input and assumptions for the two methods of stress calculation

	Hand calculation	FE analysis
Reference time signal	Internal force *in* the radial member • Axial force (radial) • Bending moment (radial)	Force of the connected element *on* the radial member. Represented by the internal forces in the lateral element • Axial force (lateral) • Bending moment (lateral)
Hotspot stress calculation	Axial component: $\frac{L_{tot}}{L_{weld}}$ Bending component: $\frac{W_{tot}}{W_{weld}}$ Stress raiser due tot change in plate thickness	Force-Stress relationship calculated by relating the hotspot stress to the applied loads

Table 6.2: Correlation coefficient and ratio between the standard deviations of the stress signals

Correlation coefficient	0.98
StdDev(σ_{hand})/StdDev(σ_{FE})	0.89

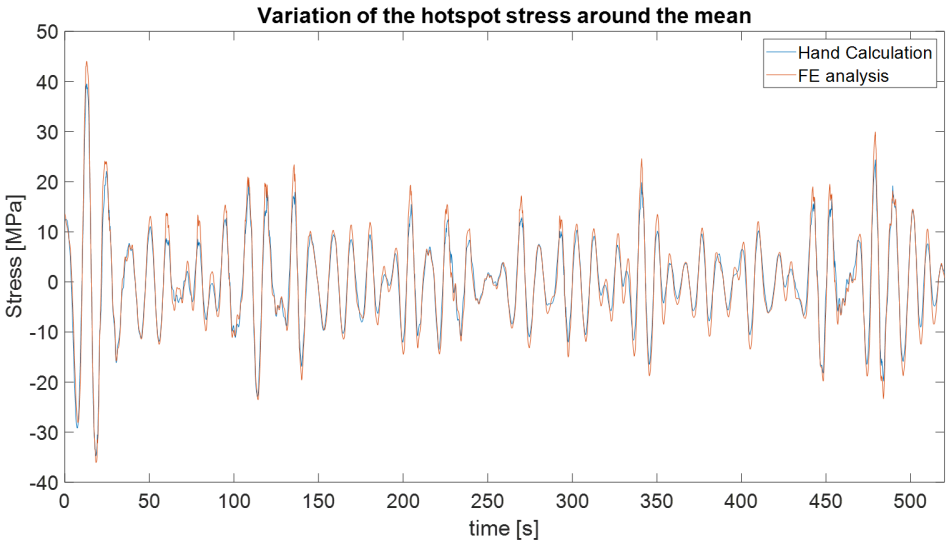

Figure 6.1: Variation of the stress signals of both methods

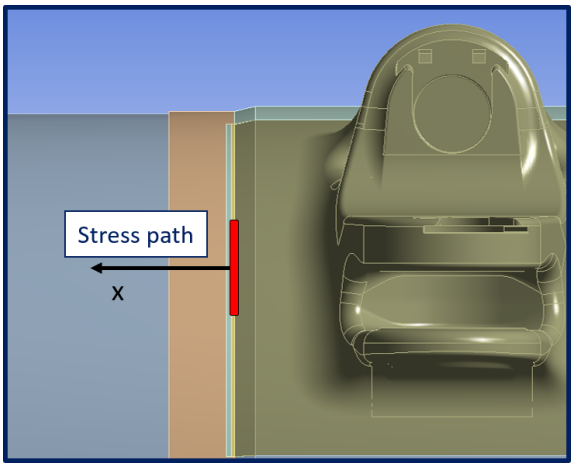

Figure 6.2: Schematic representation of a stress path starting at the hotspot

6.1 Differences

The calculation methods of the stress signals are analyzed to find a possible explanation for the difference in standard deviation that is observed in Fig. 6.1. To do so, the components of the hand calculated signal (listed in Table 6.1) are studied one by one. Each component is quantified and compared with analogous results from the FE analysis. The conclusions of the comparisons serve as a basis for the objective of this chapter.

6.1.1 Local bending moment

The first component that is analyzed is the stress raiser due to change in plate thickness (SCF_t in Eq. (6.1)). This term represents the effect of local bending moments, caused by the change in plate thickness at the hotspot. In the hand calculations this effect is accounted for by means of an SCF that is calculated based on the recommendations in [23]. The value for the considered location is equal to 1.93, as derived in Chapter 4.

For the FE calculations, the SCF attributed to local bending is determined based on the observed stress patterns. The stresses in and around the hotspot are visualized by means of stress paths. A path represents a line of points at which the stress values are read out. Fig. 6.2 schematically shows the stress path on the outside of the radial element, starting at the stress hotspot. A second path is constructed at the same position, but on the inside of the element. In this way, the effect of local bending stress can be derived. The stresses, as a function of the distance x, are shown in Fig. 6.3. Several observations are made:

- The stress on both the inside and the outside of the shell tend to go to a constant value from the distance $x > 400[mm]$. This is assumed to be the nominal stress.
- The stress close to the hotspot quickly increases at the outside and decreases at the inside of the shell. This effect is attributed to the local bending moment.
- The stresses along the paths vary not in a symmetrical way, compared to the constant value (at $x > 400[mm]$). A linear trend is observed, that increases as the distance to the hotspot decreases. This effect is attributed to local deformation of the shell, caused by the applied loads. A visualization of this effect is shown in Fig. 6.4.

The observations are analyzed as follows. The total contribution of the two local effects combined (deformation and local bending) can be quantified with Eq. (6.2), where the hotspot stress is divided by the nominal stress. However, the local deformation effect is not considered in the hand calculations, so the linear trend attributed to this effect is removed from the stress paths. In this way the effect of local bending only can be compared to the term SCF_t from the hand calculations. Fig. 6.5 shows a plot of the resulting stress paths, which are used to quantify the effect attributed

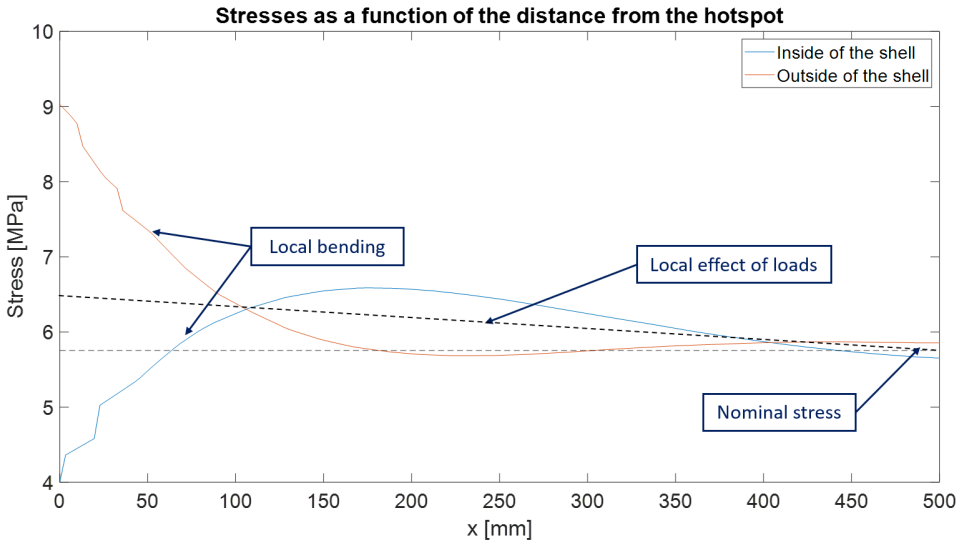

Figure 6.3: Stress on the in- and outside of the radial member as a function of the distance along the stress path

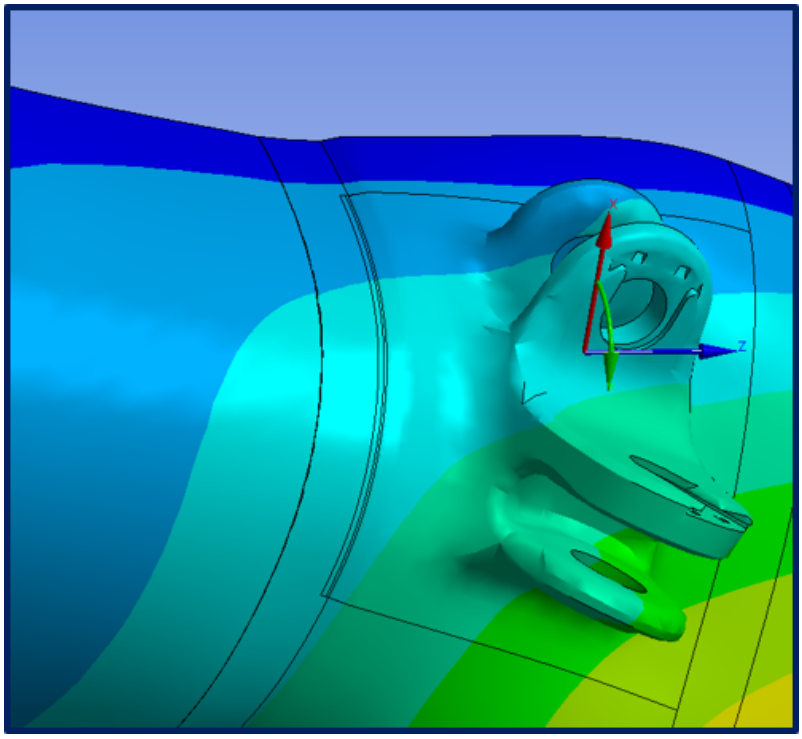

Figure 6.4: Visualization of the local load effects

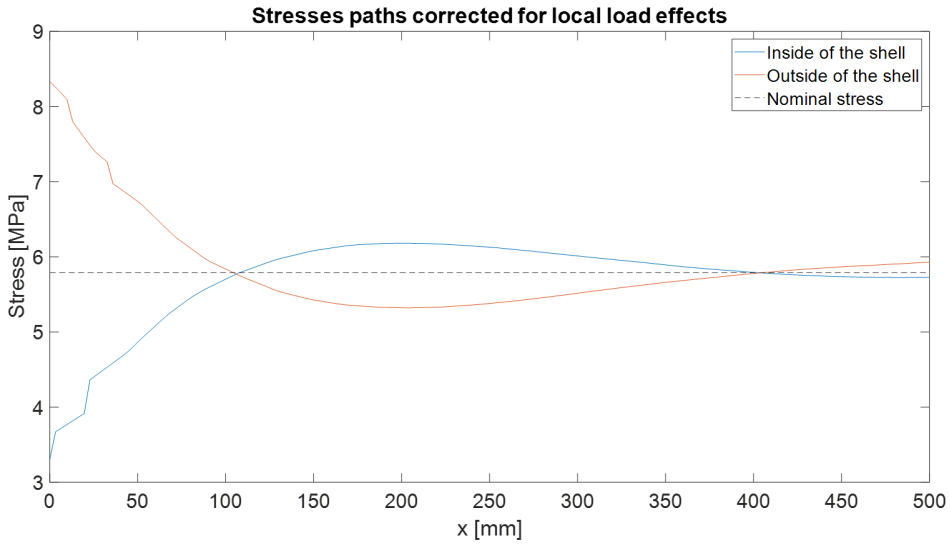

Figure 6.5: Stress path from the FE model, corrected for the local effects

to local bending. This is done with the expression shown in Eq. (6.3), where the 'corrected' hotspot stress is divided by the nominal stress.

If the resulting SCF is compared to the SCF calculated based on the recommended equation in [23] (equal to 1.93), it is concluded that the latter overestimates the effect of local bending. Consequently, the full (hand calculated) hotspot stress signal is overestimated as well. This is a remarkable difference between the signals, but it is not an explanation for the different standard deviations. In fact, it means that the difference would be even larger if equal SCFs for both signals would be used.

$$SCF_{tot,FE} = \frac{\sigma_{hotspot}}{\sigma_{nominal}} = 1.57 \qquad (6.2) \qquad\qquad SCF_{b,FE} = \frac{\sigma_{hotspot'}}{\sigma_{nominal}} = 1.45 \qquad (6.3)$$

6.1.2 Stress distribution

The second component that is compared, is the factor that is used to translate nominal stress to hotspot stress in the hand calculations. Recall that for the hand calculations all the axial force and the bending moment are assumed to be transferred through the circumference covered by the welds only. Separate SCFs for axial stress and bending stress are calculated, based on this assumption (refer to Section 4.6.

The correctness of this assumption is validated with the results from ANSYS. The fraction of the force that is transferred through the welds is calculated with Eq. (6.4). The validation consists of comparing the result from this equation with the fraction from the hand calculation, which is assumed to be equal to one.

The terms in Eq. (6.4) are derived from a stress distribution plot. Fig. 6.7 shows the stress distribution from the FE analysis along the circumference of the radial member, at the cross-section of the hotspot. The definition of the distance x is schematically shown in Fig. 6.6. The plot shows the total stress distribution, which is composed of both the axial stress and the global bending stress. The effect of local bending stress is eliminated, by taking the average of the path on the inside and outside of the radial member.

The force (per unit length) can be calculated with Eq. (6.5). The equation is used to calculate the force transfer through the welds (equal to the areas within black dotted lines in Fig. 6.7) and the force transfer through the total cross-section (equal to the total area under the stress distribution curve). The results are substituted in Eq. (6.4). This results in a ratio of 0.70. It is therefore

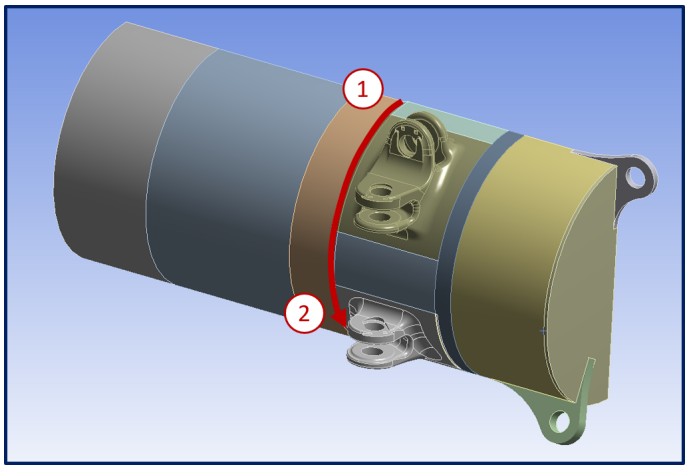

Figure 6.6: Definition of the path along which the stress distribution is checked

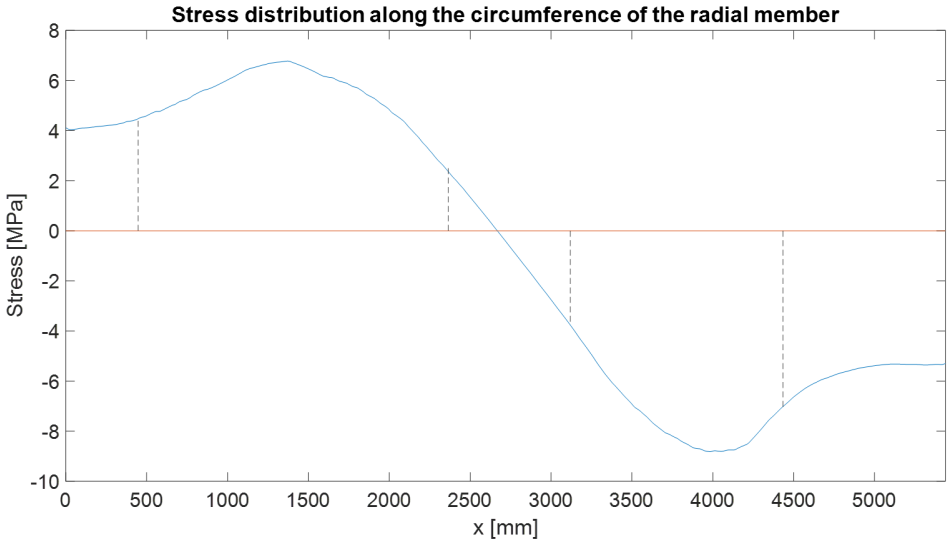

Figure 6.7: Stress distribution along the path. The dashed lines indicate the locations of the castings

concluded that 70% of the internal forces are transferred through the welds, based on the results from ANSYS. For the hand calculations it is assumed that this ratio is 100%, which means that the amount of force transferred through the welds is overestimated. Consequently, the total hotspot stress signal from the hand calculation is overestimated as well.

$$f = \frac{F_{weld}}{F_{total}} \tag{6.4}$$

$$F = \int \sigma(x)dx \tag{6.5}$$

6.1.3 Axial force and moment transfer

In Table 6.1 it is shown that both calculation methods use different reference signals to calculate the hotspot stress signals (Table 6.1). The objective of this section is to determine whether the magnitudes of the reference signals agree with each other. The following comparisons are made. They are explained below.

- The reference force signals from the hand calculations are compared with the forces that are derived from the FE analysis. The forces are derived are derived from stress distribution plots, similar to the approach from the previous section. The loads that are applied on the FE model are equal to the standard deviations. The internal forces from the FE model

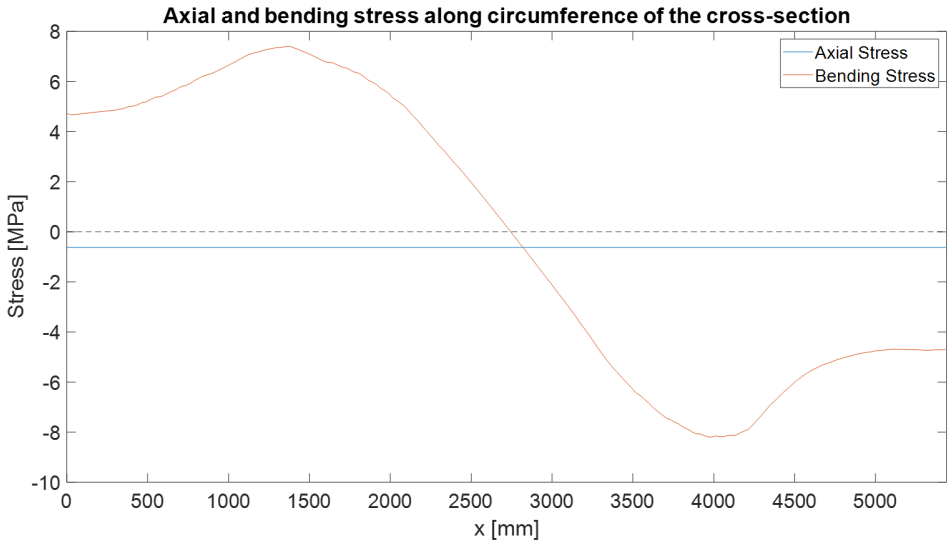

Figure 6.8: The stress distribution is decomposed in an axial stress and a bending stress

Table 6.3: Axial force and bending moment for the two methods

	Hand calculation	FE analysis	ratio FE/HC
Axial force [kN]	-101.1	-91.1	0.90
Bending moment [kNm]	302.3	743.9	2.46

are therefore compared with the standard deviations of the force signals from the hand calculations.

- The comparison can also be reversed. The internal axial force and bending moment from the hand calculations are then used to derive a theoretical stress distribution. This is compared with the stress distribution obtained from the FE analysis. This should yield approximately the same results.

The hotspot stress signal from the hand calculations is based on two force signals. These are the axial force and the bending moment signal in the radial element. The FE analysis uses the external forces from lateral element, which are assumed to be in equilibrium with the internal forces in the radial element. This assumption is verified by comparing the forces in the radial member from the hand calculations with the values found in the FE analysis.

The internal forces from the hand calculations are directly derived from USFOS. The internal forces from the FE model are calculated in the analysis. The resulting internal forces are calculated based on the stress distributions along the circumference (see Fig. 6.6). This distribution is decomposed in an axial stress and bending stress distribution, assuming that the bending stress at the middle of the element is equal to zero. The result is shown in Fig. 6.8. The plots are used to calculate the internal axial force and the internal bending moment in the cross-section of the ANSYS model with Eq. (6.6) and Eq. (6.7) respectively. The results of these equations and the corresponding internal forces from the hand calculations are shown in Table 6.3. Note that the values in the table represent the internal forces in a half cross-section for both methods. From the table it is concluded that the axial forces agree well. The bending moment however, is significantly larger in the FE analysis compared to the bending moment from the hand calculations.

$$F_{ax} = \int \sigma_{ax} dA = \int_{-\frac{\pi}{2}}^{\frac{\pi}{2}} \sigma_{ax} \cdot R t d\theta \tag{6.6}$$

$$M = \int \sigma_{bend} \cdot r dA = \int_{-\frac{\pi}{2}}^{\frac{\pi}{2}} \sigma_{bend} \cdot R^2 t d\theta \tag{6.7}$$

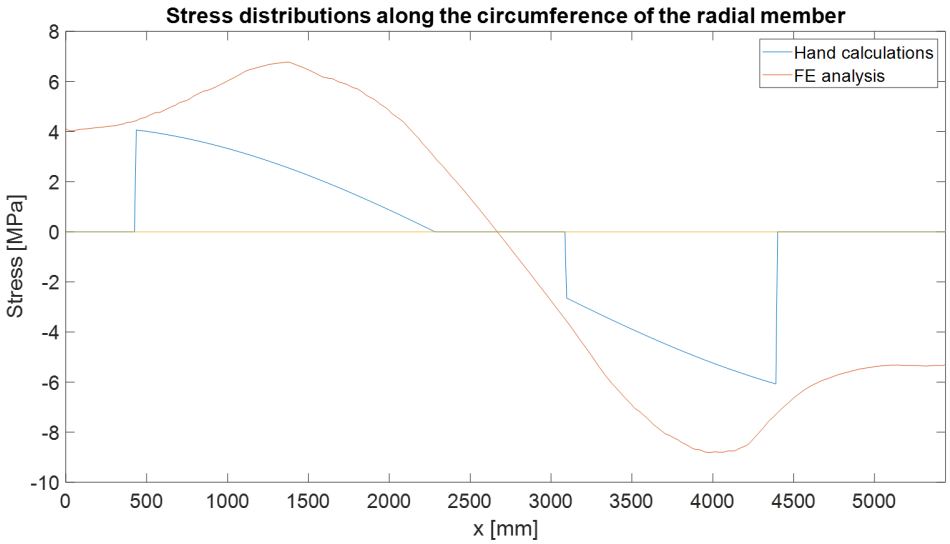

Figure 6.9: Stress distributions of the FE analysis and the theoretical distribution calculated with Eq. (6.8)

These conclusions are checked by following the inverse approach. The theoretical stress distribution is calculated based on the internal forces from the hand calculations and the assumptions that have been made in Chapter 4. The analytical expression for the theoretical distribution is shown in Eq. (6.8). The areas under this distribution and the one from the FE analysis, should have approximately the same ratio as the ratio between the bending moments in Table 6.3.

$$\sigma_{hand}(x) = SCF_a \cdot \frac{F_{ax}}{A} + SCF_b \cdot \frac{M \cdot y(x)}{I} \tag{6.8}$$

Fig. 6.9 shows the stress distributions. The areas under the curves are calculated with Eq. (6.5). The ratio of the areas is determined with Eq. (6.9), which results in a value of approximately 2.6. This confirms the conclusion that there is a significant difference between the reference signals of the calculation methods. A possible explanation for the difference is discussed in the next section.

$$\frac{\int \sigma_{fe}(x)dx}{\int \sigma_{hand}(x)dx} \tag{6.9}$$

6.1.4 Bending moment difference

From Fig. 6.9 and Table 6.3, it is concluded that there is a large difference in the bending moment obtained from USFOS and from the FE analysis. The following explanation for this difference is formulated after investigation of the models.

Fig. 6.10 shows the end of the radial member in the USFOS model. The members and the cables (mooring cable and suspension line) are all connected in one node. This node is a fixed connection, which implies that the internal moment in the radial member is determined based on the equilibrium with the moments in the other elements. The moment in the radial is therefore equal to the moment in the lateral members minus the moment in the diagonal member. Note that the moment in the diagonal is not equal to zero, because the pin connection is not modelled in USFOS. The cables do not transfer significant moments.

The situation from Fig. 6.10 is compared with the ANSYS model shown in Fig. 6.11. The figure shows that the lines of action of the forces in this model do not pass through the same location. An additional moment is generated, caused by eccentricities between work lines of the forces. The moment is calculated by taking the sum of the moments around the same point as in the USFOS model, indicated as point A. The moments resulting from the blue forces are accounted for in the USFOS model, whereas the forces in red generate the additional moments. They are calculated

with Eq. (6.10) The outcome of the equation is compared to the difference between the moments in Table 6.3. It is concluded that they agree well. The difference between the bending moments for the two calculation methods is therefore attributed to the eccentricity of forces in the ANSYS model.

$$\sum M_A = F_z \cdot e_1 + F_{susp} \cdot e_2 \approx 90[kN] \cdot 2[m] + 170[kN] \cdot 1.2[m] = 384[kNm] \tag{6.10}$$

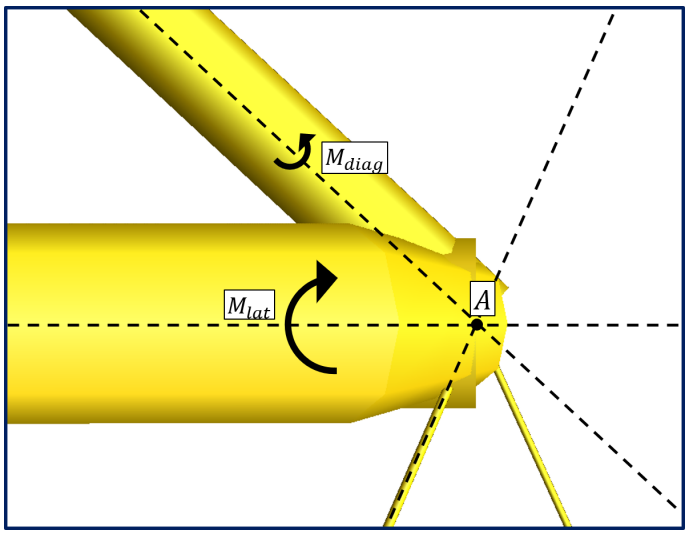

Figure 6.10: Connection as modelled in USFOS

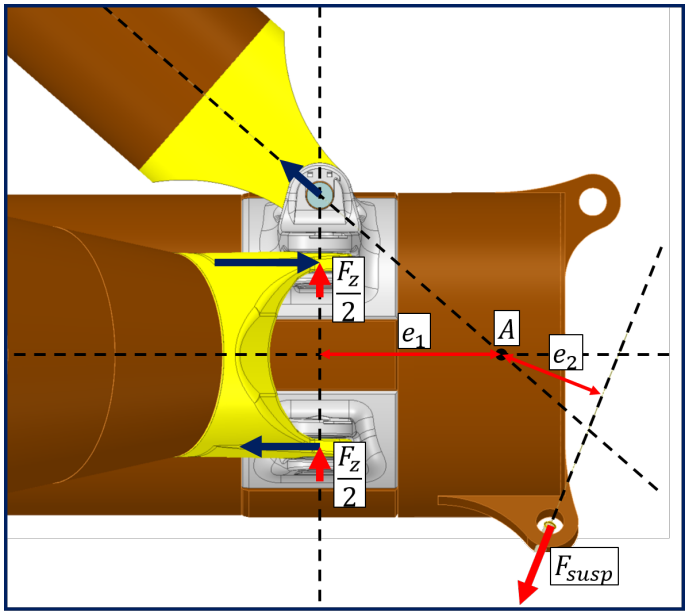

Figure 6.11: Real geometry of the connection

6.2 Conclusion

In this chapter, the hand calculated stress signal is compared with the stress signal derived from the FE analysis in ANSYS. The results of the comparisons in the previous sections are summarized in Table 6.4. At first sight, the signals seemed to agree very well. They are almost perfectly in-phase and there is only a small difference between the standard deviations of the signals. However, after

Table 6.4: Summary of the findings in this chapter

	Hand Calculation	FE analysis
SCF local bending	1.93	1.45
SCF ovalizing	-	1.08
SCF load concentration in welds	1.00	0.70
Reference force signal (ratio with hand calc)	1	± 2.5

a more detailed investigation, it is concluded that the small difference is coincidence.

The bending moments in the radial element, which are governing for the hotspot stress, are significantly different for the calculation methods. Part of the difference is compensated by the fact that the hand calculations use conservative assumptions for the local bending stress and the stress concentration in the welds. Consequently, the stress signals seem to agree very well. After comparing the reference signals however, it is concluded that the model in USFOS does not consider the eccentricity of two important loads. The accuracy of the models is discussed.

There are two differences between the USFOS model and the ANSYS model.

1. The moment in the diagonal member is considered in the equilibrium in USFOS, whereas it is zero in the ANSYS model. In reality the connection between the diagonal and radial member is a pin connection and does not transfer any moment. The calculated moment in USFOS therefore introduces a small error in the equilibrium calculation. It does not affect the results from the FE analysis.

2. The offset of the suspension line force is not considered in the USFOS model. This offset is a conscious design consideration. It aims to deform the radial member such, that the difference in rotation between the radial and lateral member is reduced. The moment transfer between these members is reduced accordingly. This effect is not considered in the USFOS model and the results should therefore be considered as conservative. Although the offset is present in the ANSYS model, the effect is not correctly modelled. The member reactions are modelled as imposed forces. Consequently, the offset creates an additional moment that *increases* the moment in the critical location in the weld between the casting and the radial member. However, the member reactions should have been modelled as imposed displacements. In this case, the additional moment would have resulted in a *decreased* moment in the critical location.

It is concluded that the results based on the FE analysis are derived from an incorrect model. They should not be used for the fatigue damage calculations. It is also concluded that hand calculations can in principle be used to approximate the hotspot stress in critical locations, for example for first design considerations. The conservative assumptions for the local bending stress and the stress concentration in the welds only will generally lead to conservative results. The fact that the offset of the suspension line force is not considered, makes the results even more conservative. Hence, the results can be used for fatigue damage calculations, but they are expected to underestimate the fatigue life of the location in the weld between the casting and the radial member.

Chapter 7

Results

This chapter presents the fatigue damage results, based on the stress signals of the potential critical locations. The fatigue damage is calculated according to the flow diagram in Fig. 7.1. This method is discussed and explained in Chapter 3.

This chapter starts with a discussion of the method that is used to calculate fatigue damage for sea states that have *not* been simulated in USFOS. Thereafter, the results for a single sea state are discussed. They are obtained for all the identified locations, shown in Fig. 7.6. The results for one sea state are used to select the most critical locations in the pin connection. In the next section, these locations are analyzed for all sea states in the wave scatter diagram, but first for only one wave direction. Finally, the results for all wave directions are combined and the results for all three connections are presented. For the calculations in this chapter, it is assumed that the structure is orientated as shown in Fig. 7.2. The definitions for wave directions and the numbers of the connections in this figure are used in the remainder of this chapter.

7.1 Method of calculation

In Chapter 3 it is discussed that not all sea states in the wave scatter diagram can be simulated in USFOS, due to a limited amount of time and computation capacity. It was proposed to divide the wave scatter diagram in blocks, that represent the sea states inside the block, in terms of fatigue damage. In this way, one simulation could represent multiple sea states, so that the number of simulations was greatly reduced. The flow diagram for this method is shown in Fig. 7.3.

At the end of the chapter, it is also explained that this method results in an underestimation of fatigue damages. This is caused by an incorrect assumption regarding the equivalent parameters of the representative sea state. This was realized only after all the simulations had be performed. The consequence of this mistake is that the equivalent sea state parameters are not representative for the block. The stress signal that is calculated from this sea state is therefore also not representative. Consequently, the obtained results can not be used directly for the fatigue damage calculations. An alternative method is therefore proposed.

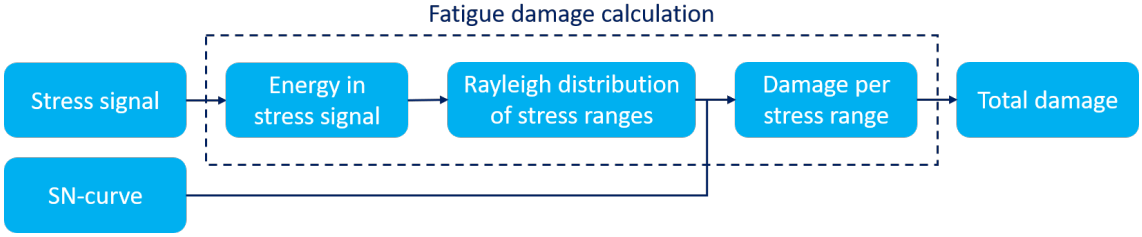

Figure 7.1: Flow diagram with the steps for the fatigue damage calculations

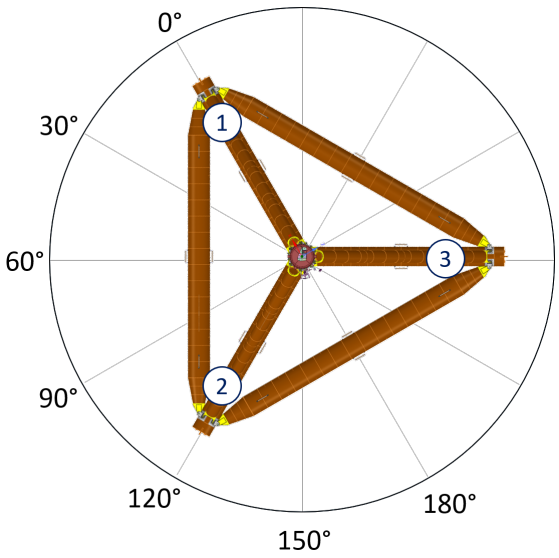

Figure 7.2: Definitions of the wave directions and the numbers of the pin connections

Figure 7.3: Original approach to reduce the number of simulations

7.1.1 Alternative method

Although the simulations cannot be used directly to calculate a representative stress signal, they can be used to determine the relationship between the sea state and the resulting stress signal. More specific, the significant wave height of the sea state is linked to the standard deviation of the resulting stress signal. The relationship can be used to determine the standard deviation for sea states that have not been simulated in USFOS. The method is explained below and shown in Fig. 7.4.

It is assumed that there is a linear relationship between the significant wave height of a sea state and the standard deviation of the stress signal that results from simulations and calculations. Recall that the damage depends on the standard deviation of a stress signal only. Hence, if it is shown that the relationship between significant wave height and standard deviation is linear, one simulation per block suffices to find the standard deviations (and damages) for the other sea states in the block. Note that with this method the actual stress signal is not calculated, but only its standard deviation.

This approach is only valid if it is shown that there is indeed a linear relation. This has been verified by performing four sets of simulations, ranging from $T_p = 9.0[s]$ to $T_p = 13[s]$, for the 0°wave direction. Note that this range of T_p-values represents the part of the scatter diagram that causes the most fatigue damage. Every set of simulations is based on a constant value of T_p. The significant wave height is varied to check the influence on the standard deviations. The results of the simulations are plotted in Fig. 7.5. They show that there is an almost perfect linear relation between the significant wave height and the standard deviation of the stress signal. They confirm that the proposed method can be used.

7.2 Single sea state

The first results that are calculated are for only one sea state (i.e. one entry in the wave scatter diagram in Fig. 7.7). The fatigue damage is calculated for all identified locations that are shown

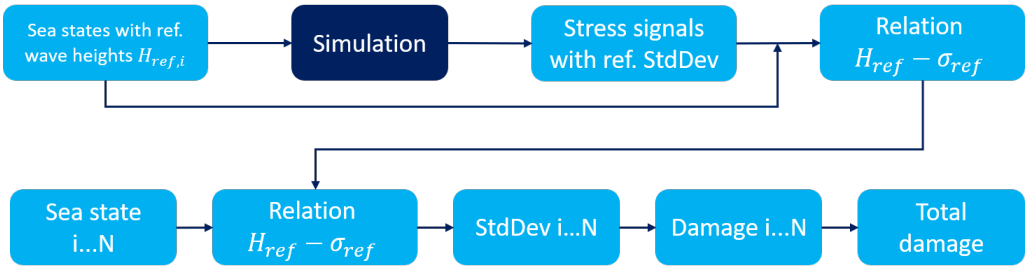

Figure 7.4: Alternative method for the calculation of the results

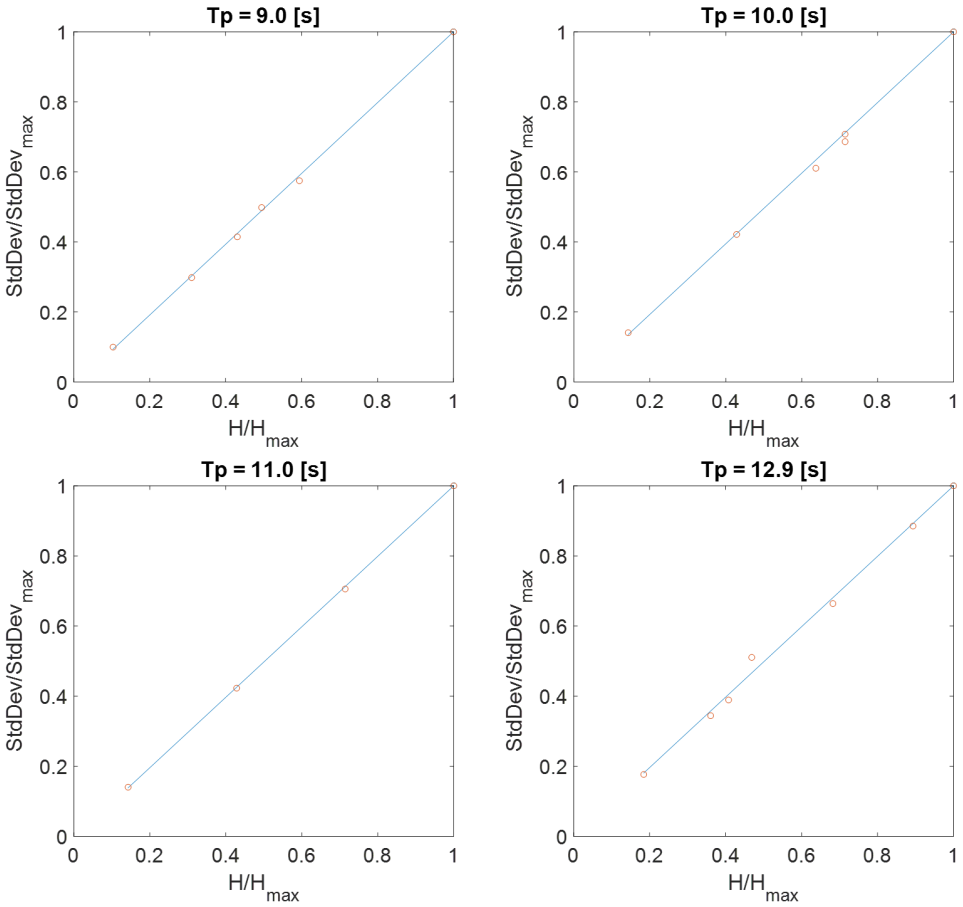

Figure 7.5: Linear relationships between significant wave height and standard deviation for the relevant T_p-values

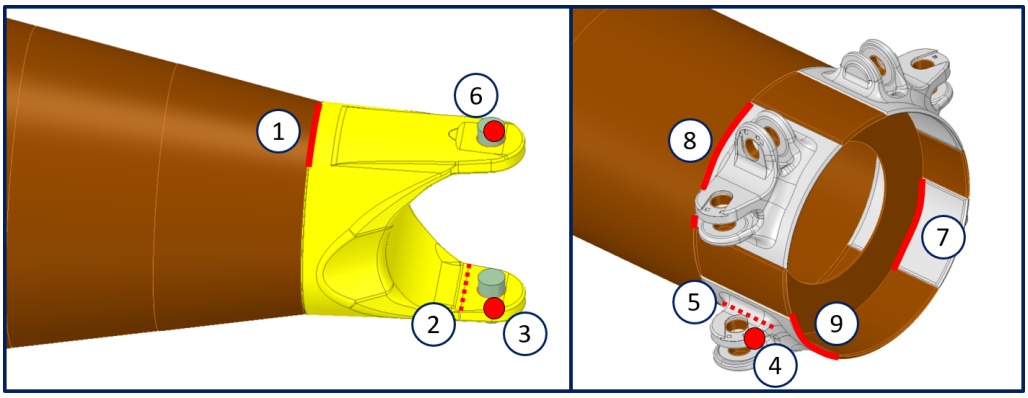

Figure 7.6: Identified locations that are potentially sensitive to fatigue damage

Table 7.1: Relative damage results for a single sea state

Critical location	Description	Relative damage
1	Element-casting weld (lateral)	0.16
2	Minimum cross-section ear	0.01
3	Ear hole	0.14
4	Fork hole	0.04
5	Minimum cross-section fork	0.02
6	Pin element	0.01
7	Ring stiffener weld	0.02
8.1	Element casting weld 1 (radial) - HC	1.00
8.2	Element casting weld 1 (radial) - FEA	1.95
9	Element casting weld 2 (radial)	0.01

in Fig. 7.6. This step aims to find the relative amount of fatigue damage for a single sea state, so that the most critical locations can be selected for further analysis. These locations are used to calculate the fatigue damage for the other sea states and wave directions in the next sections.

A random sea state for the 0°wave direction is selected for the calculation. It is not relevant which specific sea state is used, because the calculated damages are relevant. The results are the same for different sea states and the most critical location is the same in almost all cases. There are some exceptions, but they occur at sea states that have an insignificant contribution to the total accumulated fatigue damage.

The results of the calculations are shown in Table 7.1 and Fig. 7.8. The table shows that location (8) is the most critical location in the design. There are only two other locations where significant damage is accumulated, namely number (1) and (3) in Fig. 7.6. The damage in the other locations is negligible. It is also observed that the results of the two calculation methods that are used for location (8) are significantly different. This was expected, because the standard deviations of the signals are different, as found in Chapter 6. However, the results from the FE analysis are not considered, because they are calculated with an incorrect model, as discussed in Section 6.2. The results from the hand calculations are therefore considered for location (8) in the remainder of this chapter. The three locations with the highest relative damage are selected for more extensive damage calculations in the next sections. Note that the presented results are for a sea state of the 0°wave direction. The results for sea state of the other unique wave directions (30°and 180°) are similar and result in the same conclusion regarding the critical locations. These results can be found in Appendix D.

7.3 Single wave direction

The connection that was selected for the analysis in Section 4.1 is found three times in the design. The geometries of the connections are identical, but the directions of loading are different. The

Hs [m]	Tp [s]								Sum	Cum
	4.0	7.0	9.0	11.0	13.0	15.0	17.0	19.0		
0.50	8.72	9.15	6.21	3.20	1.44	0.61	0.26	0.18	29.8	29.8
1.50	5.27	12.22	11.50	6.70	3.04	1.20	0.44	0.24	40.6	70.4
2.50	0.73	4.05	5.81	3.98	1.80	0.65	0.20	0.08	17.3	87.7
3.50	0.06	0.95	2.45	2.17	1.02	0.33	0.09	0.02	7.1	94.8
4.50		0.16	0.90	1.18	0.62	0.19	0.04	0.01	3.1	97.9
5.50		0.02	0.24	0.55	0.36	0.11	0.02		1.3	99.2
6.50			0.04	0.20	0.20	0.06	0.01		0.5	99.7
7.50				0.06	0.09	0.04	0.01		0.2	99.9
8.50				0.01	0.04	0.02			0.1	100.0
9.50					0.01	0.01			0.0	100.0
10.50									0.0	100.0
11.50									0.0	100.0
12.50									0.0	100.0
13.50									0.0	100.0
14.50									0.0	100.0
Sum	14.8	26.6	27.2	18.0	8.6	3.2	1.1	0.5	100.0	
Cum	14.8	41.3	68.5	86.5	95.2	98.4	99.5	100.0		

Figure 7.7: Reduced wave scatter diagram

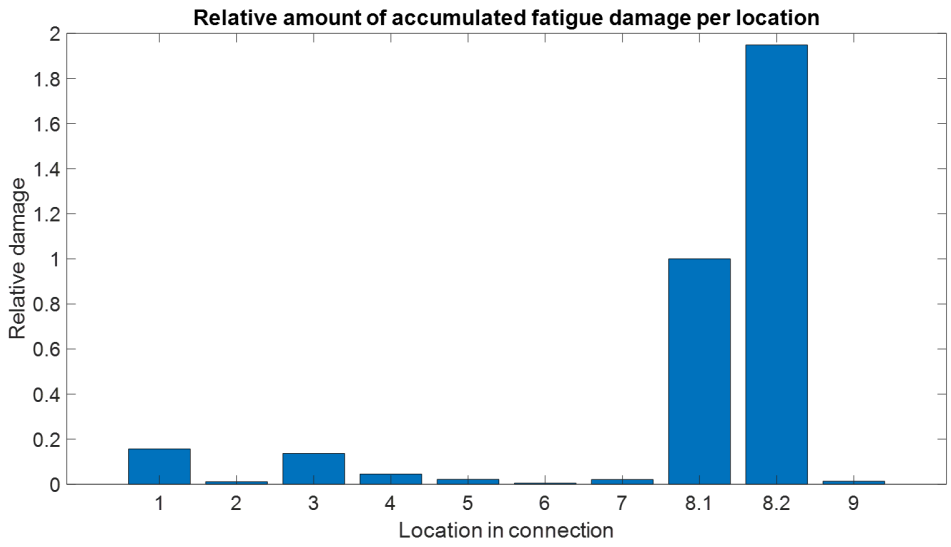

Figure 7.8: Relative damage results for a single sea state

Hs [m]	Tp [s]								Sum	Cum
	4.0	7.0	9.0	11.0	13.0	15.0	17.0	19.0		
0.50									0.0	0.0
1.50			0.03	0.02	0.01				0.1	0.1
2.50		0.02	0.19	0.18	0.09	0.01			0.5	0.6
3.50		0.03	0.44	0.53	0.29	0.03			1.3	1.9
4.50		0.01	0.56	1.00	0.61	0.05	0.01		2.2	4.1
5.50			0.40	1.22	0.92	0.08	0.01		2.6	6.7
6.50			0.15	0.96	1.03	0.11	0.01		2.3	9.0
7.50			0.03	0.49	0.87	0.12	0.01		1.5	10.5
8.50				0.16	0.55	0.12	0.01		0.8	11.4
9.50				0.03	0.24	0.10	0.01		0.4	11.7
10.50					0.07	0.06	0.01		0.1	11.9
11.50									0.0	11.9
12.50									0.0	11.9
13.50									0.0	11.9
14.50									0.0	11.9
Sum	0.0	0.1	1.8	4.6	4.7	0.7	0.1	0.0	11.9	
Cum	0.0	0.1	1.9	6.5	11.1	11.8	11.9	11.9		

Figure 7.9: Fatigue damage diagram with the yearly fatigue damage (in 10^{-3}) for each sea state

Table 7.2: Results for the most critical locations for the 0°wave direction

Location	Description	Yearly damage	Expected fatigue life [y]
1	Element-casting weld (lateral)	0.0030	333
3	Ear hole	0.0027	367
8	Element casting weld 1 (radial)	0.0119	84

connection that is expected to be the most critical (connection 1 in Fig. 7.2) is considered in this section. The other connections are addressed at the end of this chapter. The results for a single wave direction, which consists of the full wave scatter diagram, are presented. Recall that it is assumed that the scatter diagram is the same for all wave directions. The fatigue damage is obtained by combining the results of the individual sea states. The method explained in Section 7.1 is used to determine the results for sea states that are not simulated in USFOS. Note that at least one simulation is available for each block in the wave scatter diagram, because they were already done for the incorrect method. These simulations are used to derive the standard deviations of the other sea states in the block. The yearly accumulated damage for a sea state is calculated with the standard deviation and the probability of occurrence, derived from the scatter diagram in Fig. 7.7.

Results are calculated for the three critical locations, selected in the previous section. By plotting the yearly damage per sea state in a scatter diagram, a fatigue damage diagrams is obtained. Fatigue damage diagrams are derived for the three critical locations for the 0°wave direction. The wave scatter diagram in Fig. 7.7, which shows the probability of occurrence for the sea states, is thus translated into a fatigue damage diagram that shows the accumulated fatigue damage in a year. Fig. 7.9 shows the diagram for location (8) (refer to Appendix D for the fatigue damage diagrams of the other locations). If Fig. 7.7 and Fig. 7.9 are compared, it is observed that the center of probability is different from the center of fatigue damage. In fact, the largest part of the damage is caused by sea states that very rarely occur. It is therefore concluded that the fatigue damage is governed by high stress cycles with a relative low frequency of occurrence, rather than low stress cycles with a relative high frequency of occurrence.

The total fatigue damage per year is found by taking the sum over all the sea states. The expected fatigue life is calculated by taking the inverse of this value. The results are shown in Table 7.2 and Fig. 7.10, also for locations (1) and (3). Note that the expected fatigue life is for the 0°wave direction only. In other words, this would be the expected fatigue life if waves would come from this direction only, for the whole life of the structure. Results for all the wave directions are presented in the next section.

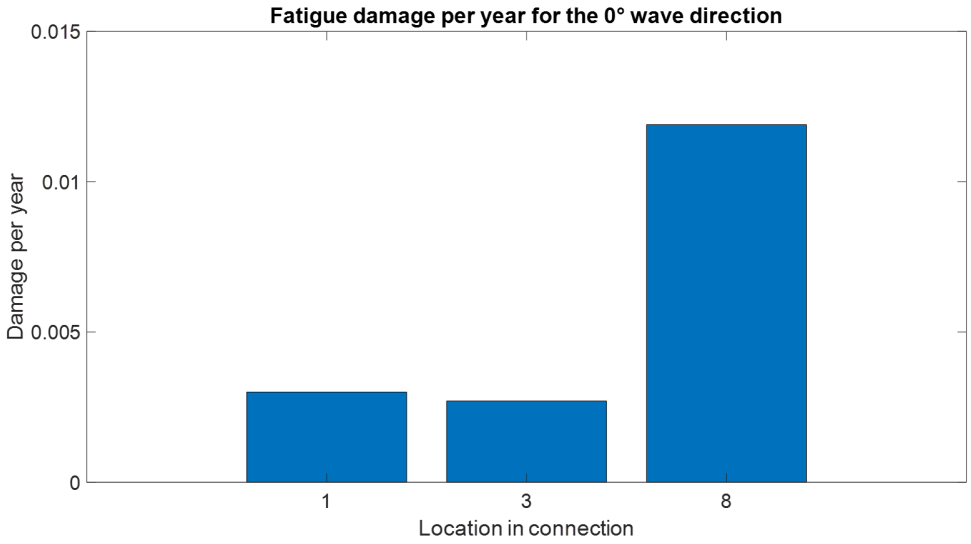

Figure 7.10: Results for the most critical locations for the 0°wave direction

Table 7.3: Probability of the wave directions

Wave direction [°]	Probability [%]
0	25.5
30	16.5
60	16.1
90	11.6
120	11.0
150	15.3
180	4.0

7.4 All wave directions

The results from the previous section are for the 0°wave direction only. In reality, waves come from multiple directions, as shown in the wave rose in Fig. 7.11. The figure shows that there are seven wave directions with a significant probability of occurrence (see also Table 7.3). Recall from Chapter 3 that there are only three unique wave directions. The other ones correspond to one of the unique directions. The fatigue damage for such a direction, is therefore determined by identifying the corresponding connection in another wave direction. For example, the results for the 60°wave direction for the connection indicated with 1 in Fig. 7.12, are equal to the results of the 180°wave direction from connection 2. In this way, results for the seven relevant wave directions are determined.

The fatigue damage results are calculated for all the directions, in the same way as for the 0°wave direction. It is assumed that the wave scatter diagram is equal for all wave directions. The damage per year for a single wave direction is calculated first, assuming that the structure is only loaded from that direction. The actual accumulated damage is found by multiplying this value with the probability of the considered wave direction. The total damage, for all wave directions, is obtained by summing these values. The results are shown in Table 7.4 for the three most critical locations in connection 1. The results for the other connections are presented in the next section.

The results from the Table 7.2 and Table 7.4 are summarized in Table 7.5. It is observed that the expected lifetime of locations (1) and (3) is significantly reduced if all wave directions are considered. This means that the 0°wave direction is more favorable than the other wave directions for these locations. The results of location (8) show an opposite trend. The expected life time increases if all wave directions are considered. It is concluded that for this location the 0°wave direction is less favorable than other wave directions. These observations are supported by Fig. 7.13. This figure shows that location (8) is more sensitive to symmetrical wave directions, whereas location

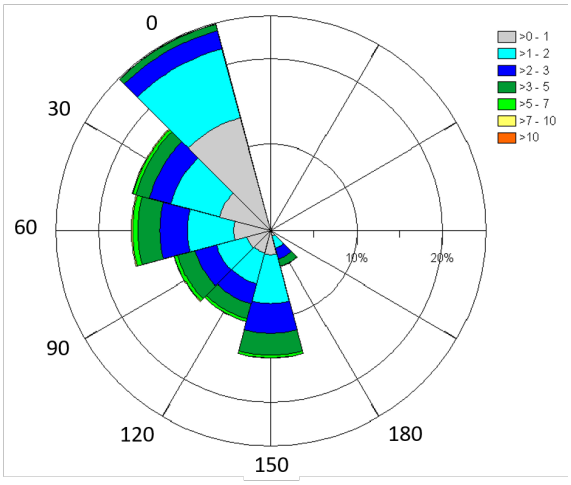

Figure 7.11: Directional spread of the waves

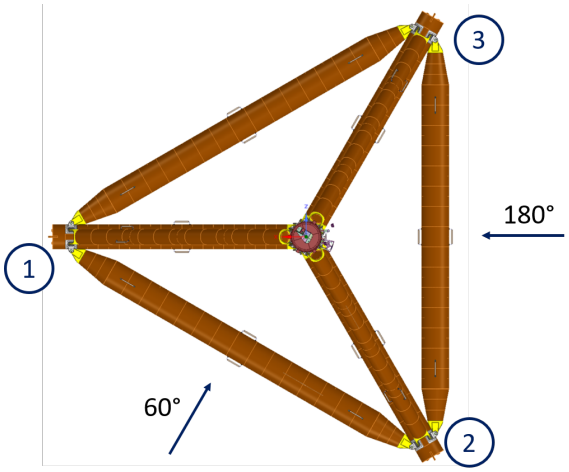

Figure 7.12: The symmetrical geometry is used, so that simulations are limited to only 3 unique wave directions

Table 7.4: Combined results for the critical locations for all wave directions

Location	Description	Damage [1/y]	Expected lifetime [y]
1	Element-casting weld (lateral)	0.0092	109
3	Ear hole	0.0084	119
8	Element-casting weld (radial)	0.0085	118

Table 7.5: Comparison between the results for all the wave directions and the 0°direction only

Location	Description	Expected lifetime [y] 0°	Expected lifetime [y] all directions
1	Element-casting weld (lateral)	333	109
3	Ear hole	367	119
8	Element-casting weld (radial)	84	118

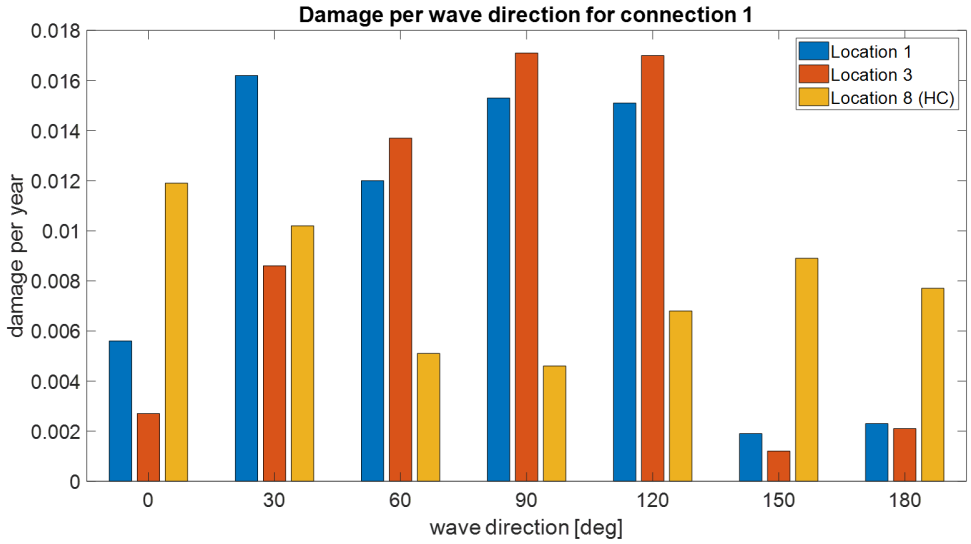

Figure 7.13: Yearly accumulated damage per wave direction for connection 1

(1) and (3) are more sensitive to oblique wave directions.

7.4.1 All Connections

The results that are presented up to this point are for one connection only (number 1 in Fig. 7.2). This is expected to be the critical connection, but this is verified by checking results for the other connections. The same approach is followed (using the symmetry in the structure) to obtain results for all wave directions. Note that the only difference between the connections is that the probability of the loading directions is different. For example, connection (1) is mainly loaded from the 0°wave direction. But, connection (3) experiences 0°wave as 120°waves (if compared to connection (1)). The expected fatigue lifetimes considering all directions for all three pin connections are shown in Table 7.6 and Fig. 7.15.

Table 7.6: Expected fatigue life times, considering all wave directions, for the critical locations in all three connections.

	Expected lifetime [y]		
Location	Connection 1	Connection 2	Connection 3
1	109	74	108
3	119	80	100
8	118	132	140

7.5 Conclusions

The results of the fatigue damage calculations are presented in this chapter. A method is discussed, that is used to calculate the standard deviations of stress signals of sea states that are not simulated in USFOS. The relationship between the significant wave height of a sea state and

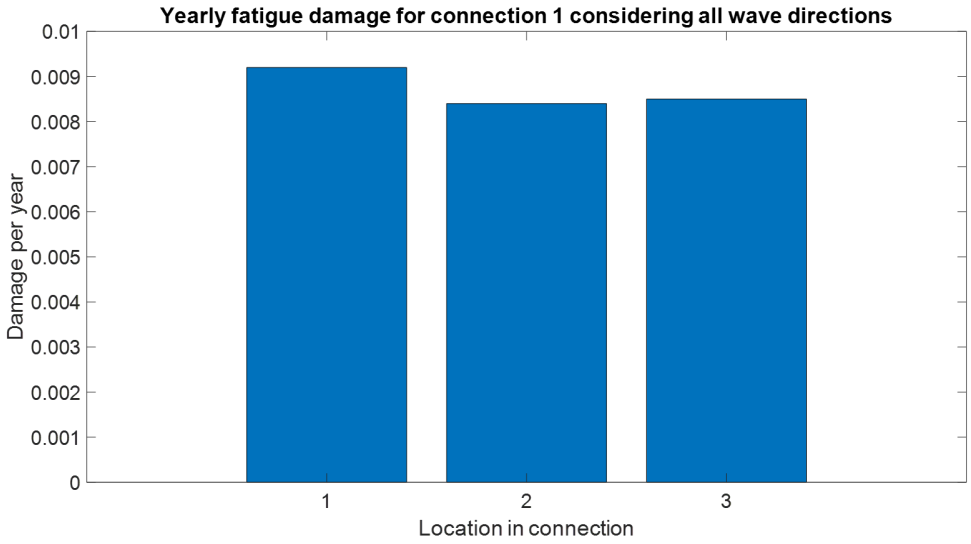

Figure 7.14: Yearly fatigue damage considering all wave directions

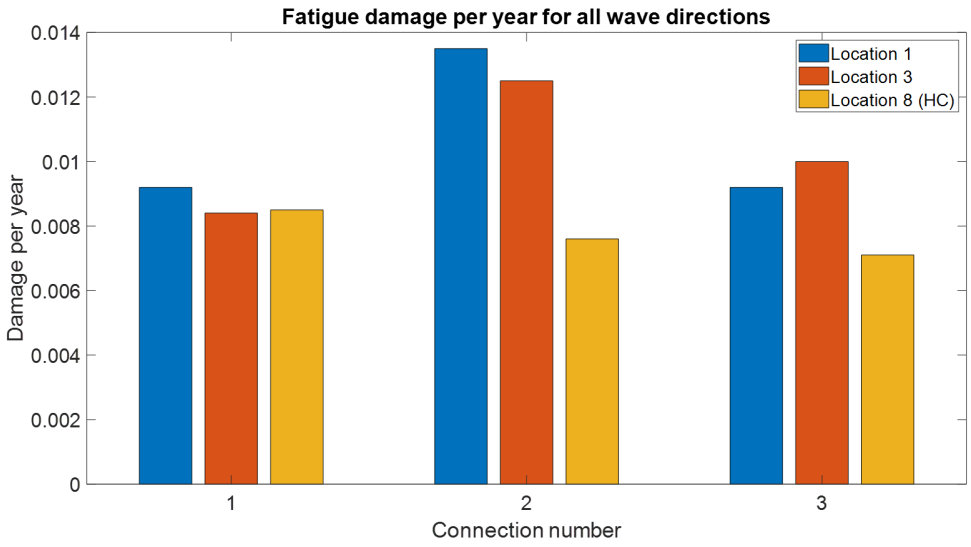

Figure 7.15: Expected damage per year for the critical locations in all three connections

the standard deviation of the resulting stress signal is linear. Hence, the simulations from USFOS that were based on incorrect equivalent parameters could still be used to calculate the standard deviations of the sea states that are not simulated. In this way, fatigue damage could be calculated for the full wave scatter diagram.

The first fatigue damage calculations were done for a single sea state only. The goal was to find the most critical locations from the list of identified locations from Chapter 4. The results showed that there are only three locations that are sensitive to fatigue. The other locations showed insignificant fatigue damages.

The three critical locations were selected for further investigation. In the second step, the fatigue damage for a single wave direction was determined, considering the full wave scatter diagram. A fatigue damage diagram was obtained, which shows the yearly accumulated fatigue damage for every sea state. From this diagram, it is observed that the center of fatigue damage is different from the center of probability. Hence, it is concluded that fatigue damage is governed by large stress cycles with a relatively low probability of occurrence, rather than small stress cycles with a high probability of occurrence. The results for the 0°wave direction only, also showed that location

(8) is expected to be most critical. The other locations show considerable fatigue damage, but this are expected not to be critical (for this wave direction).

The next step consisted of combining the results of all relevant wave directions. It is concluded that the other wave directions have different effects on the critical locations. For location (8), the expected fatigue life increased if all directions were considered, rather than only the 0°wave direction. Locations (1) and (3) showed opposite results. For these locations, the expected fatigue life time decreased significantly and approached a critical value. It is concluded that location (8) is sensitive to wave directions that result in (near) symmetrical loading. Oblique wave directions are more favorable for this location. In contrary, locations (1) and (3) are sensitive to wave directions that result in non-symmetrical loading. From these calculations it is concluded that location (1) and (3) are more critical than location (8) if all wave directions are considered

In the last section, all three pin connections were included in the calculations and results were compared. It is concluded that there are seven locations with an expected life time of less than 120 years, which is twice the required design life time according to the standard for floating wind turbine structures [24]. These locations are listed in Table 7.7. It is concluded that the locations (1) and (3) are expected to be critical in all three the connections. Location (8) is expected to be critical in connection (1) only, because this connection is mainly loaded in an unfavourable direction for this location.

Table 7.7: Critical locations with an expected fatigue lifetime of less than 120 years

Pin connection	Location	Expected lifetime [y]
1	1	109
	3	119
	8	118
2	1	74
	3	80
3	1	108
	3	100

Chapter 8

Discussion of results

In the research that is presented in this thesis, the fatigue strength of the pin connection is assessed. A method is developed, in which the complex phenomenon of fatigue is analyzed in some well-defined steps. In every step assumptions are made and models are developed that are representative for the physics involved. This is unique for a complex geometry like the pin connection. Other analyses [11, 16] avoid the complexity of the problem, by making very strong assumptions with regards to load cases or geometry. This makes it difficult to assess the validity of the applied method and the reliability of the results.

The method in this research does not necessarily produce more accurate results. However, it does provide insight into the factors that are relevant for fatigue in the pin connection. This makes it easier to identify factors that could reduce the fatigue damage or improve the fatigue strength. In general, it provides a complete and transparent method to analyze fatigue, of which the applicability is not limited to the situation discussed in this thesis.

Other applications for the TetraSpar concept could include different geographical locations or a larger (scale-up) version of the concept. The internal forces should then be calculated again, with updated input for the USFOS model. The USFOS model can be used to find new internal force signals and the same method of analysis can be used to find the corresponding fatigue damage.

Other applications could also include a whole different geometry with a pin connection. An example could be a tubular connection in a jacket structure. Such connections are currently fully welded connections. If the fatigue strength of the pin connection can be proven for commercial use, they might be an alternative for a welded connection. Internal force signals should then be generated for the specific situation, but the approach for the fatigue analysis remains the same. The identification of potential critical locations, the stress estimations and the fatigue damage calculations could be done in a similar way, using the developed tools in MATLAB.

8.1 Sensitivity

From the results in Chapter 7 it is derived that expected fatigue lives range from several tens of years to thousands of years. No specific sensitivity study on the results is carried out for this project. However, it should be clear that fatigue calculations are very sensitive to the input. It is of utmost importance to be aware of the sensitivity of the results, before either the method, or the results are used for any application. The results are specifically sensitive to the magnitude of the variations of the hotspot stresses, and hence also to the the calculation of these stresses. The factors for which there is uncertainty about (the accuracy of) the used values are listed. It is recommended to assess these factors before the results are used. The accuracy of the results can be improved if more research on these factors is done. The most important factors that can have a direct and significant effect on the results are:

- The internal force signals form the basis for the stress calculations. The most important factors that determine the magnitudes of the internal forces are the external loads on the

structure and the distribution of the forces over the connections. The external loads are expected to be relatively accurate, because commonly used and proven methods are used for the calculations. The distribution of the internal reactions on the pin connections is manually determined and could be significantly different.

- The stress concentration factors directly influence the magnitude of the hotspot stress. It is difficult to assess the accuracy of the values that are used. Most of the SCFs are derived from experimental research and are believed to be accurate. Nevertheless it should be remembered that the effect of only small inaccuracies is amplified in fatigue.
- The SN-curves define the maximum number of allowable stress cycles. The choice of SN-curve, which depends on the detail, can have a direct and significant effect on the calculated fatigue damage. The appropriate SN-curves for the identified locations are selected by finding a corresponding standard detail in [23].

8.2 Limitations

In order to model the complex situation such that it could be solved with the available resources, many simplifications and assumptions have been made. Hence, there are several limitations to the results and approach from this research. They are discussed below.

Wind loads

One of the main limitations of this project is that wind loads are not considered. This could have a large influence on the results, and on the validity of assumptions and models that are used for the approach. It is difficult to predict whether wind loads have a positive or negative effect on fatigue in the identified locations. In [13] a study is performed in which the effect of wind loads on the dynamics of a floating wind turbine is analyzed. It is concluded that aerodynamic damping can significantly reduce floater motions if wind and waves are aligned. This is confirmed in the DNV standard for floating wind turbine structures [24]. However, it is emphasized that combined wind and wave loading lead to complex situations, in which aerodynamic damping *can* play an important role. The complexity of this phenomenon is reflected by the following statements from [24]. The effect of the aerodynamic damping:

- Is highly dependent on the wind-wave alignment
- Is only significant for certain platform motions
- Depends on the motion frequency

Including wind loads might result in more positive fatigue results if aerodynamic damping is significant. However, it could also have a negative impact on the presented method, specifically on assumptions or approximations that are made. The wind loads are likely to produce more complex (irregular) stress signals, which could for example affect the validity of the Rayleigh approximation. In that case, Rainflow counting could be used as an alternative, which requires the reference force signals to be longer in order to be statistically reliable. This has a large impact on the computation time in USFOS.

Linearity

Several steps in the analysis are based on linear relationships that are derived for this specific combination of environment and geometry. This might be different for other situations or applications. An example of this is the relationship between the significant wave height and the standard deviation of the stress signal. This relationship is shown to be linear in the current situation but might be non-linear in another case. Linearity is attributed to the fact that the inertia term in the Morison equation (Eq. (3.5)) is dominant. The dominance of this term depends on the diameter of the members and the characteristics of the waves. For more slender structures, or different wave characteristic, the drag term could be more significant, and non-linear effects could come into play. The linear relationship is in such a case not valid anymore.

Models

Other limitations are a consequence of the models that are used. In the USFOS model, the pin connections are not modelled. Instead, the members are rigidly connected and forces/moments are transferred in all degrees of freedom. The internal forces are obtained at the member ends (in the plane of the pin axis and the member), and the forces in the pin connections are manually determined with static equilibrium equations. The pin connections generate a moment release around the vertical axis through the pins. However, the rigid connections in USFOS generate moments in this direction. For the connections in the lateral member, these moments have no significant effect and they can be ignored. However, the moment in the diagonal member influences the equilibrium assumptions and it introduces a small error.

The main limitation is found in the modelling of the member reactions from the lateral member in the ANSYS FE model. At the end of Chapter 6 it was explained that there is an additional bending moment in the ANSYS model, that is not considered in the USFOS model. This moment increases the moment acting on the critical location between the casting and the radial member. In reality, the member reactions from the lateral member should have been modelled as imposed displacements on the pin connection, whereas in the current model the reaction forces are modelled. If the member reactions are modelled as imposed displacements, the offset of the suspension line force will decrease instead of increase the moment acting on the weld between the casting and the radial member.

In conclusion, the FE analysis in ANSYS should be redone in order to find more accurate hotspot stress levels. The member reactions from the lateral member should be modelled as imposed displacements, instead of imposed forces. Moreover, if the results from the USFOS model are directly used (as was done for the hand calculations), the predicted fatigue lives will be conservative.

Environmental conditions

Environmental data that is used in this project is derived for the test site, so that the results are valid for this location only. The performance of the TetraSpar could be assessed at other locations as well, but site-specific data is required. However, it is commonly known that the environmental conditions at the North Sea are harsh, especially offshore Norway. From the fatigue damage diagrams, that are found in Chapter 7, it is concluded that significant damage occurs mostly at rough sea states. For other locations a revised estimation of the fatigue results can be made, based on the environmental conditions of the location of interest. An example of this could be a location in the Southern North Sea, for example offshore UK. Weather conditions are expected to be less severe, so that the fatigue life is expected to be higher than at the considered location. In contrary, the weather conditions offshore Japan are known for severe storms. In this environment, the TetraSpar is expected to have a lower fatigue life and improvements to the design might be necessary before it can be installed here. In conclusions, the results are limited to the test location offshore Norway, but a qualitative estimation of the results can be made based on environmental data.

Another (potential) limitation, regarding the environmental data is the fact that it is based on hindcast data. An implicit assumption that is made when hindcast data is used to predict lifetimes, is that the conditions remain constant. This is not necessarily the case for the future. Climate change is expected to have consequences for environmental conditions, especially in regions with extreme weather. The predicted lifetimes are therefore only valid for the data from the past and might not be applicable to the future.

Other locations

Expected fatigue lifetimes are calculated only for nine potential critical locations. They are identified based on engineering understanding, but they may be not the only critical locations. Hence, the results only apply to the identified locations and not to the whole pin connection, nor the complete structure. Though, the connection is thoroughly analyzed, and it is suspected that there are no locations that are more critical. For the full structure however, there are other zones that

experience large stress ranges and they might therefore be sensitive to fatigue as well. Examples are the pad eyes to which the suspension lines are connected, the interface between the wind turbine and the floater and the connection points between the members in the keel. The present research however is limited to the pin connections.

Chapter 9

Conclusions & recommendations

In the research project that was carried out for this thesis, the fatigue strength of the pin connection in the TetraSpar has been assessed. Environmental data (in the form of a wave scatter diagram) of the location where a prototype of the concept will be tested, has been used. Fatigue, resulting from wave actions only, has been evaluated. Non-linear time domain simulations were performed using the FE software package USFOS. The time series of the internal forces in specific members of interest formed the input for the stress calculations. Static equilibrium equations were used to combine the force time series and obtain time series of the hotspot stresses of relevant critical locations. Nine potential critical locations in the pin connection were identified. For eight locations stresses were calculated with elementary stress equations, based on equilibrium considerations. The ninth location was more complex and was therefore analyzed using the FE software package ANSYS. The fatigue damage at each location was calculated, based on time series of the hotspot stresses, by applying the Palmgren-Miner rule. For the response analysis of the many sea-states of the scatter diagram, the Rayleigh approximation for the distribution of stress ranges and SN-curves recommended in [23] were used. The predicted minimum fatigue lives for the three most critical locations in the connection are provided below.

Location	Description	Predicted fatigue life [y]
1	Element-casting weld (lateral)	74
3	Spots next to hole in ear (lateral)	80
8	Element-casting weld (radial)	118

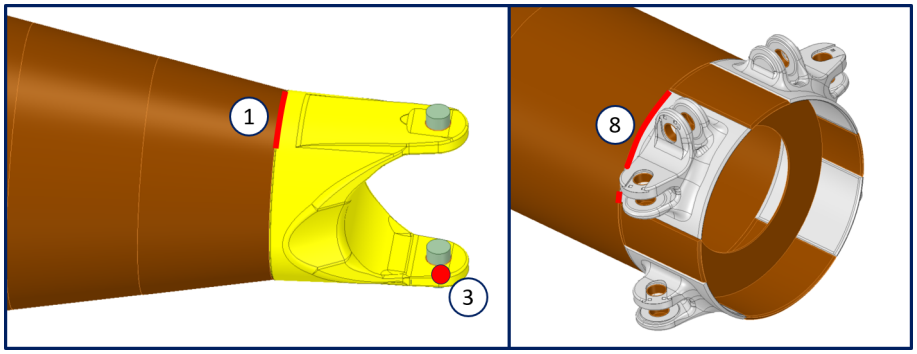

Several conclusions can be drawn from this research. The objectives of the project as defined in Chapter 1 are achieved, and the findings are shortly summarized. Conclusions are also formulated with regards to the fatigue damage results. Although they should be interpreted with care as explained in the discussion of the results (Chapter 8). Also note that the conclusions on the results are only valid for the considered geographical location. Finally, conclusions about the process are presented.

Objectives

- The connection is decomposed in its components. It is concluded that the components are in general loaded by only one or two significant loads, resulting in non-complex stress mechanisms. Only the welds between the castings and the radial member result in more complex stress mechanisms. The stress levels in these locations have therefore been analyzed with FE software.

- Nine potential critical locations are identified, based on literature and engineering knowledge. These are the identified locations, but not necessarily the only fatigue sensitive locations in the pin connection. Hotspot tresses are estimated in the identified locations. The variation of the stress levels is of main interest, because this is governing for the fatigue damage.

- Only three of the nine locations are critical. These are the hole next to the ear, the weld between casting and radial and the weld in the lateral member, close to the ear. The fatigue damage is calculated based on the recommendations in [23]. It is concluded that the fatigue life can be estimated, but that by nature of the SN curve, it is very sensitive to input.

Results

- From the nine identified locations, only three are sensitive to fatigue. The other six locations accumulate negligible fatigue damage and are therefore not critical. Two of the nine locations have an expected fatigue life shorter than 100 years. These locations are the weld between the casting and the element in the lateral member and the spots next to the hole in the lower ear. Their respective minimum fatigue life times are 74 and 80 years. The third critical locations, the weld between the upper casting and the radial member, has a minimum fatigue life of 118 years.

- For a typical operational life of 20 years of an offshore wind turbine, the fatigue damage after 20 years is expected to be around 25% of the maximum damage in the most critical location.

- The design fatigue factor (DFF) for fatigue strength in floating offshore wind turbine foundations, is equal to three [24], assuming that no inspection or maintenance is done. Consequently, the required lifetime of the structure is increased to 60 years. If this factor is included, the minimum fatigue strength of the pin connections of 74 years is *still sufficient* for a lifetime of 20 years. It is therefore also concluded that the current design does meet the standard for floating wind turbine structures, as defined by DNV in [24], according to the present calculations.

- Fatigue damage is mainly caused by rough sea states. Significant damage is accumulated at sea state with a significant wave height of at least 3.5 [m].

- The three most critical locations are sensitive to different load directions. The critical locations in the lateral member are sensitive to oblique wave directions, which result in asymmetrical loading. The most critical location in the radial member is sensitive to load directions that result symmetrical loading.

- For the testing period of the full-scale prototype, which will take 2-5 years, no significant fatigue damage is expected to occur in the assessed locations in the pin connections.

Analysis process

- In current modern times, FE software is likely to be used to solve complex situations like the pin connection. However, this research has shown that hand calculations can be of significant value in addition to FE software. They have shown to be an effective tool to estimate stress levels and it is concluded that they are of additional value. They provide in-depth insight into load paths, significance of loads and stress mechanisms, which results in a better understanding of the details in the connection. Moreover, hand calculations help to interpret results that are generated in an FE analysis, and to judge whether they are plausible. From this research it is also concluded that observed stress patterns from FE results can be coupled to the factors in the analytical expressions for stress distributions.

- Fatigue of the pin connection is analyzed with a well-defined approach. Environmental conditions are systematically translated to hotspot stresses, with which fatigue damage can be calculated. This allows for improvement of assumptions and models and creates an overall transparent view on the relevant factors for fatigue. The used approach could be applied to other situations as well. Alternative applications could include a different geographical location, a scale-up version of the TetraSpar concept, or a different geometry with a pin connection.

- Fatigue damage results are very sensitive to the variation of the hotspot stress signal, and the choice for the SN-curve. Consequently, the input for the stress calculation has a large effect on the fatigue damage as well. The input includes any step prior to the stress calculation in the general flow diagram (Chapter 3).

- From the comparison between the hand calculations and the results of the FE analysis, it is concluded that hand calculations give a relatively accurate estimation of hotspot stress levels. In general, conservative assumptions are made that result in an overestimation stress levels. However, it is also concluded that close attention should be paid to models that are used, especially with regards to geometry and force transfer in connections.

- The FE analysis in ANSYS was performed by applying imposed forces to the model. Instead of imposed forces, imposed displacements should have been applied to the model. The results from the FE analysis are therefore considered as inaccurate. If the results from the hand calculations are used (which are based on the USFOS results), without correction of the additional bending moment, the predicted fatigue lives will be conservative.

- It is concluded that the pin connection is expected to be feasible for a floating structure with regards to fatigue. The current results are valid for the test site location, which is offshore Norway. The environmental conditions here are relatively severe, but the fatigue strength is expected to be sufficient. Hence, the pin connection might be suitable for other geographical locations. Furthermore, it could also be used for other applications. An example could be the (currently fully welded) tubular connections in jacket structures. Application of the pin connection could potentially result in huge cost savings, compared to a welded connection.

Recommendations

From the findings in this research, and the conclusions presented in this chapter, several recommendations are formulated. They are divided in two sections. The first recommendations are for further work, or to improve the accuracy of the results from this research project. The second set of recommendations are specifically for the TetraSpar project team.

Further work

- In the USFOS FE analysis, an additional bending moment (caused by the offset of the suspension line force) was not modelled. It is recommended to remodel the USFOS model to reflect the hinge connections and the offsets of the suspension line. This removes one of the main approximations in the present analysis strategy.

- The ANSYS FE analysis should be redone with imposed displacements obtained from the USFOS model, instead of imposed forces.

- It is recommended to investigate the effect of wind loads. If it is found that they have a positive effect on the fatigue damage in the pin connections, the results from this research can be interpreted as conservative results. The life time of the pin connection is not expected to be critical for a life time of 20 years in that case. If it is found that the effect might be negative, it is advised to do a fully coupled wind/wave analysis in a dedicated software package. From the analysis, internal force signals could be used to assess the fatigue damage with the developed tools for this research. Internal force signals should be updated, such that the effect of wind loads is included.

- For fatigue assessment, a method is used as recommended by the recommended practice of DNV [23]. This method is very sensitive to input, and there any many factors that could significantly influence the results. It should therefore be considered to either validate the input for the fatigue damage calculations - i.e. the force signals that form the basis for the stress signals - or to validate the results with a whole different method of fatigue analysis.
- It is recommended to estimate fatigue damage in potential critical zones, other than the pin connections. Other zones are also expected to experience large stress ranges, such as the connection points of the suspension lines, the connections between the members of the keel and the interface between the wind turbine and the floater. A first estimation could be made with simplified methods, to find the order of magnitude of the fatigue damage. This could be compared with the results of the pin connection to assess whether these zones are critical.
- It should be considered to investigate the effects of climate change on the environmental conditions if the TetraSpar would be installed commercially. From the fatigue damage diagram (Fig. 7.9 in Chapter 7), it is concluded that most of the fatigue damage is caused by harsh weather conditions. Possible effects of climate change might be more frequent occurrences of such events. It is recommended to investigate the potential negative effect on the fatigue damage.

TetraSpar project team

For the TetraSpar project team, the recommendations are mainly focused on verification of the estimated stresses and fatigue in this research project. This is achieved by finding relations between predicted data and real-life measurements. Other recommendations concern measures to reduce the fatigue damage or to improve the fatigue strength in the details.

- Install accelerometers at the base of the column of the prototype that will be tested. Obtained data can be translated to displacements and accelerations, so that the numerical simulations by USFOS models can be evaluated.
- Install strain gauges at the critical locations in the prototype that will be tested. Obtained data should be translated to stress levels, so that the measurements can be compared to the estimated stresses in the identified locations.
- It is also recommended to relate the measurements to the weather conditions at site. With this relationship the accuracy of the USFOS simulations can be assessed. Also, it can be verified whether the assumption for a linear relationship between significant wave height and standard deviation of the stress signal is valid.
- It should be considered to analyze the force transfer through the pin connections, preferably with a dedicated software package such as ANSYS. In Chapter 8 it is discussed that the distribution of forces over the connections might not be accurate, and that possible errors significantly impact the results
- It is strongly recommended to perform an intensive quality control during the fabrication process of the critical pin connections. Small defects or imperfections, might result in premature initiation of fatigue cracks, resulting in a reduced fatigue life. Specifically, the welds at the most critical location should be of optimal quality and it is recommended to post-process them after the welding process.
- Finally, it is also strongly recommended to make a robust plan on how fatigue in the prototype is going to be analyzed. It is believed that a good understanding of the relationship between real life measurements and the estimated stresses in this research enables a huge potential. It would mean that stresses and fatigue in complex geometries can be assessed with relatively simple equations. Much time could be saved for the first design considerations, because geometries could be optimized in an early stadium.

Bibliography

[1] A. Almar-Naess. *Fatigue Handbook, offshore steel structures*. Tapir, Trondheim, 1985.

[2] J. Bauer. *Foundations for Offshore Wind Turbines*. 2013. URL: https://www.nrel.gov.

[3] A. Chang. "Wave-scatter lumping strategies for fatigue damage assessment". 2014.

[4] F.M. Dekking. *A Modern Introduction in Probability and Statistics*. Springer, 2005.

[5] United Nations Population Division. *The 2019 Revision of World Population Prospects*. 2019. URL: https://www.populations.un.org.

[6] LLC Engineers Edge. *Fatigue Strength (Mechanics) of Materials*. 2005. URL: https://www.engineersedge.com.

[7] M. Frocht. "Stress concentration factors around a central circular hole in a plate loaded through a pin in the hole". In: *Journal of Applied Mechanics* (1940).

[8] Siemens Gamesa. *Siemens Gamesa Wind Turbine SG-3-4-132 Brochure*. 2019. URL: https://www.siemensgamesa.com.

[9] R.C. Hibbeler. *Mechanics of Materials, ninth edition*. Pearson Prentice Hall, 2014.

[10] L.H. Holthuijsen. *Waves in Oceanic and Coastal waters*. Cambridge University Press, 2007.

[11] M. Walkusch Jensen. *Strength Verification Procedure for the TetraSpar Demo Project*. 2019.

[12] J.M. Jonkman. *Dynamics Modeling and Loads Analysis of an Offshore Floating Wind Turbine*. 2007.

[13] X. Liu. "Effect of Aerodynamic Damping on the Tower Load of Offshore Horizontal Axis Wind Turbines". In: *Elsevier* (2017).

[14] E. Nygaard. *HYWIND Metocean Design Basis*. 2008.

[15] W.D. Pilkey. *Peterson's Stress Concentration Factors*. John Wiley & Sons, INC., 1997.

[16] PRINCIPIA. *Detailed Integrated Load Analysis for the TetraSpar Demonstration Project*. 2019.

[17] PRINCIPIA. *Fully Coupled Integrated Load Analysis*. 2018.

[18] R. Putz. *Statistical analysis of wave records*. University of California, 1953.

[19] J. Schijve. *Fatigue of Structures and Materials*. Springer, 2009.

[20] H. Stiesdal. *Industrialized Offshore Wind Turbine Foundations*. 2019. URL: https://www.stiesdal.com/material/2019/02/Stiesdal-Tetra-01.02.19.

[21] P. Stoica. *Spectral Analysis of Signals*. Prentice Hall, 2005.

[22] A.H. Techet. *Hydrodynamics & Potential Flow Theory*. 2005.

[23] Det Norske Veritas. *Fatigue Design of Offshore Steel Structures*. 2014.

[24] Det Norske Veritas. *Floating Wind Turbine Structures*. 2018.

Appendices

Appendix A

SCF diagrams

In this appendix SCF diagrams are shown, which have been used to estimate SCFs. These SCFs have been used for the hand calculated stresses. The diagrams are derived from [15].

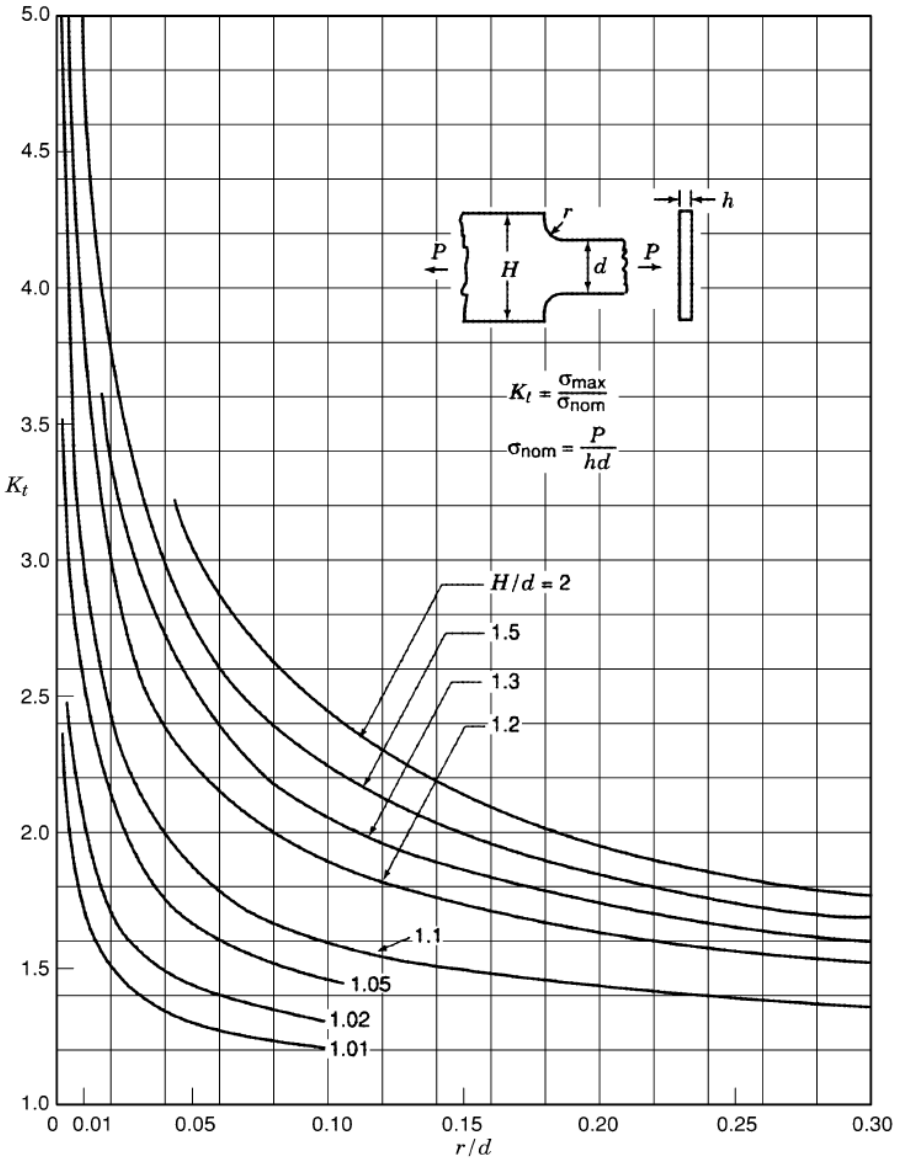

Figure A.1: SCF diagram for a component with a thickness change

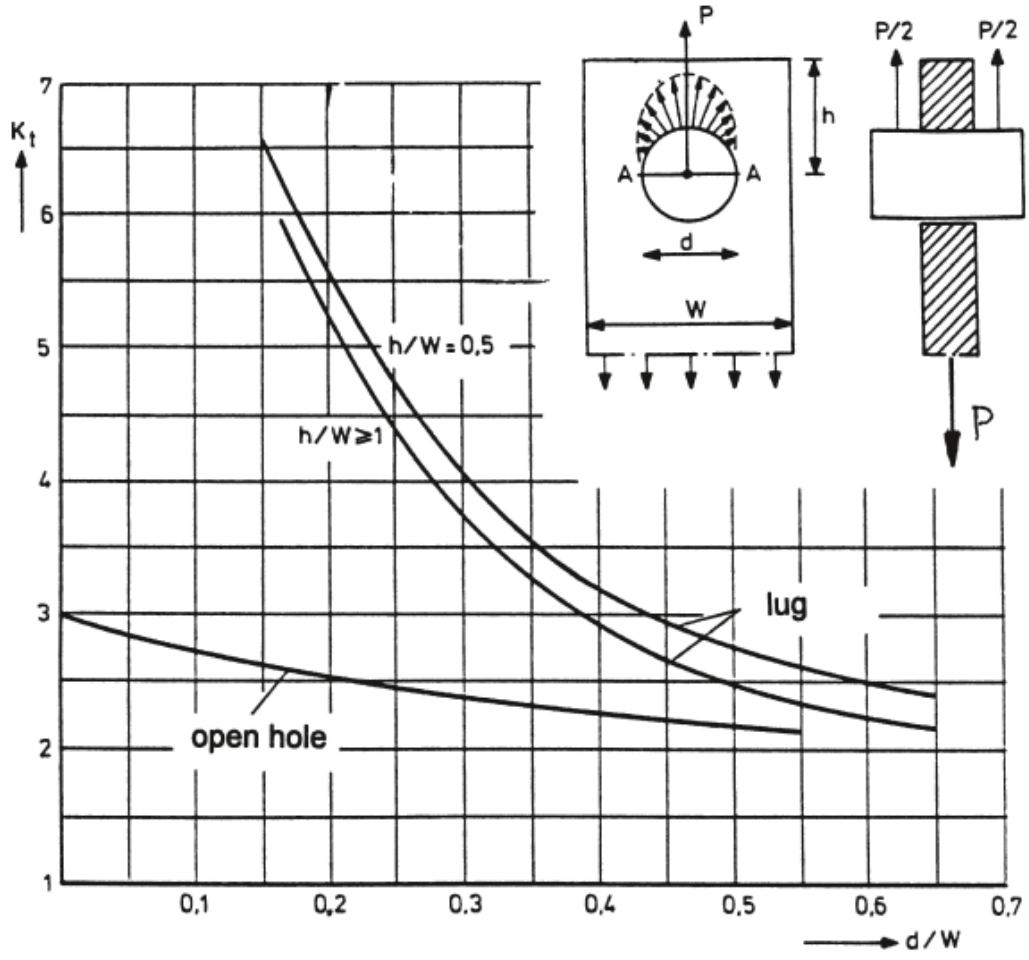

Figure A.2: SCF diagram for a lug connection

Appendix B

Alternative stress calculation

In this appendix, the model is discussed that was initially developed to calculate the stress in the circumferential weld that connects the casting with the radial element (refer to Fig. B.1. The stresses that are found with this model are around ten times higher than the yield strength of the steel. This is probably not correct, so it is concluded that this model is too conservative. More accurate results might be obtained by using plate or shell theory, but this is considered too complex for the scope of this thesis.

A schematic representation of the casting is shown in Fig. B.2. It is assumed that the reaction forces are only in the welds at the side of the casting (highlighted with red in Fig. B.1). From the force and moment equilibrium equations it is found that there is a reaction force and a reaction moment present in both welds. The magnitudes of the reactions are not easily obtained, because the adjacent plates at the sides of the casting do not have the same thickness (schematically shown in Fig. B.3). The stress in the welds depends on three factors, which all depend on the plate thickness:

- The SCF: depends on the difference in plate thickness between the casting and the plate
- The magnitude of the force or moment: depends on the stiffness ratios α and β
- The area (for axial stress) or the resistance moment (for bending stress)

It is checked which weld experiences the highest stress, to identify the most critical one. The stress is calculated with Eq. (B.1). However, axial force and bending moment are not distributed equally over the two sides of the element, because the plate thickness is not equal for both sides. The distribution of force and moment depends on the ratio of the (axial and bending) stiffness of the plates. These ratios are calculated first. The following assumptions are made:

- The casting behaves like a rigid element

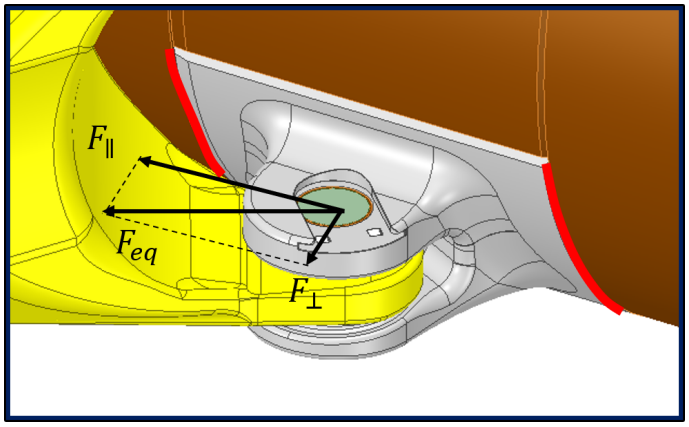

Figure B.1: Equivalent axial force on the lower casting decomposed in a parallel and perpendicular component

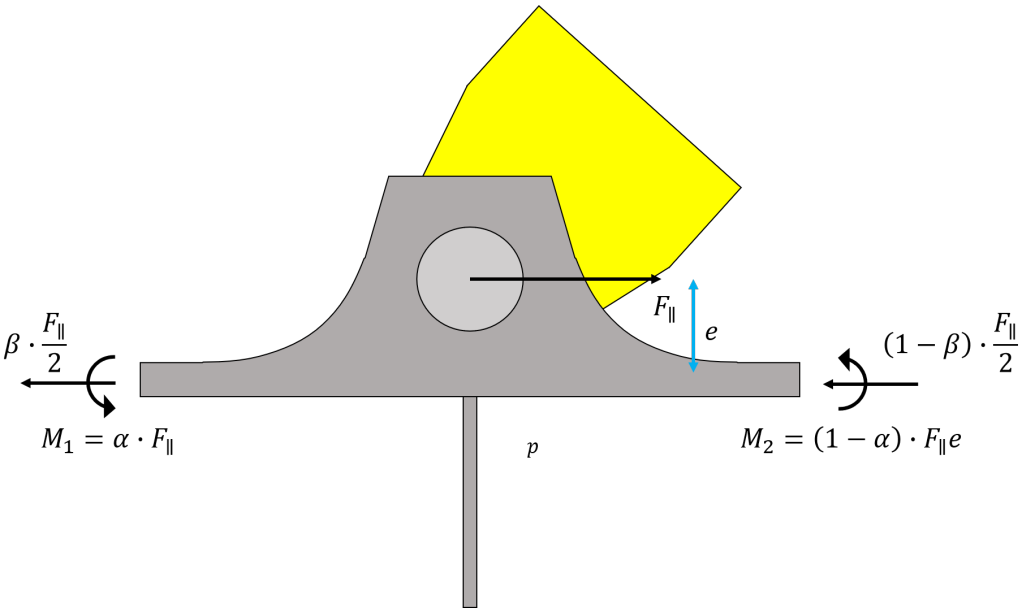

Figure B.2: Free body diagram of the casting

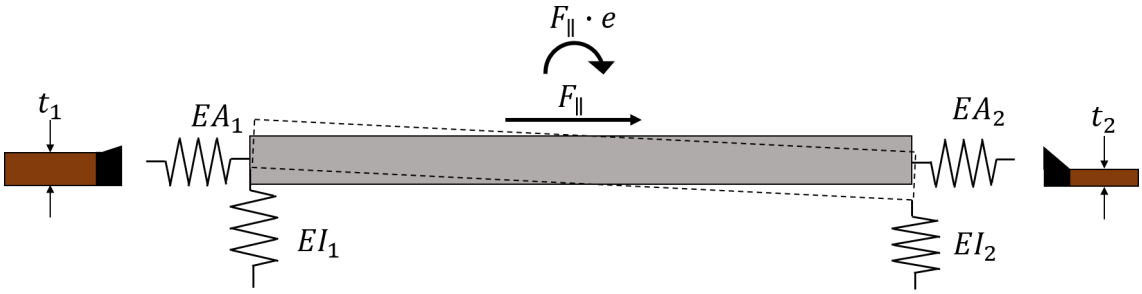

Figure B.3: Model used to calculate forces on the casting

- The reaction forces are in the welds on the sides only (indicated with red in Fig. B.1)
- The plates connected to the welds are modelled as clamped beams with equal lengths and a width that is equal to the length of the weld.

Please refer to Fig. B.2 and Fig. B.3 for the schematic representation of the situation. First the ratio for the bending stress is derived, and thereafter the ratio for the axial stress.

$$\sigma_{weld} = SCF_t \cdot (SCF_a \cdot \sigma_{axial} + SCF_b \cdot \sigma_{bend}) = SCF_t \cdot (SCF_a \cdot \frac{F_{ax}}{A_{weld}} + SCF_b \cdot \frac{M}{W_{weld}}) \quad \text{(B.1)}$$

The relative amount of moment depends on the bending stiffness only ($\frac{EI_1}{EI_2}$ in Fig. B.3). The ratio between M_1 and M_2 can be reduced to I_1 over I_2. The expression for I for a beam with a rectangular cross-section is shown in Eq. (B.3). The expression for the section modulus is shown in Eq. (B.4). Substituting these in Eq. (B.2), result in Eq. (B.5).

$$\frac{\sigma_{b1}}{\sigma_{b2}} = \frac{SCF_1 \cdot M_1/W_1}{SCF_2 \cdot M_2/W_2} \quad \text{(B.2)}$$

$$I_x = \frac{bt_x^3}{12} \quad \text{(B.3)} \qquad W_x = \frac{bh_x^2}{6} \quad \text{(B.4)}$$

$$\frac{\sigma_{b1}}{\sigma_{b2}} = \frac{SCF_1}{SCF_2} \cdot \frac{\frac{bt_1^3}{12} \cdot \frac{bt_2^2}{6}}{\frac{bt_2^3}{12} \cdot \frac{bt_1^2}{6}} = \frac{SCF_1 \cdot t_1}{SCF_2 \cdot t_2} \quad \text{(B.5)}$$

For the axial stress, the stress ratio is equal to the expression in Eq. (B.6) The axial force in the detail only depends on the stiffness EA_1 and EA_2 in Fig. B.3. Hence, the ratio between F_1 and F_2 can be reduced to $\frac{A_1}{A_2}$.

$$\frac{\sigma_{ax,1}}{\sigma_{ax,2}} = \frac{SCF_1 \cdot \frac{F_1}{A_1}}{SCF_2 \cdot \frac{F_2}{A_2}} \tag{B.6}$$

$$\frac{\sigma_{ax,1}}{\sigma_{ax,2}} = \frac{SCF_1 \cdot \frac{A_1}{A_1}}{SCF_2 \cdot \frac{A_2}{A_2}} = \frac{SCF_1}{SCF_2} \tag{B.7}$$

The SCFs that result from the change in plate thickness are calculated with Eq. (4.6). For the dimensions of the detail ($t_1 = 50[mm]$, $t_2 = 22[mm]$ and $t_{casting} = 60[mm]$), the SCFs are calculated. They result in $SCF_1 = 1.1$ and $SCF_2 = 1.9$. Substituting these values in the stress ratios, yields the expressions in Eq. (B.8) and Eq. (B.9). It can be concluded that the bending stress is most critical for the thicker plate, whereas the axial stress is most critical for the thinner plate. Consequently, the most critical weld can only be determined if the ratio between axial stress and bending stress is known, and both sides will have to be checked. After doing so, it is concluded that this method does not provide accurate stress results.

$$\frac{\sigma_{b,1}}{\sigma_{b,2}} = \frac{1.1}{1.9} \cdot \frac{5.0}{2.2} \approx 1.3 \tag{B.8}$$

$$\frac{\sigma_{ax,1}}{\sigma_{ax,2}} \approx 0.6 \tag{B.9}$$

Appendix C

Additional load case FE analysis

A fifth load case has been considered to prove the statement that the loads with a small standard deviation can be omitted for the analysis. For the fifth load case, the loads and magnitudes that are included in the analysis are shown in Table C.1. The difference between the load cases is shown in Table C.2 and is only + 2-3% which is sufficiently small to neglect the extra loads in LC5 compared to LC4.

Table C.1: All the load components on the radial member end

Load description	Standard deviation [kN]
Lateral – equivalent axial force (upper casting)	246
Lateral – equivalent axial force (lower casting)	200
Lateral – transversal force	25
Lateral – vertical force	43
Diagonal – equivalent axial force	93
Diagonal – transversal force	0
Diagonal – vertical force	13
Suspension line – axial force	191
Mooring line – axial force	4

Table C.2: Difference in hotspot stresses for LC4 and LC5

Load Case	Hotspot stress 1 [MPa]	Hotspot stress 2 [MPa]
LC4	9.77	3.60
LC5	9.45	3.67
Difference	**-3%**	**+2%**

Appendix D

All results

In this appendix, more results from the fatigue damage are shown. Refer to the captions for an explanation on the shown data.

Table D.1: Results for all identified locations for the 0°wave direction

Critical location	Description	Relative damage
1	Element-casting weld (lateral)	0.16
2	Minimum cross-section ear	0.01
3	Ear hole	0.14
4	Fork hole	0.04
5	Minimum cross-section fork	0.02
6	Pin element	0.01
7	Ring stiffener weld	0.02
8.1	Element casting weld 1 (radial) - HC	1.00
8.2	Element casting weld 1 (radial) - FEA	1.95
9	Element casting weld 2 (radial)	0.01

Table D.2: Results for all identified locations for the 30°wave direction

Critical location	Description	Relative damage
1	Element-casting weld (lateral)	0.36
2	Minimum cross-section ear	0.02
3	Ear hole	0.40
4	Fork hole	0.10
5	Minimum cross-section fork	0.04
6	Pin element	0.00
7	Ring stiffener weld	0.06
8.1	Element casting weld (radial) – hand	1.00
8.2	Element casting weld (radial) - FEA	-
9	Element casting weld 2 (radial)	-

Table D.3: Results for all identified locations for the 180°wave direction

Critical location	Description	Relative damage
1	Element-casting weld (lateral)	0.20
2	Minimum cross-section ear	0.01
3	Ear hole	0.18
4	Fork hole	0.05
5	Minimum cross-section fork	0.02
6	Pin element	0.01
7	Ring stiffener weld	0.03
8.1	Element casting weld (radial) – hand	1.00
8.2	Element casting weld (radial) - FEA	-
9	Element casting weld 2 (radial)	-

Hs [m]	Tp [s]								Sum	Cum
	4.0	7.0	9.0	11.0	13.0	15.0	17.0	19.0		
0.50									0.0	0.0
1.50		0.01	0.01	0.01					0.0	0.0
2.50		0.03	0.08	0.04	0.01				0.2	0.2
3.50		0.04	0.18	0.12	0.04				0.4	0.6
4.50		0.02	0.24	0.22	0.10	0.01			0.6	1.2
5.50		0.01	0.17	0.28	0.15	0.01			0.6	1.8
6.50			0.07	0.24	0.19	0.02			0.5	2.3
7.50			0.02	0.14	0.18	0.02			0.4	2.7
8.50				0.05	0.13	0.02			0.2	2.9
9.50				0.01	0.07	0.02			0.1	3.0
10.50					0.02	0.01			0.0	3.0
11.50									0.0	3.0
12.50									0.0	3.0
13.50									0.0	3.0
14.50									0.0	3.0
Sum	0.0	0.1	0.8	1.1	0.9	0.1	0.0	0.0	3.0	
Cum	0.0	0.1	0.9	2.0	2.9	3.0	3.0	3.0		

Figure D.1: Fatigue damage diagram for location 1 for the 0°wave direction only

Hs [m]	Tp [s]								Sum	Cum
	4.0	7.0	9.0	11.0	13.0	15.0	17.0	19.0		
0.50									0.0	0.0
1.50		0.01	0.01						0.0	0.0
2.50		0.03	0.08	0.04	0.01				0.2	0.2
3.50		0.04	0.17	0.10	0.04				0.4	0.6
4.50		0.03	0.22	0.20	0.08	0.01			0.5	1.1
5.50		0.01	0.16	0.25	0.13	0.01			0.6	1.7
6.50			0.06	0.22	0.17	0.01			0.5	2.1
7.50			0.01	0.12	0.16	0.02			0.3	2.4
8.50				0.05	0.12	0.02			0.2	2.6
9.50				0.01	0.06	0.02			0.1	2.7
10.50					0.02	0.01			0.0	2.7
11.50									0.0	2.7
12.50									0.0	2.7
13.50									0.0	2.7
14.50									0.0	2.7
Sum	0.0	0.1	0.7	1.0	0.8	0.1	0.0	0.0	2.7	
Cum	0.0	0.1	0.8	1.8	2.6	2.7	2.7	2.7		

Figure D.2: Fatigue damage diagram for location 3 for the 0°wave direction only

Hs [m]	Tp [s]								Sum	Cum
	4.0	7.0	9.0	11.0	13.0	15.0	17.0	19.0		
0.50									0.0	0.0
1.50			0.03	0.02	0.01				0.1	0.1
2.50		0.02	0.19	0.18	0.09	0.01			0.5	0.6
3.50		0.03	0.44	0.53	0.29	0.03			1.3	1.9
4.50		0.01	0.56	1.00	0.61	0.05	0.01		2.2	4.1
5.50			0.40	1.22	0.92	0.08	0.01		2.6	6.7
6.50			0.15	0.96	1.03	0.11	0.01		2.3	9.0
7.50			0.03	0.49	0.87	0.12	0.01		1.5	10.5
8.50				0.16	0.55	0.12	0.01		0.8	11.4
9.50				0.03	0.24	0.10	0.01		0.4	11.7
10.50					0.07	0.06	0.01		0.1	11.9
11.50									0.0	11.9
12.50									0.0	11.9
13.50									0.0	11.9
14.50									0.0	11.9
Sum	0.0	0.1	1.8	4.6	4.7	0.7	0.1	0.0	11.9	
Cum	0.0	0.1	1.9	6.5	11.1	11.8	11.9	11.9		

Figure D.3: Fatigue damage diagram for location 8 for the 0°wave direction only

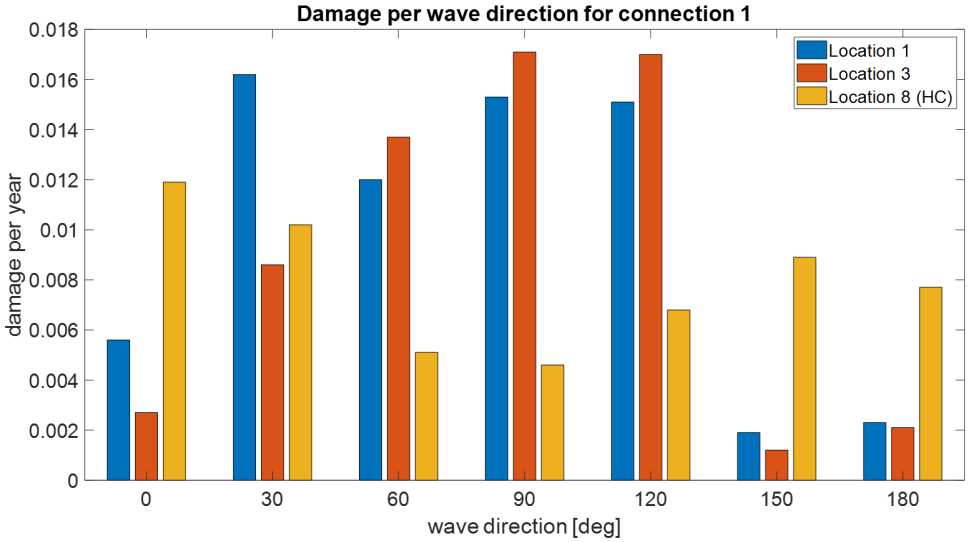

Figure D.4: Fatigue damage results per wave direction for connection 1

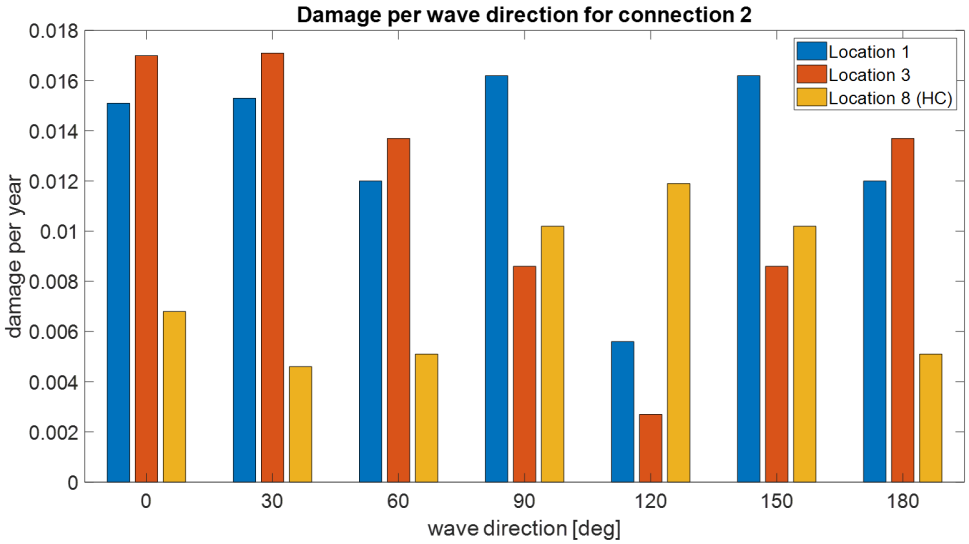

Figure D.5: Fatigue damage results per wave direction for connection 2

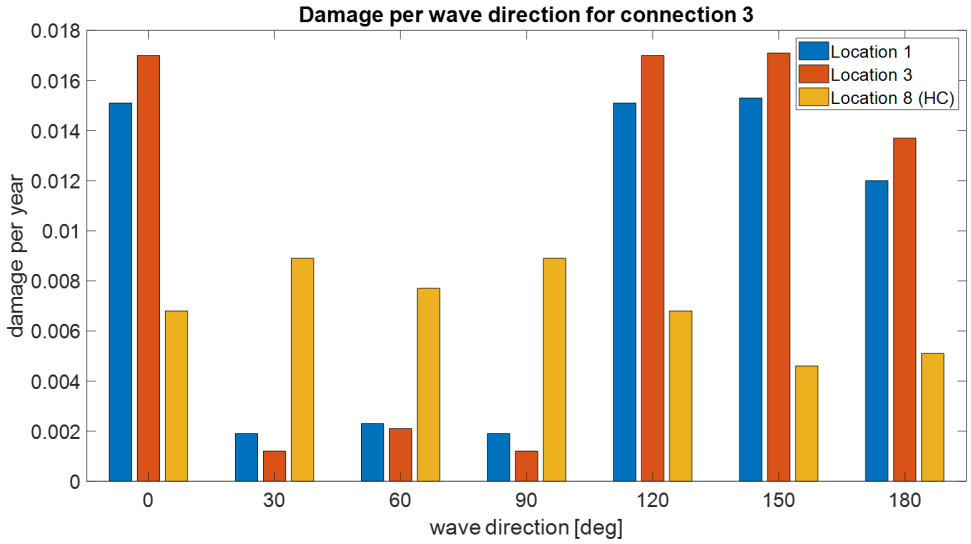

Figure D.6: Fatigue damage results per wave direction for connection 3

Table D.4: Results for all locations, wave directions and connections

	Connection 1			Connection 2			Connection 3		
Wave Dir.	1	3	8	1	3	8	1	3	8
0	0.003	0.0027	0.0119	0.0151	0.0170	0.0068	0.0151	0.017	0.0068
30	0.0162	0.0086	0.0102	0.0153	0.0171	0.0046	0.0019	0.0012	0.0089
60	0.0120	0.0137	0.0051	0.0120	0.0137	0.0051	0.0023	0.0021	0.0077
90	0.0153	0.0171	0.0046	0.0162	0.0086	0.0102	0.0019	0.0012	0.0089
120	0.0151	0.0170	0.0068	0.0030	0.0027	0.0119	0.0151	0.0170	0.0068
150	0.0019	0.0012	0.0089	0.0162	0.0086	0.0102	0.0153	0.0171	0.0046
180	0.0023	0.0021	0.0077	0.0120	0.0137	0.0051	0.0120	0.0137	0.0051